The Heart as an Organ at Risk in Radiation Therapy of Locally Advanced Non Small Cell Lung Cancer

Linnea Frang

Master Thesis in Medical Technology

Department of Physics and Technology
University of Bergen

June, 2023

Scientific environment

This project was a part of an ongoing prospective imaging study at Haukeland University Hospital (REK 2019/749 Utvikling av metoder for persontilpasset strålebehandling av lokalavansert ikke-småcellet lungekreft). All included patients have consented to participate in the study and the candidate has worked with de-identified data.

Haukeland University Hospital

Acknowledgements

First I would like to thank my supervisor, Liv Bolstad Hysing, for an interesting project and for the great support and help I have recieved over the past year. Your insight in the field have been invaluable and I am proud of what we have created together. Thank you for always being supportive and confident in this project.

I would also like to express my gratitude to my co-supervisors, Kristine Fjellanger and Inger Marie Sandvik. Kristine, thank you for consistently showing patience and providing invaluable assistance whenever I faced challenges, particularly in dealing with Raystation. The insights shared by Inger Marie regarding lung cancer and heart contouring were important in giving my project a strong foundation. Furthermore, I would like to extend my thanks to everyone at the Department of Oncology and Medical Physics, especially those at Haukelandsbakken 45, for a warm and welcoming atmosphere and for always being accessible to share their knowledge and support me along the way. I am grateful to Helge Egil Seime Pettersen for your assistance with Python and to Marcin Pawel Sikora for your guidance regarding Raystation.

Lastly I want to express my gratitude for the amazing support I have had over my five years at the university. My dedicated study partner throughout the degree, Julia Cat-Vy Nguyen, thank you for all the laughs and tears we have shared over the years. The wonderful friends I have made throughout my entire journey with Curie, including both the ones I began with in 2018 and those I have gained since. Thank you to my family and friends for always supporting me and cheering me on, I could not have done this without you.

Linnea Frang
Bergen, June 2023

Abstract

Purpose: Currently, in radiation treatment planning for locally advanced non-small cell lung cancer (LA-NSCLC), the heart is typically contoured as a whole organ at risk. Both photon and proton beam techniques are used for this purpose in research. The dose delivered to the heart has emerged as a significant consideration in predicting patients' survival outcomes. Therefore, the purpose of this thesis was to investigate the feasibility of delineating specific substructures within the heart, assess the robustness of treatment plans for these structures, and analyze the variation in dose distribution among them. This analysis involved comparing the dose received by substructures with that of the whole heart, as well as comparing the dose distributions between photon beam and proton beam planning.

Methods: Contouring was done on fifteen patients, nine with both rapid contrast computer tomography (CT) scans in planning state of treatment, and for all fifteen average intensity projection four-dimensional (AVE-4D) CT scans in both planning state of treatment and week 1. In-house and new Python scripts were used to quantify the geometric differences of the structures. Existing in-house intensity-modulated radiation therapy (IMRT) and intensity-modulated proton therapy (IMPT) plans were utilized, with prescribed doses of 60-66 Gy. The substructures and the dose metrics utilized for analysis were based on existing literature that links radiation dose to radiation-induced heart disease or survival outcomes.

Results: Nineteen substructures of the heart and the cardiovascular system were found from literature and contoured. The volume of the substructures was found to have significant change for ten of the structures in the planning state of treatment between the different CT scans, while only one of the structures had significant change between the AVE-4D-CT scans. The overlap of the structures were generally higher for large structures (> 10 cc), with some exceptions. Dmean, D45%, V15Gy and V30Gy were used as dose metrics for analysis. Five of the substructures, mostly situated at the base of the heart, was found to not be robust over time in IMRT planning, with signif-

icant change between planned dose and actual dose. Only one, the superior vena cava, was found to not be robust for IMPT planning. All of the substructures were found to get significantly less dose with IMPT than IMRT. Many of the substructures had significant different dose than to the heart with both IMRT and IMPT.

Conclusion: IMPT demonstrates the potential to significantly reduce the radiation dose to all substructures considered in this project, thereby potentially improving the overall survival of LA-NSCLC patients undergoing radiation treatment. The base of the heart is of particular interest, as certain parts were found to be less robust in IMRT planning and some parts received higher doses compared to the heart as a whole. Additionally, larger structures show promise for feasible and beneficial contouring using AVE-4D-CT. Further studies, including a larger patient cohort, focusing on the base of the heart, especially the left atrium, and the great vessels superior to the heart, would be valuable.

Contents

Abbreviations

3D-CRT	Three-Dimensional Conformal Radiation Therapy
AIP	Average Intensity Projection
AVE-4D-CT	Average Intensity Projection Four-Dimensional Computer Tomography
AV	Atrioventricular
AVN	Atrioventricular Node, AV Node
CAD	Coronary Artery Disease
CT	Computer Tomography
CTCAE	Common Terminology Criteria for Adverse Effects
CTV	Clinical Target Volume
Cx	Left Circumflex Coronary Artery
DVH	Dose-Volume Histogram
FDG	Fluorodeoxyglucose
HF	Heart Failure
HU	Hounsfield Unit
HUS	Haukeland University Hospital
IHD	Ischemic Heart Disease
IQR	Interquartile Range
IMPT	Intensity-Modulated Proton Therapy
IMRT	Intensity-Modulated Radiation Therapy
LAD	Left Anterior Descending Artery
LA-NSCLC	Locally Advanced Non-Small Cell Lung Cancer
LET	Linear Energy Transfer
LMCA	Left Main Coronary Artery
MACE	Major Adverse Cardiovascular Event

MCE	Major Coronary Event
MHD	Mean Heart Dose
NLCG	Norwegian Lung Cancer Group
NSCLC	Non-Small Cell Lung Cancer
OAR	Organ at Risk
OS	Overall Survival
PET	Positron Emission Tomography
PT	Proton Therapy
PTV	Planned Target Volume
QA	Quality Assurance
QUANTEC	The Quantitative Analysis of Normal Tissue Effects in the Clinic
RBBB	Right Bundle Branch Block
RBE	Relative Biological Effectiveness
RCA	Right Coronary Artery
RT	Radiation Therapy, Radiotherapy
RIHD	Radiation-Induced Heart Disease
RIVHD	Radiation-Induced Valvular Heart Disease
SABR	Stereotactic Ablative Radiotherapy
SAN	Sinoatrial Node, Sinus Node
SF	Survival Fraction
SFUD	Single Field Uniform Dose
SVC	Superior Vena Cava
VHD	Valvular Heart Disease
VMAT	Volumetric Modulated Arc Therapy

List of Figures

List of Tables

Chapter 1

Introduction

1.1 Motivation

In 2015 Bradley et al. published a study where they compared overall survival after standard radiotherapy with high-dose conformal radiotherapy, for patients with stage three non-small-cell lung cancer (NSCLC) [1]. These patients have poor prognosis, and the hypothesis was that an increased total dose would benefit the patients. The results however showed that the high dose radiotherapy was not better than the standard for this group, and "might potentially be harmful" [1]. Many researchers have tried to find the reason for this. One hypothesis that is being investigated is that the increased dose to the heart could be of importance. Therefore, the heart has gained attention as an important organ at risk (OAR) in radiotherapy (RT).

In clinics today, the mean dose to the heart is one of the calculated metrics used in treatment planning, with a recommended threshold. However, the heart receives varying dose in different structures of the heart and might be more affected by an increased dose in one substructure than another. Research have suggested to substantiate the correlation between radiation therapy and mortality of heart diseases, but there is still no clear academic agreement on the matter. Because various studies utilize distinct data, measurements, and objectives, comparing them directly becomes challenging.

In 2024 a new radiation therapy centre is opening in Bergen, where some patients can be treated with proton therapy (PT) if it is favourable over state-of-the-art photon therapy. With this opening, there is an increased amount of research in this field at Haukeland University Hospital (HUS). Research by Gjyshi et al, at the Department of Radiation Oncology, the University of Texas MD Andersen Cancer Center, found that in planning with modern PT the dose to the heart could be decreased [2]. This study

only analyse mean heart dose as a parameter, and do not take the varying radiation to the different parts of the heart into account. A study at the Department of Oncology and Medical Physics, Haukeland University Hospital, by Boer et al. also found that modern PT show potential to decrease the toxicity to the heart in treatment [3]. During the peer review leading up to the publication of the article a comment was made on the study. The comment suggested that further investigation could be conducted on the different structures of the heart, specifically focusing on how the dose vary in these structures.

1.2 Thesis Outline

This master project will retrospectively study the heart's substructures as organs at risk in simulated treatment of NSCLC, using prospectively collected image data. The same data that was used in the study by Boer et al. will be used in this project, collected for the pulmDIBH-study at HUS (REK 2019/749) [3]. This data includes computed tomography (CT) scans acquired prior to treatment, as well as in week 1 and 3 during the seven-week radiotherapy treatment. Additionally, the data include simulated photon and proton radiation therapy treatment plans for 15 patients. Proper statistical methods will be utilized to compare risk of adverse heart effects with PT and state-of-the art photon therapy.

To calculate the dose to the different substructures the candidate will manually contour the chosen substructures, with supervision of an oncologist. Images will be studied in Eclipse (Varian Medical Systems, Palo Alto, CA, USA), a system used for treatment planning with photons at HUS. For treatment planning with protons RayStation (RaySearch Laboratories, Stockholm, Sweden) will be used. With these tools the candidate can collect dose statistics, to compare both drawings on different types of images, the different stages of treatment, and photon versus proton plans. The candidate will have to use appropriate statistical methods in this part of the project.

1.3 Objectives

The objective of this thesis is to investigate whether there are substructures within the heart that can contribute to the treatment planning process of radiation therapy. These substructures should be capable of accurate contouring and exhibit robustness over

time. The thesis will explore the varying doses delivered by photon therapy and proton therapy to the involved structures, with proton therapy expected to result in lower doses. The degree of dose reduction is of interest, as it may impact the probability of developing radiation-induced heart disease. Furthermore, the thesis aims to identify specific structures or regions within the heart that receive higher-than-anticipated doses, making them more vulnerable to injury. The main objectives ste-by-step can be summarized as follows:

i) Identify substructures and dose parameters that can show correlation with radiation-induced side effect on the heart from existing literature.

ii) Analyze the influence of both contouring inconsistency and uncertainties due to anatomical changes over time for the structures.

iii) Examine the planned and delivered dose to substructures by using existing simulated treatment plans of both proton and photon therapy.

iv) Compare the doses administered to the structures in existing simulated photon and proton treatment plans.

v) Evaluate the viability of using the dose to the heart as a surrogate measure for the substructures or regions within the heart.

The main part of this thesis involves the utilization of the Eclipse software (Varian Medical Systems, Palo Alto, CA, USA) to contour structures. Subsequently, various tools will be utilized to compare the structure contouring on different scans. The thesis will also use statistical tools to analyze the doses received by the different structures.

Chapter 2

Theory

In this chapter, the primary theoretical framework of the project is presented. It includes an overview of the heart's structure, physiology, and its vulnerability as an OAR during RT, as well as a brief summary of lung cancer and its treatment. Additionally, a detailed description of the fundamental aspects of RT, involving both photons and protons, and their interactions with biological matter, is provided.

2.1 General Anatomy and Physiology of the Heart

The heart is the muscle that moves blood around in the body. It is located in the front of the chest, behind the breastbone, within and protected by the ribcage, and between the lungs [4]. Typically, the heart is around the size of a fist. The heart works as two pumps, one on the right side, and one on the left side. Both sides consists of an atrium, where the blood comes in from vessels, and a ventricle, that pumps the blood out of the heart. Together they make the four chambers of the heart, called the right atrium, the right ventricle, the left atrium, and the left ventricle [4]. On the outside of the heart the pericardium lies as a sack that surrounds the heart muscle. It is there to keep the heart in place and protect it [4]. The pericardium typically holds a maximum of 50 ml of fluid, which serves the purposes of lubricating the heart's surface and acting as a protective shield against infections [5].

The blood from all around the body enters the heart in the right atrium. It arrives there through the vena cava, superior and inferior, respectively the upper and lower part of the vein. This blood is poor in oxygen. From the right atrium it moves to the right ventricle, and to the lungs through the pulmonary artery. In the lungs oxygen is added to the blood. The now oxygenated blood goes through the pulmonary veins to

the left atrium, to the left ventricle and out to the aorta. These blood vessels, namely the superior and inferior vena cava, the pulmonary artery, and the pulmonary veins, are collectively known as the great vessels of the heart[6]. These structures can be seen in Figure 2.1. The base of the heart is the upper region of the heart where the great vessels enter and exit the heart to the atria.The left ventricle's tip is where the lowest portion of the heart, known as the apex, is located [4].

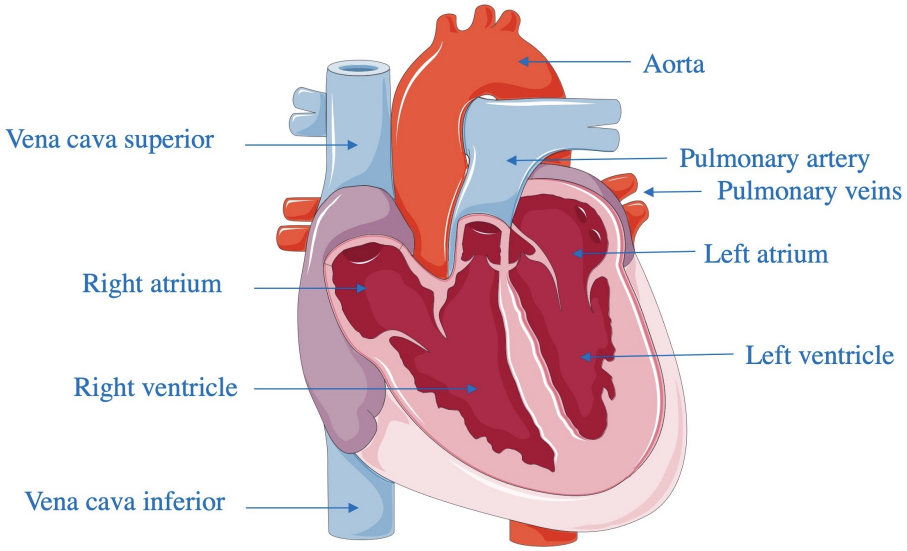

Figure 2.1: General heart anatomy, with names of chambers and vessels. Credit[1].

Each chamber of the heart has a valve to regulate the flow direction of blood between the chambers and vessels [4]. The valves have flaps that open to let blood flow to the next location and close to stop it from returning. There are two different types of valves. The first type of valves are between the atria and ventricles, and are called the atrioventricular (AV) valves. On the right side the tricuspid valve is placed between the right atrium and the right ventricle. The AV valve on the left side is called bicuspid or mitral valve, placed between the left atrium and the left ventricle. The second type are the semilunar valves, used to move blood out of the ventricles. On the right side the blood flows out from the right ventricle to the pulmonary artery through the pulmonic valve. Blood travels from the left ventricle to the aorta via the aortic valve [4]. The four valves can be seen in Figure 2.2

[1]Figure modified with text after adaptation of "Heart - Physiology" from Servier Medical Art by Servier, licensed under a Creative Commons Attribution 3.0 Unported License (accessed on 3 January 2022).

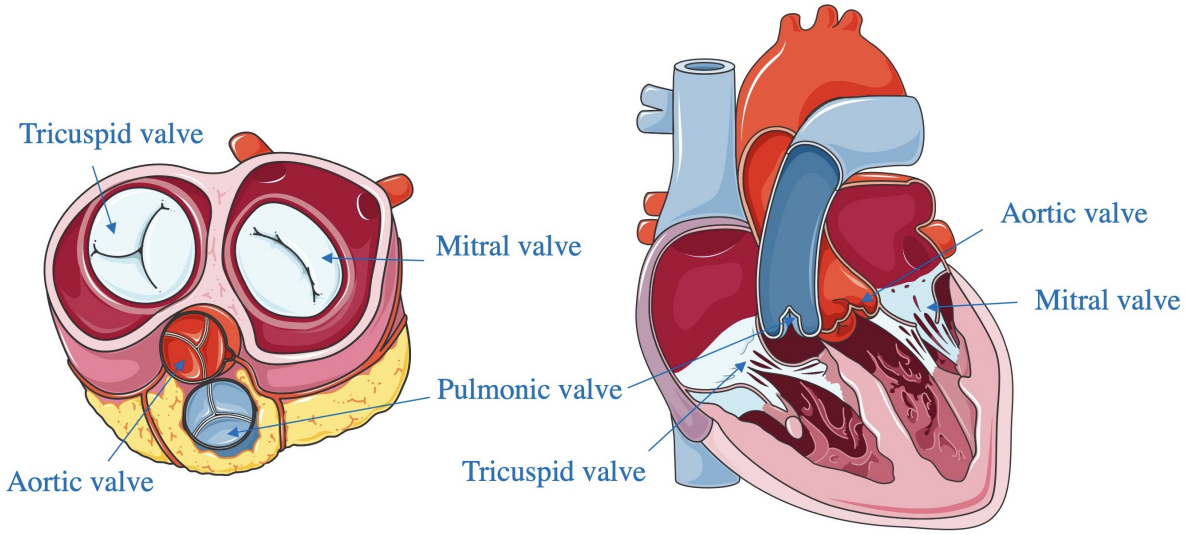

Figure 2.2: Illustration of the valves of the heart. Credit [2].

Systole and diastole are the two phases that together make up a heart cycle. Systole is the period of contraction, where the ventricles contracts to pump out blood. When the volumes of the ventricles are reduced the pressure increase, and the aortic and pulmonic valve are pushed to be opened, so the blood is pumped out to the arteries. There will always be some blood left in the ventricles. The diastole is the period of relaxation. The ventricles relax, and the volumes increase. The ventricles are filled with blood, from the veins, through the atria and now open AV valves. The atria lastly contracts, forcing blood into the ventricles. The cycle then begins again with a new systole.

There are coronary arteries on the outside of the heart muscle that supply blood to the heart. Situated at the division between the atria and ventricles, these vessels are separated into two branches, one on the right side and the other on the left side. The one on the right side is the right coronary artery, which lies on the outside between the right atrium and the right ventricle. The left main coronary artery divides into two, the left circumflex coronary artery and the left anterior descending coronary artery. The left circumflex coronary artery lies in the separation of the left atrium and the left ventricle, while the left anterior descending coronary artery lies between the ventricles. All can be seen in Figure 2.3.

[2]Figure modified with text after adaptation of "Heart - Physiology" from Servier Medical Art by Servier, licensed under a Creative Commons Attribution 3.0 Unported License (accessed on 3 January 2022).

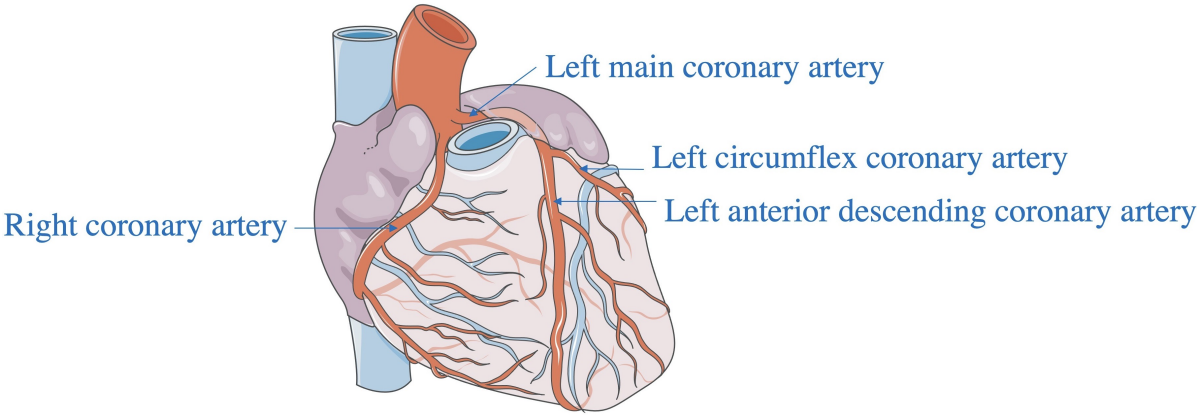

Figure 2.3: Illustration of the largest coronary arteries of the heart. Credit [3].

The heart's own electrical conduction system controls the pace of the heartbeat, the rhythm of the contractions. The signal begins in the sinus node (SAN), at the top of the right atrium, then is delayed in the atrioventricular node (AVN), between the atria and ventricles, at the bottom of the right atrium. From the AV node the bundle of His carries the signal to the Purkinje fibers. The Purkinje fibers make the ventricles contract. To transmit an electrical signal to the associated ventricle through the Purkinje fibers, the bundle of His has two branches on the left and right. This network can be seen in Figure 2.4.

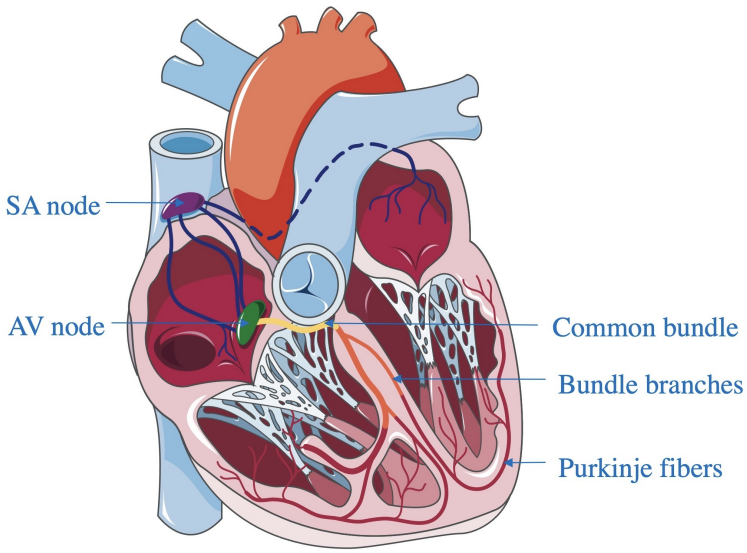

Figure 2.4: Illustration of the electrical conduction system of the heart. Credit [4].

[3]Figure modified with text after adaptation of "Heart - Physiology" from Servier Medical Art by Servier, licensed under a Creative Commons Attribution 3.0 Unported License (accessed on 3 January 2022).

[4]Figure modified with text after adaptation of "Heart - Physiology" from Servier Medical Art by Servier, licensed under a Creative Commons Attribution 3.0 Unported License (accessed on 3 January 2022).

2.2 Lung cancer

The second most common cancer worldwide is lung cancer. In 2020 12.2% of new cases of all cancers were diagnosed as lung cancer [7]. In 2021 there was registered 3499 new incidents of lung cancer in Norway [8]. As Norway have more senior citizens and is expected to have more senior citizens in the future, the incidents increase. As the median age for lung cancer diagnosis is 72 years, the disease primarily affects the elderly [9].

Patients with lung cancer typically have a bad prognosis, as lung cancer is the cancer type that claims the most lives [8]. The survival rate is measured in percentage of patients that lives five years after diagnosis, and is different for genders. For women the survival is 32.8%, while it is 25.7% for men [10]. The stage of the cancer at the time of discovery affects the survival rate. If the cancer is found early, before spreading, 73.3% of the women and 64% of the men lives after five years [10]. If the cancer has developed, and spread to other organs, 7% of the women lives, and 5.2% of the men lives after five years [10]. The last 20 years the survival rate in Norway has been nearly doubled. This has been made possible by better diagnostic tools, treatments, and follow-up, all of which are projected to continue to get better.

According to Kreftforeningen, there are several different examinations that can be used to detect lung cancer, some of which are described below [10]. In a clinical examination a doctor inspects the patients of signs of lung cancer. A common first test is an X-ray of the lungs, and if there is suspicion of lung cancer the patient will be sent to get a CT scan, that will show the tumor, and possible metastasis. Another examination is positron emission tomography (PET) CT, that will show the spread of the disease, and better show involved lymph nodes. For some patients, an MRI examination could be helpful to provide extra information that the CT scan cannot provide, since it has much better soft tissue contrast. Particularly in relation to the examination of the head, spinal cord, and spinal column, MRI can be a valuable diagnostic tool. Another test is bronchoscopy, which uses a tube to examine the airways and get a tumor biopsy. With the biopsy the tissue can be examined, and a precise diagnosis can be decided on, to determine the course of treatment [10].

The treatment course depends on a number of variables, including the extent or localization of the cancer, risks to healthy tissue, potential side effects for the patient, and the kind of cancer tissue. Small cell lung cancer and non-small cell lung cancer

(NSCLC) are two distinct types of lung cancer tissue. The most frequent is NSCLC [10]. The disease is classified in stages, with increasing severity, from stadium I to stadium IV. The staging is based on the size of the tumor, and the degree of spread to lymph nodes or other organs, and whether the cancer is spreading or not.

Chemotherapy, surgery, and radiotherapy are the three primary cancer treatments utilized today. These can be used alone, or together in different combinations. If the tumor is localised and accessible surgery is an option. The tumor-containing lobe is usually fully removed during surgery [10]. For patients with NSCLC about 25% have the tumor removed surgically [10]. If the cancer has spread throughout the body chemotherapy is often used. This medical procedure uses medications to kill cancer cells. The last main treatment type is RT, where ionizing radiation is used to reduce the size of the tumor. RT is effective when the tumor is isolated inside a defined area, but it is limited by the worry of causing damage to the healthy tissues.

In initial diagnosis lung cancer is clinically staged. CT of thorax and upper abdomen is taken of all patients with suspicion of lung cancer that are current to treat, and later PET-CT [11]. The staging uses the TNM (tumor, node, metastases) classification [5]. It includes the extent of both the primary tumor and regional lymph node, and whether there is metastasis or not. Generally, staging increase in severity. For stage III NSCLC the staging system can be seen in Table 2.1. Abbreviations are explained in Table A.1 in Appendix A.

Table 2.1: Stage III NSCLC TNM classification. Extracted from [11]. T:tumor, N:node, M:metastase.

Stage	T	N	M
IIIA	T1a-T2b	N2	M0
	T3	N1	M0
	T4	N0/N1	M0
IIIB	T1a-T2b	N3	M0
	T3/T4	N2	M0
IIIC	T3/T4	N3	M0

Observe that all of the different combinations are locally advanced as none include metastasis. It can also be seen how the stage III group may have a wide range of tumor and node statuses and how they will be treated accordingly. During the time of diagnosis, approximately 40% of all cases of NSCLC are classified as stage III, which is referred to as locally advanced (LA) NSCLC. Curative RT is commonly recommended as an appropriate treatment approach for LA-NSCLC [11].

2.3 Physics of Radiotherapy

RT incorporates principles from radiation physics, such as nuclear physics and the characteristics of ionizing radiation, which are crucial for comprehending the effects of radiation on biology and the processes followed in clinical settings.

2.3.1 Interactions of Photons with Matter

In RT, light uncharged particles such as photons undergo three major interactions with matter: photoelectric effect, Compton scattering, and pair production. 1) The photoelectric effect occurs when a photon collides with a bound electron in an atom, and the entire energy of the photon is transferred to the electron, causing it to become a positive ion. The photon ceases to exist after this interaction [12]. 2) In Compton scattering the photon partially gives away it's energy to a "free" electron, with small binding energy, and the rest to a photon with a new direction, that can take part in further interactions [12]. 3) When a photon collides with an atomic nucleus and its energy exceeds 1.022 MeV, pair production may occur, resulting in the creation of an electron-positron pair that travel in different directions [12]. The type of interaction that takes place is determined by the level of energy. For RT high energy photons are used, and at these energies the Compton scattering process dominates [12].

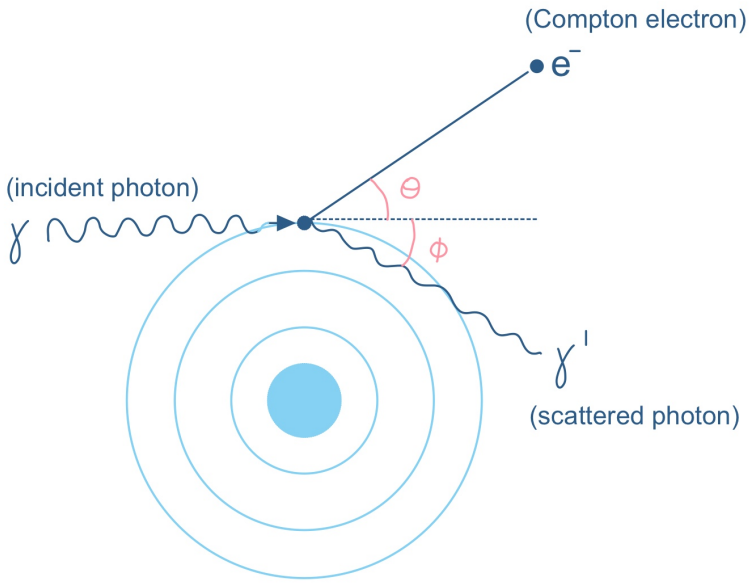

Figure 2.5: Illustration of Compton scattering. γ is the incident photon, colliding with a "free" electron. This becomes the Compton electron, that moves in a new direction, with angle θ. A scattered photon, γ', moves with an angle ϕ.

2.3.2 Interactions of Protons with Matter

In contrast to photons, protons are charged particles that possess mass. Between a charged particle and an atom, there exists a strong electromagnetic force, known as the Coulomb force. This force can easily cause the charged particle to stop, deflect, or lose its kinetic energy as it interacts with the atomic electrons and/or nucleus. Therefore, a proton can undergo various reactions when interacting with matter, some more important to RT. 1) The proton loses energy and decelerates when it undergoes inelastic collision with atomic electrons. This is the primary factor contributing to the absorbed dose in PT. The energy loss over distance is showed with the Bethe-Bloch formula, dependent on a number of factors, including the material, the charge and the speed of the particle [13]. 2) When a proton experiences elastic collisions with atomic electrons or nuclei, it changes direction, resulting in beam broadening. Therefore, the beam is positioned close to the patient to maintain accuracy [12]. 3) Inelastic scattering with nuclei or nuclear reactions can occur if the protons have sufficient energy to overcome the Coulomb barrier. This can generate secondary particles, which may contribute to the treatment dose beyond what was planned [12].

2.3.3 General Concepts in RT

The unit for absorbed radiation dose is gray (Gy), and defined as 1 J/kg, energy per mass [14]. This can be seen in Formula 2.1. When the beams particles interact with matter, like biological tissue of a patient, the beam attenuates. The intensity I of a beam after a distance x is determined by the initial intensity, I_0, and the attenuation coefficient, μ. This can be seen in Formula 2.2.

$$D = \frac{dE}{dm} \tag{2.1}$$

$$I = I_0 e^{-\mu x} \tag{2.2}$$

Linear energy transfer (LET) relates to how much energy is deposited along the particle track, and is a measure of the ionizing radiation's quality [12]. It reflects the biological effect of radiation, as the energy transferred per unit length of the path [15]. This can be seen in the definition in Formula 2.3, with dE, the energy deposited on the distance, dx. The unit is [keV/μm], kiloelectron volt per micrometer. LET is not measurable, but can use the experimental equivalent lineal energy (l).

$$L = \frac{dE}{dx} \tag{2.3}$$

Relative biological effectiveness (RBE) is a description of biological effectiveness [15], seen in Formula 2.4. Equivalent dosages of various radiation types will not have the same biological damaging effects, and their RBE values reflect this. With the same dose, a greater RBE value causes more injury. RBE is closely related to LET, as a higher RBE value tells that the substance is more efficient in cell killing [15].

$$RBE = \frac{Dose\ of\ reference\ radiation}{Dose\ of\ test\ radiation} \tag{2.4}$$

2.3.4 External RT

Energy Loss of Photons and Protons

The goal of RT in treatment is to give the tumor as much radiation as possible while irradiating the surrounding healthy tissue as little as possible. There are two different types of RT, internal radiation, including nuclear medicine and brachytherapy, and external beam RT [12]. External RT can be used both for imaging of the patients, and delivery of radiation to treat the cancer. Radiation is directed at the cancer in the body by a machine while treating cancer with external RT. These beams pass through the body of the patient in the planned location. High energy x-rays, photon beams, are commonly utilized. After the dosage maximum, the absorbed dose for photons declines with distance, as seen in Figure 2.6. As the beam of photons traverses through matter, its energy remains unaltered but its intensity is attenuated [12].

Proton beams can also be used for external RT. Protons experience a different type of energy loss over distance, as can also be seen in Figure 2.6. Most of the energy in the proton beam is lost shortly before the particles stop, depositing a significant amount of energy in what is known as a Bragg peak [12]. The depth the Bragg peak occurs at is defined by the initial energy of the protons. This makes it possible to spare more healthy tissue, but also sets higher demands on the accuracy of the beam. With a spread out Bragg peak (SOBP), also illustrated in Figure 2.6, can be designed to include the whole tumor. This is made by adding together multiple beams of lower intensity and shorter range [15].

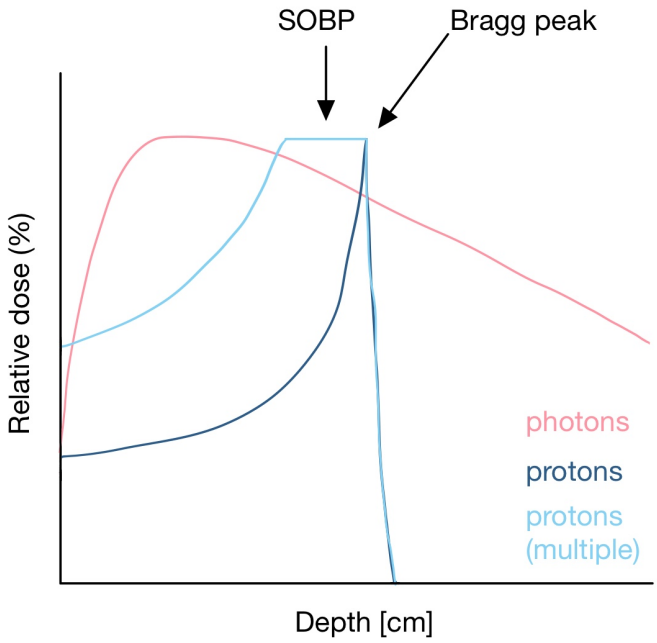

Figure 2.6: General depth dose curve for photon and proton. Dose expressed in % and distance expressed in cm. SOBP: Spread out Bragg peak. Credit[5].

Direct and Indirect Ionizing Radiation

There are two types of ionizing radiation: direct and indirect [15]. Charged particles, like protons, are directly ionizing. When absorbed, they contain enough energy to cause both chemical and biological alterations [15]. X-rays and γ-rays are indirectly ionizing. Instead of directly harming the target, indirect ionizing radiation is absorbed and provides energy to create charged particles that can cause damage. The energy of the photons and the chemical composition of the absorbing substance both affect how the x-rays are absorbed. The amount of energy loss varies, and so does the amount of fast electrons produced. The fast electrons can ionize other atoms and eventually lead to biological damage [15].

Direct and Indirect Action of Radiation

When radiation is absorbed in a biological material there can be effects caused by both direct and indirect action [15]. High LET radiation typically causes direct action of radiation, whereas low LET radiation typically causes indirect action of radiation. Through direct action, the radiation directly affects the cell's critical target, initiating the chain of events that lead to biological damage [15]. Indirect action is responsible

[5]Illustration made by the candidate, inspired by [16].

for almost two thirds of the biological damage induced by x-rays.

Free radicals are essential in indirect action. A free radical is an atom or molecule that has one unpaired orbital electron in the outer shell [15]. Because of the unpaired orbital electron the atom or molecule is highly chemical reactive. About 80% of the cell is composed of water, and as a result of radiation, the water of the cells can become ionized [15]. This can be expressed as Formula 2.5

$$H_2O \rightarrow H_2O^+ + e^- \tag{2.5}$$

The resulting ion radical, H_2O^+, is an atom that has lost an electron and is now electrically charged. H_2O^+ is a free radical by definition, and is therefore called both an ion and a free radical, an ion radical [15]. This decays shortly to a free radical, still with an unpaired electron. In reaction with water OH· is produced, hydroxyl radical, expressed with Formula 2.6.

$$H_2O^+ + H_2O- > H_3O^+ + OH\cdot \tag{2.6}$$

This hydroxil radical also have an unpaired electron, and is therefore highly reactive, and can damage the target, such as DNA [15]. The chain of events is summarized in Figure 2.7.

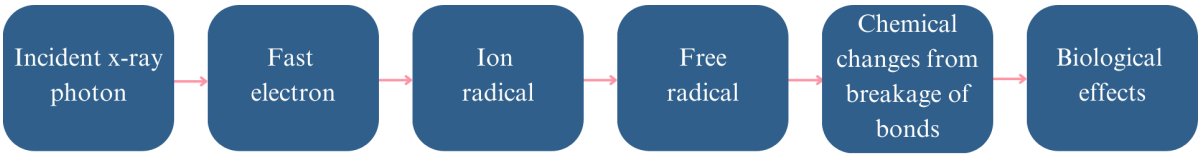

Figure 2.7: Chain of events for indirect action of radiation.

2.4 Biology of Radiotherapy

2.4.1 Survival of Cells

The DNA in the cells is the primary target of ionizing radiation, to stop reproduction of the cells [15]. DNA is made up of four different bases connected in two specific pairs. Two strands are connected with a hydrogen bond. This chemical bonds in the DNA can be broken when radiation strikes it. There are two types of breaks, single strand breaks, and double strand breaks. In a single strand break the other strand can repair the damage, as it knows what pairing strand is missing. With a double strand break repair is more difficult, and the radiation if more efficient in damaging the DNA. Breaking of chemical bonds in the cell can lead to mutation of the cell or cell death. Mutation can

lead to hereditary effects or cancer. The DNA must be exposed to enough energy for sufficient double strand breaks to occur in order to kill a cell [15]. The biological effect of 1 Gy is: 1000 single strand breaks, 20-40 double strand breaks, and typically 30% of the cells killed [15].

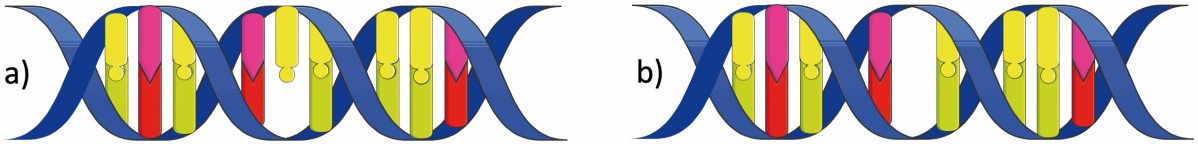

Figure 2.8: Illustration of the difference between a) single strand break, and b) double strand break of the DNA. Credit[6].

Cell Cycle

New cells are made by cell division (mitosis), where the cell duplicates itself, in a number of steps, called a cell cycle [15]. First, the cell duplicates the contents in the cell, before it splits into two distinct cells. The cell cycle can be split in four phases: G1, S, G2 and M, shown in Figure 2.9. The time it takes for a cell to complete all the four phases is known as mitotic-cycle or as cell-cycle time T_c. Cancer cells have a shorter cell-cycle time than normal cells [15]. On the other hand, normal cells can proliferate faster after radiation [15]. The cells are the most sensitive to radiation in the M and G2 phase of the cell cycle, and the most resistant in the S phase. After irradiation, there will be an increase in the percentage of surviving cells in the radioresistant stages. Damaged cells may be controlled and made to die. Radiation is substantially less effective at killing non-proliferating cells than at killing proliferating cells.

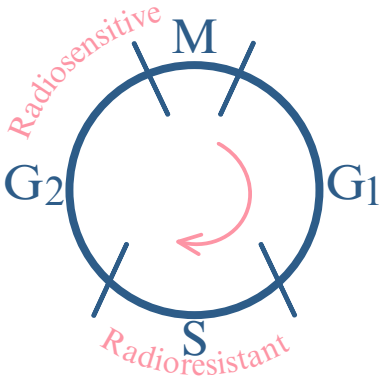

Figure 2.9: Illustration of the cell cycle phases. It illustrates which phases the cell is most senstive and resistant to radiation.

[6]Figure modified after adaptation of "Nucleic_acids" from Servier Medical Art by Servier, licensed under a Creative Commons Attribution 3.0 Unported License (accessed on 25 February 2022).

Cell Death

Radiation can cause different types of cell death in the body. Damage to DNA caused by radiation can result in various outcomes, and these are typically categorized into distinct groups [17]. Mitotic catastrophe refers to cell death that occurs when cells attempt to divide but fail in mitosis. Necrosis is an uncontrolled form of cell death that triggers an inflammatory response. In contrast, apoptosis is a programmed and controlled form of cell death that does not provoke inflammation. Senescence refers to a state in which cells are still present but they are unable to complete the process of mitosis. Different cells in the body can undergo any of these types of cell death after exposure to radiation [17].

Distinguishing between proliferating and non-proliferating cells and their responses to radiation is crucial. Proliferating cells generate new cells to replace those that have died [17]. For non-proliferating cells, cell death is defined by the loss of a particular function, while in proliferating cells, it is defined by the inability to reproduce. RT targets the loss of reproductive ability, making it more relevant to normal tissues containing cells that divide and reproduce, such as fibroblasts, and less relevant to normal tissues that do not divide, like muscles [17].

The 5 Rs of RT

The biological effectiveness of radiation is impacted by all 5 Rs of radiobiology, and by understanding them, the reaction can be predicted [15]. The 5Rs are repair, repopulation, re-distribution, re-oxygenation, and radio-sensitivity [18]. Repair is the process by which the cell heals the DNA. The total radiation dose is divided into fractions, to spread out the treatment time. Re-population takes into account the fact that new cells form between each fraction and that cancer cells divide more quickly than healthy cells. The tissue becomes more resistant to the following fraction as a result of this and repair. Utilizing the fact that radiation therapy primarily impacts cells during the M and G2 phases, re-distribution synchronizes the radiation with these phases to optimize treatment effectiveness. Re-oxygenation makes use of the fact that RT most strongly affects cells with high oxygen levels, as it makes the damage from free radicals permanent. The tissue is made more sensitive to the next fraction by both re-oxygenation and re-distribution. The last R is radio-sensitivity. Different cells respond differently to radiation, and it is important to know how sensitive the specific cells are to radiation [15].

Dose Response

The linear quadratic (LQ) model is a model to explain the survival rate of the cells [15]. It is based on stochastic concepts on how energy is deposited. The formula for survival fraction (SF) can be seen as Formula 2.7, with D as the total dose in Gy. The SF of cells after a single dose can described with two constants: α and β. α represents non-repairable injuries, double strand breaks, while β represents repairable injuries, single strand breaks. The α/β-ratio shows the characteristic relationship for different types of tissue, when the components contribute equally, and is higher for early responding tissue than late responding tissue. The SF can also incorporate the impact of the oxygen effect, which refers to the influence of oxygen on the biological response of molecules to radiation.

$$SF = e^{-(\alpha D + \beta D^2)} \tag{2.7}$$

The LET affects the cells' survival curve; when the LET is high, the survival curve exponentially declines, whereas when the LET is low, the survival curve initially slopes and then exponentially declines with higher doses [15]. Both LETs are illustrated in Figure 2.10.

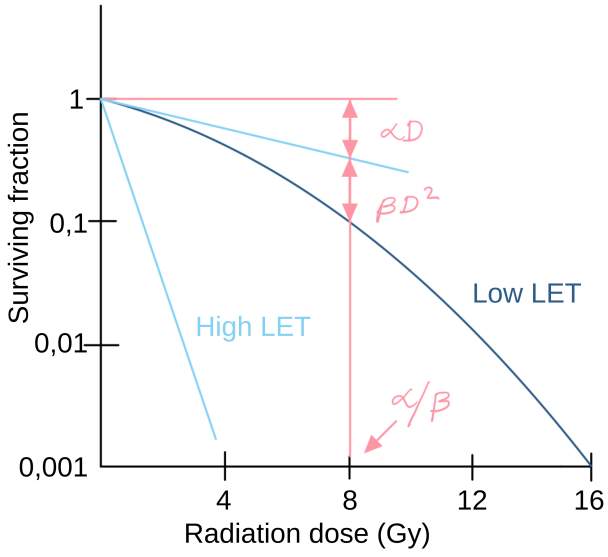

Figure 2.10: Cell survival curves under different conditions. One can both see the curves of when the linear energy transfer (LET) is low, and when the LET is high. α and β represents double strand breaks and single strand breaks, respectively.

Different tissue responds differently to radiation. Early responding tissue, such as skin responds in two to three weeks, as they have a high α/β-ratio. Late responding

tissue, such as the lungs, manifests in months to years after radiation, with a low α/β-ratio. The dose response curve in tissue is a plot of biological effect observed against the dosage given [15]. Generally, a higher dosage will increase the effect. The dosing range between achieving tumor control probability and the normal tissue complications probability is known as the therapeutic window, that can be seen i Figure 2.11. Differentiate between stochastic and deterministic effects from radiation. When there are stochastic effects, the likelihood of injury increases with dose, but the severity of the damage is independent of dose. The probability and severity of damage increase with dose for deterministic effects. Also, there are differences in the thresholds between the types: deterministic effects have a threshold for damages and take radiation illness and OARs into account, whereas stochastic effects have no threshold dose [15].

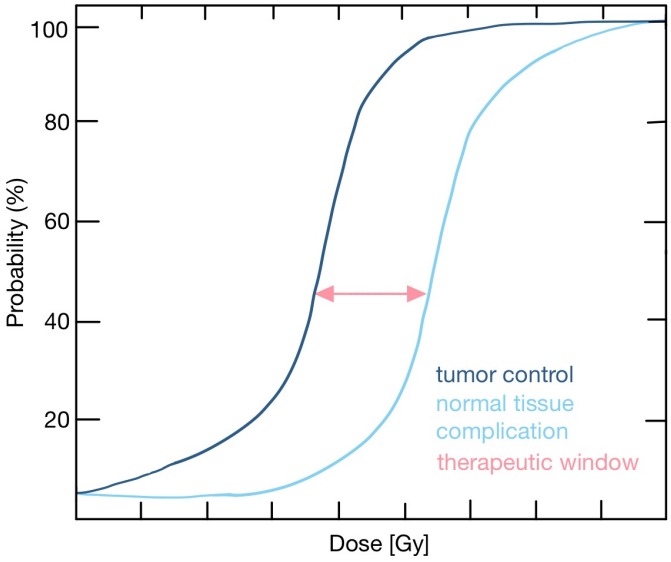

Figure 2.11: Dose response curve with the therapeutic window. The therapeutic window can be seen to lie between the dose response curve for tumor control and normal tissue complications. Credit[7].

2.4.2 Normal Tissue Response

The impact of radiation is dependent on various factors such as the type of radiation, dose, duration, and individual differences. The effects may occur at different times and can result in various normal tissue complications. Inflammation, which causes increased blood flow and heightened immune system activity, can lead to elevated activity in cells [17]. Fibrosis, characterized by the excessive production of fibrous tissue, is a frequent late toxicity following radiation exposure that can cause organ function loss [17]. Late radiation responses may manifest months or even years after exposure, while

[7]Illustration made by the candidate, inspired by [19].

early effects usually occur within 60 days of irradiation. Additionally, radiation exposure can cause different types of cell death [17]. Apoptosis typically begins within 6-24 hours after exposure, while mitotic catastrophe takes place within one to two cell cycles, ranging between 15 hours to two weeks. If necrosis transpires, it may be observed a few weeks after exposure, but this timeline may be accelerated with high doses. Acute effects of radiation include DNA damage, which the cells attempt to detect. If the damage goes undetected, it can lead to mutations. The cell may try to repair the damage if it is detected, and decide whether to proliferate further or stop growing and undergo apoptosis if the damage is too severe. Another late response can be impaired wound healing [17].

2.5 Workflow of Radiotherapy

High-quality imaging plays a critical role in the RT process and is essential for the efficient workflow of RT, as can be seen in Figure 2.12. The subsequent stages of contouring, planning, evaluation, and delivery all depend on the quality of the initial images. For RT, CT scans are usually required for treatment planning and must be obtained after the diagnosis specifically for planning. This is done in order to provide all information needed for treatment planning. This information includes the position of the patient, as they are in the same position when the treatment is delivered, tissue density information for the dose distribution, and the precise anatomical image.

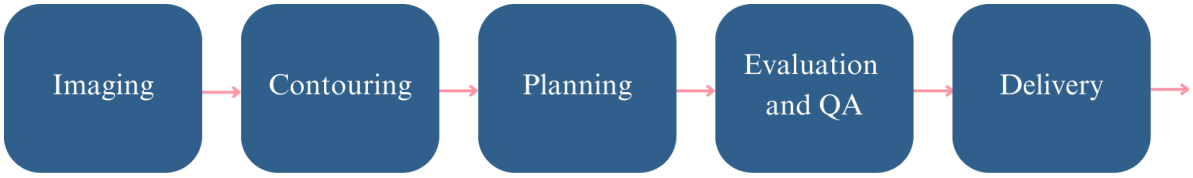

Figure 2.12: Illustration of the workflow stages in RT.

2.5.1 Imaging

CT is a an external radiation penetrating image modality. It is cost effective, quick, and usually available at most hospitals. With CT the anatomy of the patients body can be seen in three dimensions. CT is used for treatment planning for multiple reasons. The images are taken in the same position as the RT treatment will be in. Bones and soft tissue are highly contrasted on a CT scan [20]. CT also have a high geometrical accuracy, and matches the real anatomy of the patients, with high spatial resolution. Numerous

X-ray scans rotating along a patient are used in CT, the radiation is absorbed in the patient, and the intensity is detected on the opposite side of the patient. Each scan can be seen as a thin slice, and these scans combined create the 3D scan. The patient receives more radiation during CT than during a standard X-ray as CT use ionizing radiation to make multiple images [13].

The spatial distribution of the linear attenuation coefficient (μ) is measured and computed by the CT [20]. To describe radiodensity CT uses Hounsfield Unit (HU) as pixel information. The different tissue-electron densities in the image are represented indirectly by HU. HU for a substance is given with equation 2.8, with the substances μ: linear attenuation coefficient, and the known coefficients of water and air [20]. By doing this, various tissues can be distinguished by their HU values.

$$HU = 1000 \times \frac{\mu - \mu_{water}}{\mu_{water} - \mu_{air}} \tag{2.8}$$

CT is the most important imaging tool to decide the extent of the primary tumor, the T value of the staging [10]. To improve imaging, there are many conceivable CT extensions. Some hospitals have 4D CT. This is respiratory correlated CT, that by having scans in different breathing phases can create a visualisation of the motion while the patient breathes. With 4D CT an Average intensity projection (AIP) image can be made. This takes the average of each phase to create on CT scan. 4D CT is usually used in treatment planning of NSCLC. Another type of CT that can be used is contrast CT, where and intravenous radiocontrast is used. It enhances the capacity to distinguish between biological tissues, to see structures like blood vessels better [21]. Not all patients can be subjected to the contrast liquid, due to reasons like allergies or loss of kidney function.

Another image modality much used for treatment planning of lung cancer is PET-CT. In addition to taking a CT scan, a radioactive tracer is injected into the patient, that can be detected when it decays. PET with [^{18}F]-fluoro-2-deoxy-glucose (FDG) and CT for anatomical images, is a common tracer, called PET-FDG [11]. The tracer is injected to the patients body, and it will travel where there is highest metabolic activity, with high uptake of glucose [22]. Most cancer cells have a high uptake of glucose, so these will also have a high uptake of the FDG [11]. More radioactive material will decay in the cancer cells, and this radioactive decay will be reported at that specific anatomical location of the cancer cells [22]. Staging also makes use of FDG-PET, which gives higher accuracy in diagnosis of lymph nodes, and decide the N-value in

the TNM staging [11]. PET-CT performs particularly well at identifying metastasis, the M-value for staging [11].

2.5.2 Contouring

By utilizing CT images, it becomes possible to delineate the shape and location of the tumor, which serves as the target for irradiation. The definition of the target volume in done in multiple steps. The gross tumor volume (GTV) is the exact tumor volume one can detect on images. The next is the clinical target volume (CTV), which includes the tumor and the potential microscopic tumor spread. Internal target volume (ITV) is an additional volume that includes an inner margin with variations in motion, shape, and CTV position. The largest volume is the planning target volume (PTV), which also takes into account setup variations of the CTV. These are illustrated in Figure 2.13. The OARs are also contoured in this stage. An OAR is nearby healthy tissue or an organ that could be damaged with the radiation [23], and varies depending on the tumor location.

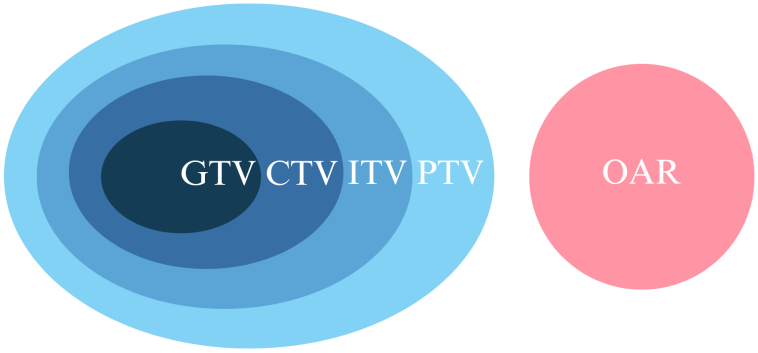

Figure 2.13: Illustration of placement of target volumes. Gross target volume (GTV), clinical target volume (CTV), internal target volume (ITV), planning target volume (PTV) and organ at risk (OAR).

When planning and calculating the risk of injury to OARs it is important to take into account if it is a serial or parallel organ. For a serial organ, like the spinal cord, the loss of function in one part of the organ will cause the entire organ to loose function [17]. This means that a high dose to a small area can cause critical damage, and the risk of injury is determined by the highest dose. Therefore, radiation therapy planning aims to minimize the dose to the most sensitive parts of the organ while still delivering an effective dose to the tumor. In a parallel organ, like the lungs, the loss of function in one part does not affect the other parts of the organ [17]. The risk of injury is determined by the average dose over the whole organ volume. The risk of injury increases as the

average radiation dose to the whole organ increases, regardless of whether the radiation is delivered evenly or unevenly within the organ [17]. Therefore, when planning RT, it is important to consider the total dose to the entire organ and not just the dose to a specific point or region within the organ.

2.5.3 Planning and Treatment Techniques

There are different goals of radiation to the tumor and restrictions to the dose to the OARs. All of these are taken into account in the next stage, the individual RT planning. Here the beam arrangement and the dose distribution are decided. There are different types of treatment planning styles in RT. The first is forward planning, in which the dose distribution is determined through a process of "trial and error", until a treatment plan that satisfies both the dose to the target and the OARs is created [12]. Inverse planning is another type where the aim is first made known to the system being utilized. These aims are given with specified objectives, the measure of how well satisfied the set dose to target is with the plan, and constraints, the maximum doses to the OARs [12].

Three-Dimensional Conformal Radiation Therapy (3D-CRT) is a photon therapy beam delivery technique based on forward planning. 3D CT/MRI images are used for dose calculation and contouring of PTV and OARs. Multiple fields around the tumor is used, and each is set up based on how the tumor looks i the direction of the radiation, using multileaf collimators. Three or more fields are used, to reduce the dose to healthy tissue. In each field the tumor gets a homogeneous dose. The delivery of photon beams using the intensity-modulated radiation therapy (IMRT) method is based on inverse planning. In each field there is a variety in intensity of the radiation, which in the end gives a homogeneous dose to the tumor [12]. Volumetric modulated arc therapy (VMAT) is another inverse planning technique. In contrast to IMRT, VMAT rotates constantly to reduce the dose to the surrounding healthy tissue. Less fractions are used in stereotactic ablative body radiotherapy (SABR), which usually delivers doses ranging from 6 Gy to 30 Gy [12].

For delivery of protons, there is a difference in beam spreading between passive beam spreading and pencil beam scanning. The simplest method is passive beam spreading, using thin sheets as scatter material for the proton beam [12]. Pencil beam scanning use magnets to direct the proton beam. Pencil beam scanning PT includes various techniques. Single Field Uniform Dose (SFUD) is a technique where every field delivers a homogeneous dose. Similar to IMRT, intensity-modulated proton ther-

apy (IMPT) uses protons instead of photons, and creates a homogeneous dose to target [12].

2.5.4 Evaluation and QA

The plan is evaluated with different parameters, some that can be seen with a dose volume histogram (DVH). DVH is used to describe the distribution of the dose in chosen target or OAR. In RT cumulative DVH is most often used. From the DVH much information about the dose can be found. It is possible to assess the dose to the structures using various metrics. Dx%Gy provides the dose in Gy that x % of the entire volume of the structure receives. VxGy shows the volume, often presented in percentage, that receives x Gy or more with the plan. Other dose parameters are mean, min and maximum dose to a structure. With the DVH, several treatment plans can be compared. The goal is to develop a treatment plan that achieves a high dose to the target while minimizing the dose delivered to the OARs. Finally, a quality assurance (QA) process or treatment plan verification is conducted.

2.5.5 Treatment Delivery

All of these steps before treatment usually happen in a week, around a day for each. The next week RT begins, with usually five fractions a week, one every weekday, over five to seven weeks, as illustrated in Figure 2.14. This helps the healthy tissue to not be as damaged by the radiation. With doses in fractions the radiation is also less efficient in causing cell death. Normal tissue is typically better at self-repair than cancer cells, and fractionation makes use of this advantage by giving the normal tissue time to do so [24].

Figure 2.14: Illustration of workflow in radiotherapy. Can both see the different stages before treatment, and the fractions of radiotherapy.

2.5.6 Radiotherapy of LA-NSCLC

The recommendation from the Norwegian Radiation Protection Authority is that suitable patients in good general condition with stage IIIA-IIIB NSCLC should be offered combination therapy with concurrent platinum-based chemoradiotherapy with a radiation dose of 60-66 Gy [25]. This is given in 2 Gy fractions 30-33 times, in combination with chemotherapy.

The RTOG-7301 trial set the standard in 1980 for RT to patients with stage III NSCLC [26]. In 2015 this was still fractions of 1.8-2.0 Gy, with a total of 60-63 Gy [1]. Bradley et al. tried with the RTOG-0617 trial to increase this total dose to 74 Gy, and compare with patients receiving 60 Gy. They found that the high-dose radiation was not better than 60 Gy, with shorter median overall survival. They also found that overall survival for the patients was negatively associated with cardiac irradiation, as there were no dose constraints for the heart with high-dose [1]. They concluded that 60 Gy should remain the standard treatment total dose for these patients. A recent analysis of this trial revealed that the dose administered at the heart's base had a significant impact on the trial's poorer overall survival [27].

Dillman et al. discovered in 1990 that sequential administration of chemotherapy before radiation therapy, sequential chemoradiotherapy, resulted in improved survival rates for patients with stage III NSCLC [28]. The RTOG-9410 trial, published in 2011 by Curran et al., revealed that administering chemotherapy simultaneously with radiation therapy, concurrent chemoradiotherapy, was more beneficial for patients [29].

Today there is no routine for using protons in treatment of lung cancer [11]. The advantages of the depth dose characteristics of PT have the potential to minimize the adverse effects in LA-NSCLC patients. For example, Elhammali et al. achived satisfactory results from treating 51 patients with LA-NSCLC with IMPT and concurrent chemotherapy [30]. One of the benefits found from using PT on stage III NSCLC is a reduction of the dose to the heart [31].

2.6 The Heart as an Organ at Risk in Radiotherapy

Mediastinal irradiation refers to the use of RT to the mediastinum, the central region of the chest between the lungs. The mediastinum contains the heart, major blood vessels, thymus gland, esophagus, trachea and lymph nodes. This makes the heart an OAR

in treatment planning of radiation to tumors in the lungs, among other cancers. Heart toxicity is rarely reported as a side effect of RT of tumors in the lungs [11]. The cause of this is that not many individuals who receive treatment for this survive long enough to experience heart-related side effects. One can think that these side effects increase as the survival rate increases.

2.6.1 Grading

The patient focus for multiple studies on radiation to the heart is overall survival (OS), and death related to radiation to the heart [1, 32, 33]. Some use the Common Terminology Criteria for Adverse Events (CTCAE), a set of criteria to classify different side effects from cancer treatment [34, 35, 36, 37]. There are many different cardiac disorders listed and graded in CTCAE. Studies often groups patients $\geq$ grade, to get a sufficient amount of patients. Generally, grade 1 is asymptomatic or mild symptoms, grade 2 is moderate, grade 3 severe, grade 4 has life-threatening consequences, and grade 5 is death [34]. Others use the general term major adverse cardiovascular events (MACEs), which covers a variety of heart conditions and criteria [38]. A similar term used is major coronary events (MCEs) [39].

2.6.2 Radiation Induced Heart Disease

There are indications that chest RT can increase the risk of heart disease. Studies on radiation induced heart disease (RIHD) have been conducted for numerous cancer types, including lung, esophageal, breast, and lymphoma. Several distinct heart conditions have been observed to develop with RT. According to estimates, the incidence of RIHD ranged from 10% to 30% 5 to 10 years following treatment, depending on the kind of cancer and the year of RT [40]. According to a study by Pan et al., RT for lung cancer increases the risk for cardiac death by nearly 30% [41]. It is important to remember that many of the studies are based on radiation with old techniques. Radiation induced acute illness is uncommon, it is more common with a long incubation period before symptoms manifest.

Pericardial Disease

The most usual RIHD is pericardial disease. Acute pericarditis, pericardial effusion, or constrictive pericarditis are the most common manifestations of pericardial disease [5]. Acute pericarditis is an inflammation of the pericardium. The main symptom for acute pericarditis is pain to the chest. Although the prognosis for acute pericarditis is good

and it often only lasts a few weeks with treatment, sudden death can still occur [5]. It usually manifests early, within days or months, while constrictive pericarditis develops later, within months or years. A thick, fibrous, and calcified pericardium is indicative of constrictive pericarditis [5]. The heart is then enclosed in a rigid shell and is unable to adequately fill. When there is an excessive quantity of fluid in the pericardial sac, it is called a pericardial effusion. This condition can put pressure on the heart and affect how well it functions. Cardiac tamponade occurs when the pericardium is unable to expand, which obstructs the filling of the ventricles of the heart [5]. Exposure of radiation to thorax tumors can lead to damage to the pericardium, which may cause the accumulation of fluid in the pericardial sac (pericardial effusion) and the development of pericardial fibrosis [5].

There are many studies that have correlated radiation with pericardial disease. The risk of pericarditis increase with the radiation dose [39]. A study by Heidenreich et al. studied 294 patients treated with $\geq$ 35 Gy for Hodgkin's lymphoma, a cancer in the lymphatic system. A time after treatment they found that 21% of the patients got a thickening of the pericardium [42]. Wei et al. aimed to identify the risk factors associated with pericardial effusion in patients with esophageal cancer who underwent RT. Their findings indicated that the incidence of pericardial effusion could be minimized by lowering the dose-volume administered to the pericardium and heart [43]. By incorporating the heart chambers as substructures in the model, Niedzielski et al. discovered that their regression model for predicting pericardial effusion CTCAE $\geq$ 2 for NSCLC patients predicted more accurately [35].

Valvular Disease

Valvular heart disease (VHD) is another potential RIHD. According to Gujral et al., radiation exposure to the thorax area can result in valve fibrosis and calcification, leading to regurgitation and stenosis [44]. Regurgitation, also known as valve insufficiency, is when a valve does not close tightly, causing blood to flow backward through the valve [5]. A result of this can be decreased blood flow to the body. Stenosis is when a heart valve becomes narrowed or blocked, reducing the amount of blood that can flow through it, and makes it harder for the heart to pump to the body [5].

The incidence of RIHD varies depending on the direction of radiation administered during cancer treatment. Studies have indicated that patients who underwent left breast cancer therapy have a higher incidence of RIHD, particularly a higher incidence of

VHD [45]. More specifically aortic valve disease, often as aortic regurgitation, is the most common manifestation of VHD. Chang et al. After gathering various RIHD information, and their statistics on radiation induced VHD (RIVHD), x years after treatment, is in Table 2.2. According to research by Cella et al, receiving doses > 25 to 30 Gy to a higher volume of the LA and LV enhanced the likelihood of developing mitral and aortic valve disease [46]. In their research, Cutter and colleagues examined survivors of Hodgkin lymphoma to investigate the incidence of radiation-induced valvular heart disease (RIVHD). They observed that exposure to radiation in the valve area could raise the likelihood of developing VHD, with the risk escalating with radiation doses surpassing 30 Gy and increasing in proportion to the dose [37].

Table 2.2: Statistics of valvular heart disease from research. Collected by Chang et al. [47]. R: regurgitation, S: stenosis.

	Aortic R	Aortic S	Mitral R	Triscuspid R	Pulmonic R
10 years	26%	-	39%	16%	7%
20 years	60%	16%	52%	26%	12%

Conduction System Malfunctions

Another possible RIHD is abnormalities in the conduction system. This happens when the radiation causes inflammation or lack of blood flow to the heart, which leads to a build-up of fibrosis. The fibrosis can affect the heart's ability to conduct electrical signal properly, which can cause problems with the heart's rhythm. The most common manifestation is infranodal and right bundle branch block (RBBB) [48]. An infranodal block is a heart block that occurs below the AV node and the bundle of his, and can affect the ventricles ability to receive electrical signals from the atria, leading to abnormal heart rhythms. RBBB is a heart block that occurs when the electrical signals that travel through the right bundle branch of the heart's conduction system are delayed or blocked.

A study by Adams et al. found that of 48 young (diagnosed $\geq$ 25 years of age) Hodgkin's disease survivors 75% of them had conduction defects after mediastinal irradiation, 5 to 27 years after diagnosis [49]. A different study discovered that out of 13 individuals who received SABR treatment for lung cancer, one patient developed sick sinus syndrome and required a pacemaker implant. This particular patient was elderly (83 years old) and received a high radiation dose of 40 Gy to the sinoatrial node, which was the third highest dose among all the patients [50].

Cardiomyopathy and Heart Failure

Cardiomyopathy and heart failure (HF) are further potential RIHDs. Cardiomyopathy is a condition that affects the heart's ability to pump blood efficiently, which can result in HF. Dilated, hypertrophic, and restricted cardiomyopathy are the three most prevalent forms [5]. In dilated cardiomyopathy, the left ventricle and/or right ventricle is enlarged and weakened, limiting the heart's capacity to pump blood. With hypertrophic cardiomyopathy, the muscle thickens abnormally, making it more difficult for the heart to pump blood. Restrictive cardiomyopathy occurs when the heart muscle becomes stiff and less elastic. This makes it more difficult for the heart to expand and fill with blood. HF happens when the heart is unable to pump enough blood to meet the body's needs, and can either be acute or chronic [5].

Radiation induced heart failure typically develops gradually over several years after RT. Radiation of the heart can cause diastolic dysfunction and fibrosis, key features of restrictive cardiomyopathy [51]. According to Chang et al. cardiomyopathy happens to up to 10% of RT patients with irradiation to the heart, most often as restrictive cardiomyopathy [47]. Nimwegen et al. did a study that showed that there was higher HF risk with an increased mean dose to LV, with CTCAE ≥ 2 [36].

Coronary Artery Disease

Another RIHD is coronary artery disease (CAD). Coronary artery disease is a condition where there is a buildup of plaque in the coronary arteries, which can lead to narrowing or blockage of these arteries. This can result in reduced blood flow to the heart muscle, that can cause chest pain or discomfort known as angina. Ischemic heart disease (IHD) can be caused by various factors, one of which is CAD. This reduced blood supply can lead to injury or death of heart cells.

According to Chang et al. CAD usually occurs 10 years after RT [47]. One study found that the rate of CAD was proportional with the mean heart dose for women treated with RT for breast cancer [52]. In a study conducted by Tagami et al., it was discovered that there was a significant association between the mean radiation dose received by the LAD and the occurrence of CAD. The study revealed that for every Gy of radiation exposure to the mean LAD dose, there was a 21% increase in the incidence of disease in the LAD [53].

Further Research

Tjong et al. conducted a retrospective study on patients with LA-NSCLC, analyzing the relationship between the dose administered to the LAD and a broad selection of cardiac events and death, with the aim of developing a predictive model for such events. One of their key findings was that the dose-volume to LAD was a significant factor among others [38]. Wang et al. also conducted a retrospective study on the radiation dose to substructures in patients with esophageal cancer. Their study revealed a significant correlation between the radiation dose administered to the LAD and LMCA and both MCEs and OS [39]. Duane et al. conducted a retrospective study spanning four decades (1970-2009) on women with breast cancer. Their findings indicated that the treatment approaches utilized during this period increased the risk of both IHD and VHD, but the risk has decreased with the introduction of newer techniques [54]. Vivekanandan et al. investigated the correlation between radiation doses to the heart, OS, and the consequent changes in the heart. Their research revealed that patients who exhibited conduction abnormalities or ischemic/pericarditis-like changes six months after treatment and those who received higher radiation doses of 63-69 Gy to larger heart volumes had a higher mortality rate [33].

Reducing the Risk of RIHD

Exceeding specific dose thresholds can increase the risk of adverse cardiac side effects. This includes pericarditis ($\geq$ 35 Gy), cardiomyopathy ($\geq$ 35 Gy), injury to coronary artery ($\geq$ 30 Gy), valvular injury ($\geq$ 40 Gy) [55]. Ischemic heart disease is reported as the most usual contributor to heart related deaths [56]. Therefore there is recommended to limit the volume of the heart that is irradiated with high doses, above 35 Gy. The Norwegian Lung Cancer Group (NLCG) recommends following dose constraints: V50 Gy < 25%, V45 Gy < 60%, V40 Gy < 80%, Mean heart dose (MHD) < 20 Gy [11]. In the clinics today the heart is contoured and as a whole, despite the fact that it is composed of numerous distinct parts. The Quantitative Analysis of Normal Tissue Effects in the Clinic (QUANTEC) group published in 2010 a guideline to recommended dose-volume limits for each OAR, including the heart. One of the QUANTEC group suggestion for future toxicity studies was that "additional study is needed to relate doses to subvolumes of the heart (e.g., coronary arteries) to clinical outcomes" [57].

Chapter 3

Materials and Methods

The study approach, data collection methods, and materials used in this project to accomplish the research objectives are all described in this chapter. It covers the patient material used in the project, as well as the initial literature search that was done to determine the substructures that would be contoured. The process of preparing and implementing the contouring is also detailed. Furthermore, various substructure analysis approaches are investigated, and an overview of the tools utilized by the candidate for this purpose is provided.

3.1 Literature Search

The selection of the heart's substructures for investigation and contouring is a crucial component of this project. Initially the candidate performed a literature search to get an overview of existing knowledge on the heart as an OAR in RT. Learning about the structure of the heart was crucial to this literature search. The candidate attended a number of Human Physiology seminars while the topic of circulation was being discussed. Gaining further knowledge about the cardiac structures revealed the significance of various components, such as the heart chambers, valves, blood vessels involved in circulation to and from the heart, coronary arteries, specialized cells responsible for heart rhythm regulation, and the pericardium surrounding the heart. This understanding highlights the importance of considering these individual elements in addition to the heart as a whole. The goal was to identify which substructures that were possible to contour, how these were contoured, and assess the correlation between the administered dose and the recorded side effects.

The candidate focused on research on RIHD that studied other parameters than the standard whole heart, to see which substructures were most often mentioned in differ-

ent articles, and could have a possible correlation with disease or death. These studies cover a variety of radiation techniques as well as other thoracic cancer forms besides NSCLC, with different doses and fractions in the RT. The candidate used PubMed with different search words, to find fitting articles. The candidate discovered that it was effective to use references from research that appeared relevant to the subject, particularly those that examined RIHD. For each article's evaluation the candidate took into account a variety of factors, including the study's size, type of treatment, and publication year. This is all illustrated in Figure 3.1.

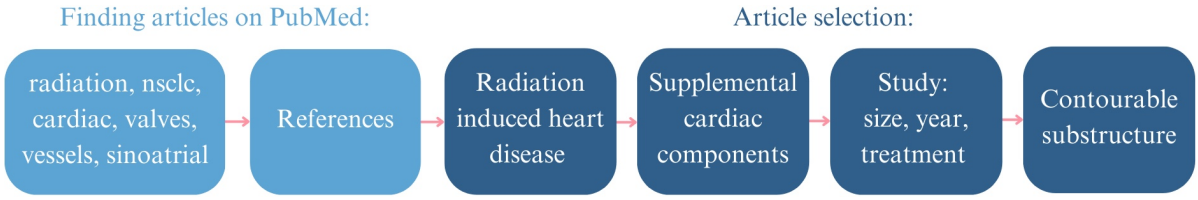

Figure 3.1: Illustration of the literature search process.

3.2 Patient Material

In this project the prospective data from the pulmDIBH-study at HUS (REK 2019/749) was utilized. This study included patients treated for NSCLC, treated with RT with curative intent, and a curative fractionation regime. All patients had given their written agreement to participate in the study and the patient data had been deidentified. This retrospective project includes 15 of the patients in the study, as there were already created proton treatment plans for the patients. The selected patients had a diagnosis of NSCLC stage III, treated with RT in 2019-2020. The median age was 65, ranging from 53 to 75 years old. Further patient characteristics can be found in Table 3.1.

Table 3.1: Patient characteristics, disease extent and radiotherapy.

Stage	**N. of Patients**
IIIA	9
IIIB	5
IIIC	1
Target Volume	
Primary tumor and mediastinal lymph nodes	13
Primary tumor	1
Mediastinal lymph nodes	1
Primary tumor location (lobe)	
Left upper	3
Left lower	3
Right upper	4
Right mid	0
Right lower	3
Prescribed dose	
60 Gy	6
66 Gy	9

The data used included the patients' prospectively collected image data. The image data collected from the patients were CT scans at treatment planning and week 1 into the RT treatement period. All 15 participants completed four dimensional CT (4DCT) scans during both treatment planning and week 1, with 10 breathing phases, as 10 distinct scans. This was used to create an average intensity projection four-dimensional CT (AVE-4D-CT) by a dosimetrist at HUS. 9 of the 15 patients took contrast CT scans additionally to 4DCT during treatment planning. Omipaque 350 mg/ml (GE Healthcare, USA) was administered intravenously at a flow rate of 3 ml/S. Not all patients in the project could be given this contrast liquid, due to required functional kidney function. The patients who could were only given contrast in their first scan, in treatment

planning, to avoid increasing their risk of side effects.

The CT scans followed a specific protocol for the study at HUS, and were done by radiation technologists. The patients were placed in Philips Brilliance Big Bore (Philips Healthcare, Best, The Netherlands). On the CT-table they were placed in head-first supine position, with their arms fixed above their head in the thorax fixation equipment (Posirest™-2, Civco Radiotherapy, Coralville, Iowa, USA). Additional support included a neck pillow, a thin mattress, and knee support.

The previous research conducted on the same patient material allows for the enabled reuse and additional analysis of projects carried out by other researchers. Prior to this project, the AVE-4D-CT scans from treatment planning and week 1, the organs at risk had previously been contoured by dosimetrists and approved by the responsible oncologist. This included contouring of the heart structure that was used in this research .

In this project, Kristine Fjellanger's simulated plans for the 15 patients receiving both photon and proton therapy were used. The plans were created by using automatic planning, of intensity-modulated during free breathing RT [58] and PT. The prescribed dose was 60-66 Gy, given in 2 Gy fractions.

3.3 Contouring of Heart Structures

3.3.1 Definition of Scans

Three sets of drawings were produced for each patient, which are now defined seperately as:

i) C.plan: rapid contrast CT scans in planning stage of treatment (n = 9).

ii) A.plan: AVE-4D-CT in planning state of treatment (n = 15).

iii) A.w1: AVE-4D-CT in week 1 of treatment (n = 15).

3.3.2 Selection and Description of Atlases

The candidate studied the following atlases to contour the selected substructures. A cardiac contouring atlas by Duane et al. was recommended by a representative from the Department of Oncology and Medical Physics at HUS [59]. The atlas by Socha et al. was found to be used for contouring of the four heart valves, as it is not covered in

Duane et al. [60, 59]. Loap et al. was found to be used to contour the electrical conduction system of the heart, the sinus node and the atrioventricular node [61]. All of the atlases used are made for non-contrast CT scans. This can make the rules and images more difficult to follow, and the result can be more dependant on the candidate.

3.3.3 Procedure for Contouring

While working with the supervisor, the applicant created a structure template to be used for adding the substructures to each CT scan in Eclipse (Varian Medical Systems, Palo Alto, CA, USA). The color system for the structure template made can be seen in Figure 3.2. This resembles the color scheme in the atlas by Duane et al. [59]. By doing so, confusion when utilizing this atlas to contour substructures will be avoided. This color system also needed to follow the usual standard at HUS, for example that red contouring is reserved to the PTV. This information resulted in a template with structure ID and colors to all of the 19 selected substructures. In this template some of the structures were named incorrectly.

3.3.4 Contouring and QA

Figure 3.3 illustrates the order of action in the contouring process, while Figure 3.4 represents the order of contouring of the structures by the candidate. All of the contouring was done in Eclipse (Varian Medical Systems, Palo Alto, CA, USA) in "breast mode", a level preset with lower level -250 HU and upper level 150 HU. The transversal plane was mostly used.

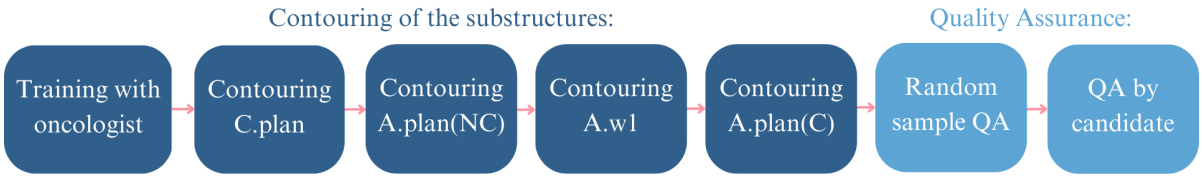

Figure 3.3: Illustration of order of action in the contouring process. NC (Non-Contrast) represents patients who did not undergo C.plan scans, while C (Contrast) represents the patients who did.

[1]The image was made by the candidate, inspired by [59], using canva.com.

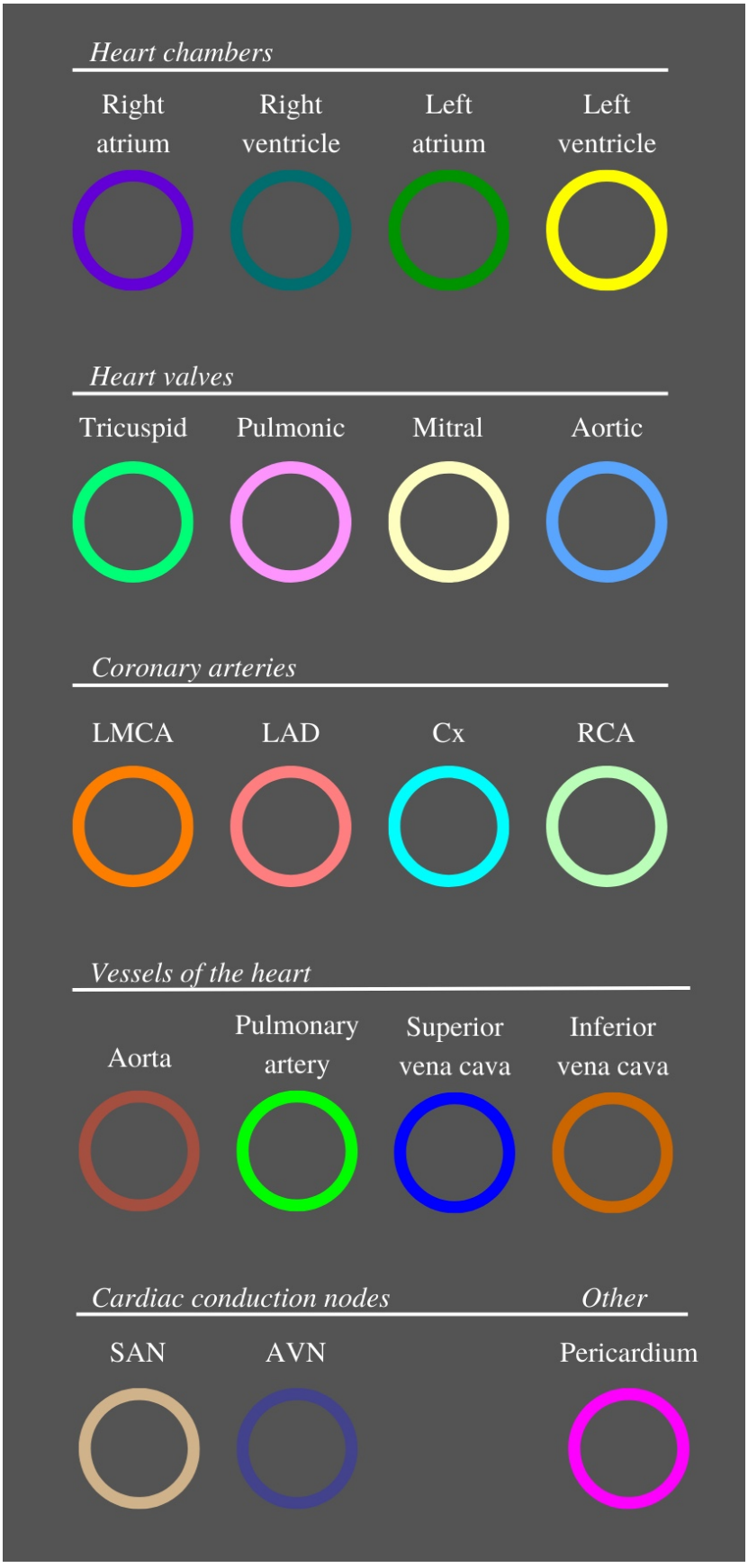

Figure 3.2: Color system for contouring selected substructures. Credit [1].

1. Aortic valve
2. Pulmonic valve
3. Pulmonary artery
4. Superior vena cava
5. Aorta
6. Inferior vena cava
7. Right atrium
8. Left ventricle
9. Right ventricle
10. Left atrium
11. AVN
12. SAN
13. LAD
14. LMCA
15. Cx
16. RCA
17. Tricuspid valve
18. Mitral valve
19. *Heart*
20. Pericardium

Figure 3.4: Illustration of order of contouring of substructures. The difference in color differentiate the different groups of structures.

Training with Oncologist

In order to learn how to recognize the various structures, patient 04 C.plan was initially contoured in collaboration with HUS oncologist and co-supervisor Inger Marie Sandvik. The candidate was sufficiently capable to carry out contouring independently after this.

Contouring of C.plan

To further train and prepare the candidate for drawing in images without contrast enhancement, A.plan and A.w1, contouring was first done on patients with C.plan. This could also be used to later compare the contouring with and without help from the contrast.

The four cardiac valves' contours were determined by the candidate using the atlas by Socha et al. [60]. The atlas has slice separation of 2.5 mm, while the data in this project has 3 mm. The aortic and pulmonic valves were both specified to have a length of 7.5 mm, however in this project, the length was increased to 9 mm to provide substantial substructures. They were both drawn by their definitions, in four slices. If the top slice of the pulmonic valve was defined outside of the heart, the valve started a slice below the definition from the atlas.

The candidate used Duane et al. to draw the heart chambers, vessels of the heart and coronary arteries [59]. The section of the pulmonary artery visible from the slice just above the pulmonic valve was outlined, focusing solely on the portion directly linked to the heart. The superior vena cava was contoured from one slice above the pulmonary artery, to where the right atrium was seen. The aorta was contoured from the top where it could be identified, to the aortic valve was defined and the dorsal artery to the end of the delineation of the heart. The inferior vena cava was contoured from where it sepa-

rated from the right atrium to the end of the delineation of the heart.

The heart chambers were drawn where they could be identified. The left ventricle was defined to take up the space of the aortic valve in the slice below its last slice. Nodes were contoured by the candidate as suggested in, as 2 cm spheres, overlapping other strucures [61]. The coronary arteries varied in how easily they could be identified, but were contoured with brush of 4 mm. They were all contoured within the previously contoured heart structure. Here, the sagittal and frontal planes were also utilized. With an 8 mm diameter brush where the margins of the atria and ventricles were close to one another, the tricuspid and mitral valves were contoured as indicated in the atlas [60].

On C.plan the whole heart was also drawn by the candidate, following the beginning and end already drawn on A.plan, but adjusted to the heart with contrast liquid. These hearts were utilized to shape the pericardium by acting as the heart's wall, to create a rim volume. The pericardium is found to be maximum 2 mm thick [62]. Therefore the candidate tried to create the volume with 2 mm walls, but these created disrupted volumes in many of the images. As a result, on all scans, the wall was extended to 3 mm in order to obtain a thin but continuous volume.

Contouring of A.plan and A.w1

Eventually the candidate performed contouring on A.plan and then A.w1, using the same atlases and definitions as for C.plan. They followed the atlases in the same manner as the contouring process for C.plan, adhering to the guidelines. The coronary arteries were a challenge because they are small and challenging to contour, especially in AVE-4D-CT scans, they were difficult to locate. Consequently the contouring of the coronary arteries were typically not a precise location but rather an indication of where they would likely be. Since the coronary arteries are vessels the focus was that the drawings were connected between slices, to make whole functional vessels.

The motivation for drawing on AVE-4D-CT is that these scans are often being used in treatment planning. Drawings cannot fully rely on the availability of contrast pictures because contrast CT scans like C.plan are not always available. With AVE-4D-CT breathing motion is included in the scan, which can affect the placement of the heart structures.

Quality Assurance

Without using excessive resources, the quality might be guaranteed by taking a random sample and then having the candidate perform quality control. Therefore, the oncologist co-supervisor and supervisor collaborated to perform a quality control assessment using a random sample. With the feedback from the quality control the candidate could perform a quality control on each patient, on C.plan, A.plan, and A.w1. This was done to lower the likelihood of variations resulting from the contouring order of the images.

3.4 Geometric Comparison

By using the metrics, the patients' structures could be compared. There were two comparisons of interest in this project, defined below. Comparison of a) will show breathing motion uncertainties and contouring inconsistency in the CT scan, while comparison of b) will on the other hand display day to day changes for a patient, antomical change over time.

a) Quantitative Comparison between C.plan and A.plan.

b) Quantitative Comparison between A. plan and A.w1.

3.4.1 Definition of Metrics for Comparison

Three metrics are being used to study the structures: Volume of the structure, Dice similarity coefficient and Hausdorff distance 95% percentile, later referred to as:

i) V: Volume of the structure, calculated by DVHToolKit, created by Helge Egil Seime Pettersen.

ii) D: Dice coefficient, comparing A.plan with either C.plan or A.w1.

iii) H: Hausdorff distance 95% percentile, comparing A.plan with either C.plan or A.w1.

Volume

Volume of the structures were extracted by the candidate by using DVHToolKit, created by Helge Emil Seime Pettersen, a medical physicist at HUS [63]. This includes many dose metrics in addition to volume, so the candidate removed the dose metrics from the file by using Microsoft Excel (2016)[64]. This file was used in a new script,

to change the volume to the same format as D and H, to be used together. This script can be seen in Appendix B.1.

Dice Coefficient

Dice coefficient, also called Dice similarity coefficient or Sørensen-Dice coefficient, is a statistical tool used to compare overlap of data [65]. In this project the data is CT slices with areas of the different structures. The formula for calculating Dice coefficient of areas is given in Formula 3.1, and an illustration is seen in Figure 4.6. Defining a "good" Dice coefficient value for all structures is challenging because of the distinct differences in their size and shape. A Dice coefficient, which ranges from 0 to 1, describes how well structures "overlap," with 1 indicating complete overlap and 0 indicating no overlap.

$$Dice = 2 * \frac{|A \cap B|}{|A| + |B|} * 100\% \tag{3.1}$$

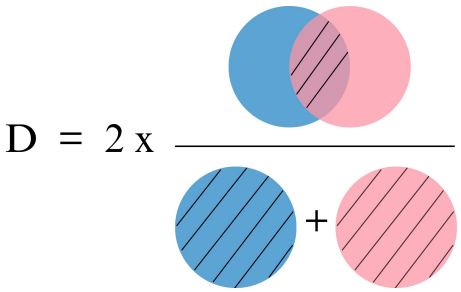

Figure 3.5: Illustration of calculation of Dice coefficient for two circles. Their areas are marked with lines.

Hausdorff Distance 95% Percentile

Another metric is Hausdorff distance, explained as the longest distance from on point in data A to data B, taking the shortest possible road. Hausdorff distance 95% percentile, illustrated i Figure 3.6, is the 95% percentile of all the distances from all points of the data. The optimal H value may vary depending on the specific structure being considered, as each structure has unique characteristics. In general, a low H value is desirable as it corresponds to a shorter distance between the structures.

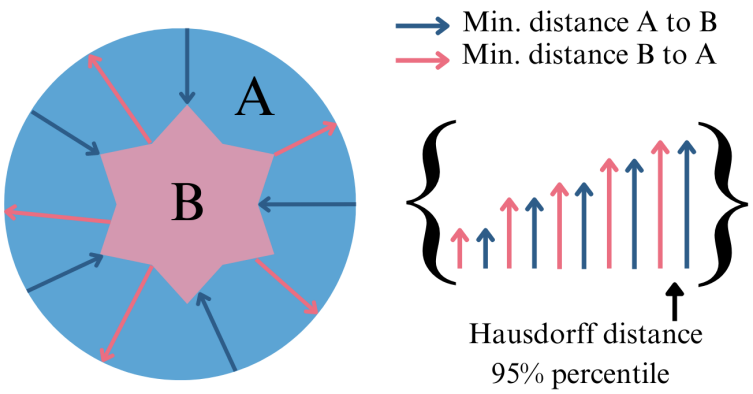

Figure 3.6: Illustration of calculation of Hausdorff distance 95% percentile. Different shortest distances from A to B are illustrated as arrows, and are lined up after size, the 95% percentile can be found.

3.4.2 Usage and Creation of Python Scripts

To geometrically compare the drawn structures, the candidate was given a Python script written by Helge Egil Seime Pettersen. To use this the candidate exported the structure sets from Eclipse (Varian Mediaval Systems, Palo Alto, CA, USA). Input images and DCM files with structures were handled by the script, which then used them to calculate and display the Dice similarity coefficient, Hausdorff distance 95% percentile, and mean surface distance on the slices. The code was modified by Pettersen to accommodate the candidate structures, which involved comparing structures within the same image rather than in different files, as the script was originally intended to do. In order to prevent errors, Pettersen also updated the script to only use the slices that contained both of the structures being compared.

From Eclipse, the candidate exported the patients for later analysis. Additionally, the candidate updated the code by Pettersen so that it could accept numerous patients at once and matched the names and structures in the script to this given instance. The colors of the drawings were set by the candidate to be the same as the colors used in Eclipse. Volume similarity and Hausdorff distance were introduced to the script's metrics by the candidate, in case it was found useful later in the project. Using this tool, the candidate could compare the initial planning's A.plan with two or three alternative versions of the structures. These versions involved contouring on A.w1, transferring placement using both 3D and 6D for 12 patients (excluding 3D for two patients and 6D for one patient). Additionally, contouring on C.plan was included for nine patients. The modified code for this can be seen in Appendix B.2, and the accompanying classes made by Pettersen in Appendix B.3.

For all patients, except one who exclusively underwent a 3D transfer, the script uti-

lized only the 6D transfer from A.w1. In the case of the patient who had the 3D transfer, it was necessary to employ that specific transfer. The candidate also modified the script to exclude wrongly calculated outliers of D and H, before using the metrics. With the script all of the data was put in the same file for later use. The script can be seen in Appendix B.4.

To calculate the mean D and H values for each structure individually, a script was developed. This script was designed to analyze data from all patients collectively, incorporating the standard deviation as a measure of uncertainty. In this script the D and H values were put together with the corresponding volumes. This script can be seen in Appendix B.5.

3.5 Dose

There were three comparisons of interest in this project, while studying the patients' structures, defined below. a) concerns differences between planned and actually delivered dose to the patient. This is in this project illustrated as the differences in dose between A.plan and A.w1. In this scenario, if the dosage remains consistent throughout this time, it is characterized as being robust. b) illustrated the differences in physics of the two beams through a patient. c) examined the variances in the dose received by the heart and the substructures, and investigated whether the heart accurately reflects the dose delivered to the substructures.

a) Robustness of treatment plan for photon and proton beam.

b) Comparison of dose from photon beam and proton beam.

c) The heart as a surrogate parameter for the substructures.

3.5.1 Literature Search

Expanding the initial literature search the different DVH metrics the studies used for substructures could be found by the candidate. This decided which dose metrics the candidate would study in this project. The options were dose[Gy] at volumes [%], volume [%] at doses [Gy], and volume [%] at doses [% of max], in addition to Dmean, Dmax and Dmin. To ensure comparability with this project, only studies that employed a similar total dose were selected. As a result, studies that focused on substructures of Hodgkin's lymphoma, where the total dose typically falls below NSCLC, were excluded. The study was also only included if the "Best dosimetrics" was specified, and

a known parameter of the previously chosen substructures for this project, not for the whole heart.

3.5.2 Retrieval of Dose Parameters

DVHs for photon beam RT were manually exported from Eclipse by the candidate. To export DVH curves for PT from Raystation (RaySearch Laboratories, Stockholm, Sweden) the candidate had to:

a) Export structure sets from Eclipse for each patient (n = 15 x 2 = 30).

b) Import structure sets (n = 30).

c) Frame of reference registration and register imaging system (n = 4).

d) Week 1 (and cases from iii)): compute on additional sets from existing free breath plans with PT (n = 15 + 4 = 19).

In addition the average dose to the structure with PT had to be manually written to a table by the candidate for use in analysis. Due to technical errors the candidate was not able to get the average dose for one of the 15 patients.

For three patients additional modifications had to be done to compute the doses. These modifications were primarily done by co-supervisor Fjellanger. For two of the patients the holes on the structure "BODY" drawn prior to this project had to be fixed. For another patient there was an issue concerning a structure outside of the dose grid in A.w1. This was solved by extending the dose grid.

3.5.3 Usage and Creation of Python Scripts

To get the DVH values from the exported files from Eclipse and Raystation DVHToolkit was used [63]. The script had to be edited, in a single line, by the candidate to match the current version of DVH file output of Raystation. The candidate created a script to transform the data, to be able to use for statistical testing. The script can be seen in Appendix B.6. Another script, Appendix B.7, was created by the candidate to calculate the median and the interquartile range of the doses for the different structures, in addition to preparing the data for statistical testing. This script also calculated the relative change and the difference between dosages.

3.6 Tools and Statistical Tests

Further analysis of the calculated metrics was done by the candidate using IBM SPSS Statistics (Version 29.0). Both creation of figures and the execution of statistical tests can be done using this program.

Measures of Statistical Distribution and Dispersion

When dealing with larger populations, the mean is often used to provide a summary of the distribution, along with the standard deviation or variance to indicate the spread. However, the current project is limited by the small sample size of only 15 patients and 20 structures. The data being compared are from the same patients and structures, but at different times or with different doses, resulting in a non-normal distribution of dependent pairs. In such cases, it is more appropriate to use the median as a summary of the distribution, as it does not require the assumption of normality. A statistical measure of the distribution's spread that complements the median is the interquartile range (IQR). IQR is the difference between the third quartile and the first quartile of a distribution, illustrated in Figure 3.7.

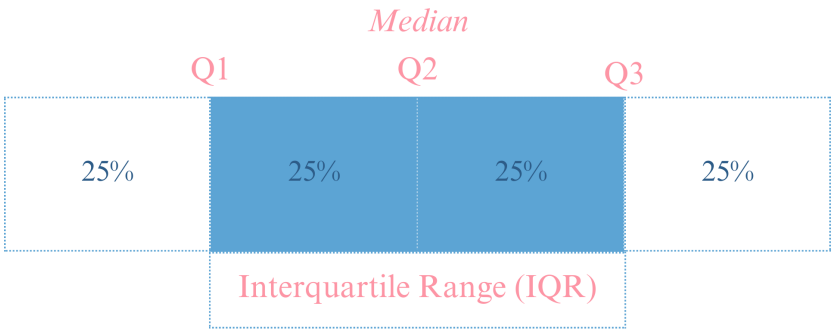

Figure 3.7: Illustration of interquartile range. Q stands for quartile, making Q1 the first quartile, Q2 the second (the median), and Q3 the third quartile.

Wilcoxon Signed-Rank Test

A non-parametric test possible to use on the data is Wilcoxon Signed-Rank Test. The null hypothesis of this test is that the median of differences between a pair equals zero. By testing this null hypothesis the candidate can find if there are statistical significant differences. The null hypothesis is rejected if the p-value is lower than the chosen α. The chosen α in this project was 0.05, which means that the the results are incorrect 5% of the time, but correct 95% of the time.

Chapter 4

Results

This chapter presents the findings of the project, covering various aspects. It includes the selection of substructures for contouring, examples of the contouring process, a comparison of both geometric and dosimetric aspects between photon and proton beam planning, and the use of figures and tables to visually depict the analyzed differences. The investigation explores potential correlations and highlights the specific parts of the heart that are affected. It is important to note that a portion of the statistical results are presented in the accompanying appendix rather than within this chapter.

4.1 Literature Search

Many various methods and substructures were discovered in the chosen publications as alternatives to mean heart dose (MHD) for modeling radiation to the heart. Two of the articles focused on the four heart chambers, the right atrium, the right ventricle, the left atrium, and the left ventricle. Niedzielski et al. examined the relationship between the dose to the four heart chambers and disease in the pericardium [35]. Cella et al. investigated the relationship between the dose to the four heart chambers and valvular disease [46]. Another study, by van Nimwegen et al., estimated both MHD and mean left ventricular doses, and found that the ratio for heart failure was higher with increased mean left ventricular doses [36]. Thor et al. investigated the dose to the pericardium as well as the ventricles and atria as isolated groupings of the heart chambers [32].

Other articles focused on the coronary artery disease and coronary arteries. Jacob et al. studied the four main coronary arteries, the left main coronary artery (LMCA), the left anterior descending coronary artery (LAD), the left circumflex (Cx), and the right coronary artery (RCA), in addition to the left ventricle [66]. Another study only studied the LAD, more specifically using the LAD V15 Gy dose to predict the risk of major

adverse cardiovascular events (MACE) [38].

Studying the heart's valves could be informative as well. The valves are easy to also include, as they are the connection between some of the earlier suggested substructures, the atria and ventricles, and ventricles and vessels of the heart, aorta and pulmonary artery. One of the previously discussed heart issue related to radiation, in section 2.6.2, is valvular disease. As was already indicated, Cella et al. studied the association between valvular disease and the dose to the four heart chambers, but for this research, it would be beneficial to additionally include the valves themselves at this stage [46]. A study by Duane et al. contoured the pulmonary valve, aortic valve, mitral valve, and tricuspid valve, in addition to the whole heart and the left ventricle [54]. Subsequently, the four heart valves, tricuspid, pulmonic, mitral, and aortic, were also added to the list of substructures to be contoured.

Another group is the great vessels of the heart. Since these are connected to the heart they could be interesting to include. They could also be helpful for the contouring as they are clearly seen, and connect to other substructures. Another study by Momin et al. looked at 15 substructures, including the heart chambers and valves, coronary arteries, the aorta, the pulmonary artery and superior vena cava [67]. Therefore aorta, pulmonary artery, and vena cava, superior (SVC) and inferior (IVC) were chosen to be contoured. Pulmonary veins were taken into consideration, but were left off because cardiac contouring atlases generally do not include them.

A rare effect of radiation is development of conduction abnormalities [68]. Studying significant components of the heart's electrical conduction system may therefore be relevant in this project. Qian et al. contoured the SAN, and found a possible correlation with sick sinus syndrome [50]. A study similar to this project chose to outline the whole heart, pericardium, AVN, and two walls in the heart [33]. This demonstrates that SAN and AVN may both be interesting and contourable. According to a recent study by McWillam et al., a region in the base of the heart was linked to a worse patient survival rate [27]. The sinoatiral node and the origin of the left coronary artery were both located in this region. McWilliam et al.'s earlier study also concluded that the base of the heart is sensitive to radiation dose [69].

Ultimately 19 substructures classified in six groups were chosen to be studied and contoured, with the possibility of removing some of them, if they could not be realistically found and drawn in the CT images. These chosen substructures can be seen in

Table 4.1: Selected substructures for contouring.

Group	Name	Structure ID	Abbreviation
Heart chambers	Right atrium	RightAtrium	RA
	Right ventricle	RightVentricle	RV
	Left atrium	LeftAtrium	LA
	Left ventricle	LeftVentricle	LV
Heart valves	Tricuspid valve	TricuspidalValve	
	Pulmonic valve	PulmonicValve	
	Mitral valve	MitralValve	
	Aortic valve	AorticValve	
Coronary arteries	Left main	LeftMainCoArtery	LMCA
	Left anterior descending	LeftAntDescArter	LAD
	Left circumflex	LeftCircumflex	Cx
	Right coronary artery	RightCoronarArte	RCA
Vessels of the heart	Aorta	Aorta	
	Pulmonary artery	PulmonaryArtery	
	Superior vena cava	SuperiorVenaCava	SVC
	Inferior vena cava	InferiorVenaCava	IVC
Cardiac conduction	Sinoatrial node	NodeSinus	SAN
node	Atrioventricular node	NodeAV	AVN
Other	Pericardium	Pericard	

Table 4.1. Not all chosen substructures have been found to correlate with radiation induced heart disease, but chose to include full groups of substructures at this step. By doing this later we have the option use statistics on whole groups, and compare them to each other as groups.

4.2 Contouring of Heart Structures

Following the method in section 3.3, 39 structure sets were drawn. 15 each for A.plan and A.w1, and 9 for C.plan. A slice from one of the patients can be seen in Figure 4.1, without any drawing, with drawing of structures, and drawing of the structures with the 3 mm pericardium. A 3D model of the substructures drawn can be seen in Figure 4.2.

Different strategies were used to evaluate the contoured substructures. A difference in the left atria were found and corrected by the candidate. The continuity of the coronary arteries was also verified in every scan.

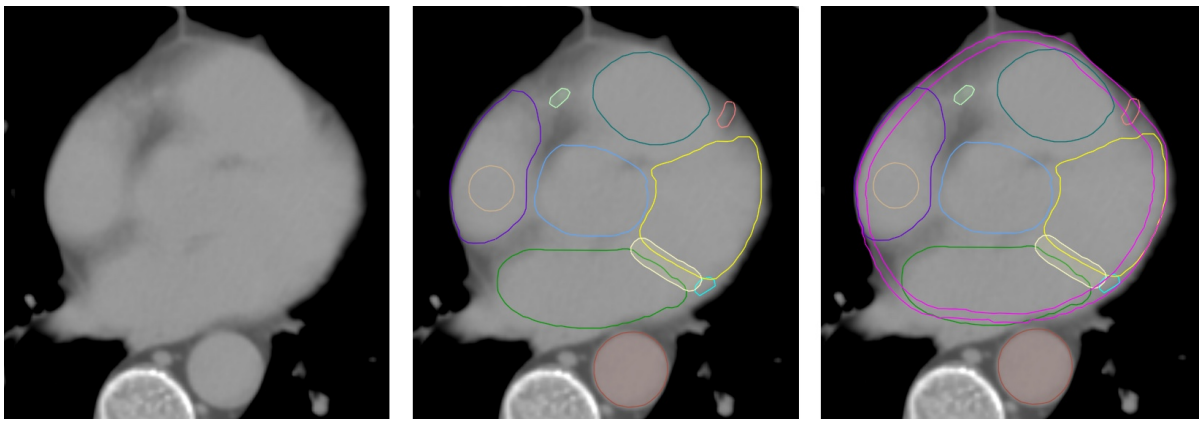

Figure 4.1: Slice contouring of the substructures in one patient. With and without the pericardium, in the transversal plane. The color labels can be found in Figure 3.2.

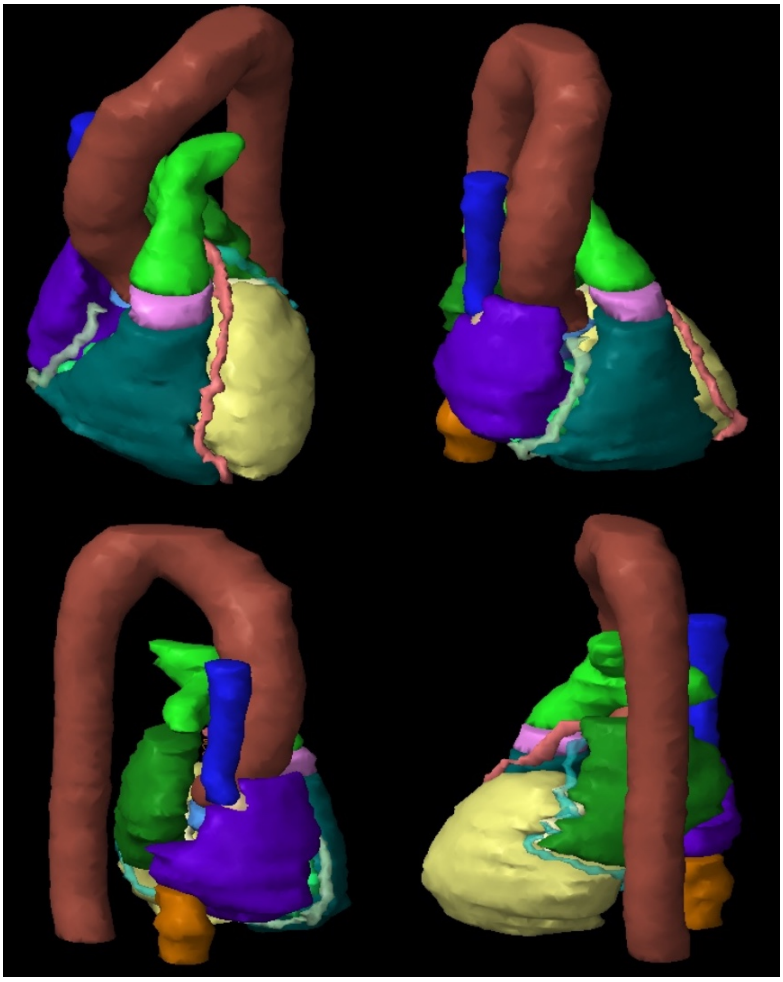

Figure 4.2: 3D model of the substructures in one patient, from four different angels. The color labels can be found in Figure 3.2.

4.3 Comparison of Contouring of Structures

4.3.1 Visual Comparison of the Structures

Structural differences between the substructures drawn with and without contrast seen by the eye could be interesting to find and later discuss. It has to be taken into consideration that the heart and lungs may not be in the same phase or place, and the structures can vary because of this. Overall, with minor differences, the structures seem to correspond adequately. The contrasted drawings were likely essential to the contouring learning process.

The biggest difference between C.plan and A.plan can be seen with the coronary arteries. The coronary arteries can easier be seen with the contrast liquid. The volumes of the coronary arteries structures drawn are noticeably larger in the contrast images, as they are more often seen with certainty than guessed. As they are drawn quite small, a small movement in the heart makes a big impact. However, when comparing the substructures drawn with and without contrast, they are for most of the time seen in the same area, but not the exact same location. The left main coronary artery seem to have the most placemental variation among the coronary arteries. Without contrast, this is extremely difficult to perceive, hence variations are frequently found in the drawings.

Another difference found is the separation of the heart chambers. Especially the right atrium varies, and it's borders with the right ventricle and the left atrium. The difference in border with the right ventricle also impacts the tricuspid valve. The borders are harder to see with the AVE-4D-CT, as it smudges out the edges.

There are also a few minor variations. The identification of the left ventricle, which affects both the pulmonic valve and the pulmonary artery, varies a bit. It is usually defined higher with the contrast images, as it is easier to identify, which makes the pulmonic valve and pulmonary artery appear higher up in the thorax. The nodes also vary slightly as well.

4.3.2 Geometric Comparison of Substructures

Multiple statistical tools were used to compare different measures of the structures drawn C.plan, A.plan and A.w1. Both the volumes (V) [cc], the overlap of the structures with Dice coefficient (D), and the Hausdorff distance 95% percentile (H) [mm] were examined.

Volume

The structures in this project varied in volume, as shown in Figure 4.3. The structures were split into two categories: large or small, based on whether the structure has median volume over 10 cc. This placed the heart, all heart chambers, vessels of the heart and the pericardium in the "large" group, and the heart valves, the nodes and the coronary arteries in the "small" group. The structures also varied in volume on the different scans, as one can see in Figure 4.4. To find out if there was change of statistical significance a Wilcoxon signed-rank test was performed. This compared V.A.plan with V.C.plan and V.A.w1 separately as two pairs, with results in Table 4.2. The source and full results of this test can be seen in Appendix C.1.

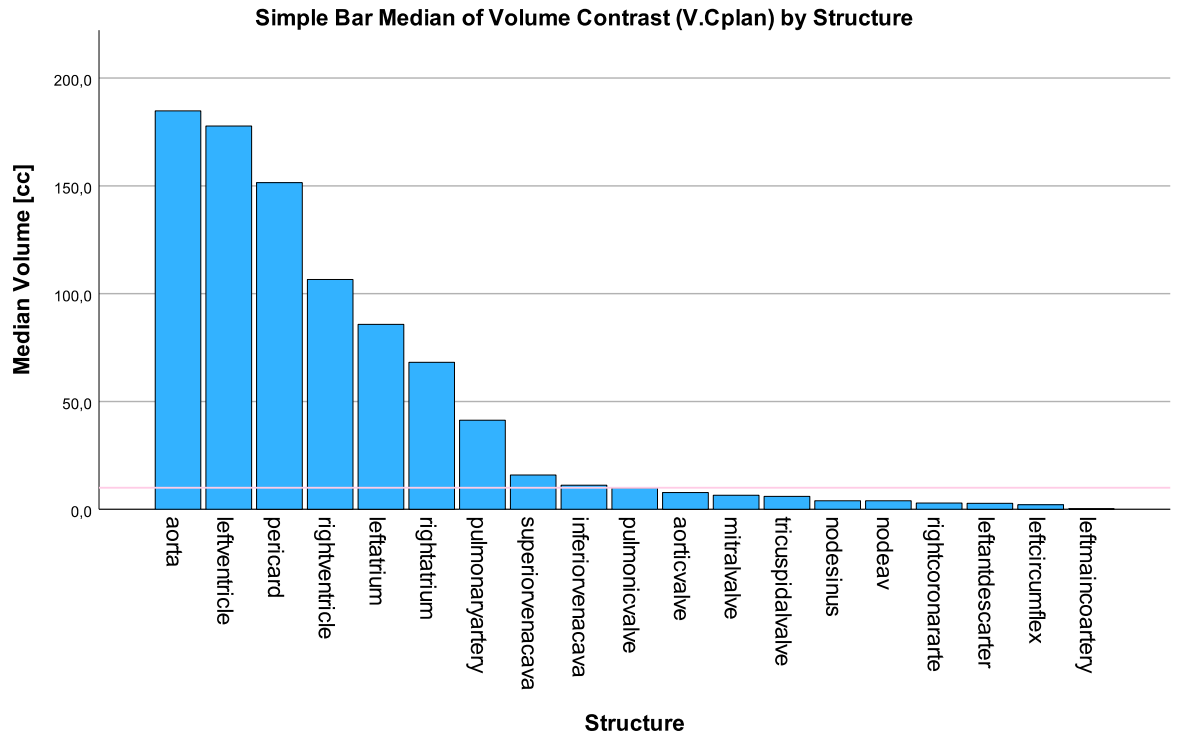

Figure 4.3: Bar plot with the different median volumes (V.C.plan) [cc] of each substructure (excluding the heart). The pink line represents 10 cc. Sorted by volume (V.C.plan).

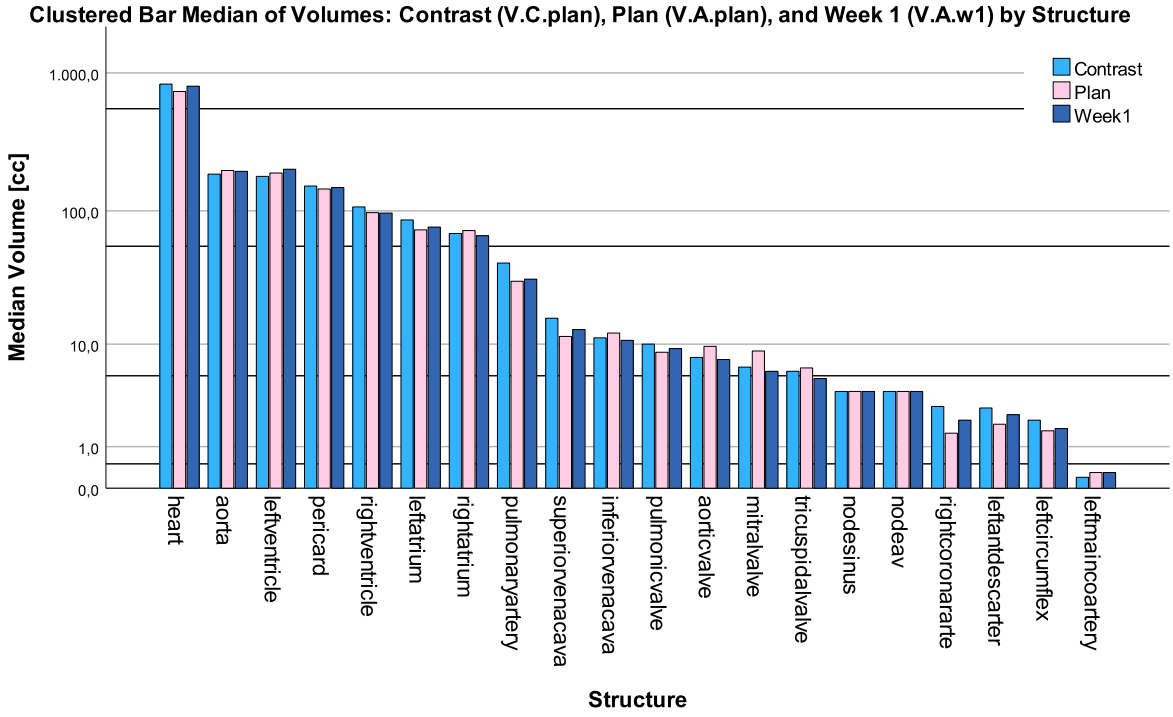

Figure 4.4: Bar plot with the different median volumes (V) [cc] (V.C.plan, V.A.plan, V.A.w1) of each structure. Sorted by volume (V.C.plan).

Table 4.2: Median volume for each structure, with interquartile range (IQR), sorted by V.C.plan. Where the null hypothesis of the Wilcoxon signed-rank test were rejected are marked as bold ($\alpha = 0.05$).

	Median Volume [cc]		
Structure ID	**V.C.plan (IQR)**	**V.A.plan (IQR)**	**V.A.w1 (IQR)**
Heart	**828.5 (759.8-896.6)**	692.3 (605.25-808.1)	721.8 (622.9-839.3)
Aorta	184.8 (175.4-203.1)	182.9 (167.65-215.25)	177.4 (158.6-201.8)
LeftVentricle	177.8 (158.0-220.2)	181.2 (168.0-212.2)	177.9 (157.7-206.6)
Pericard	**151.5 (138.4-164.6)**	124.9 (116.4-149.9)	139.9 (121.8-153.0)
RightVentricle	**106.6 (97.8-135.1)**	90.4 (76.5-98.2)	92.5 (80.9-108.7)
LeftAtrium	**85.8 (72.8-99.3)**	66.1 (55.5-84.5)	74.3 (60.7-82.3)
RightAtrium	68.2 (58.7-71.9)	60.7 (54.5-77.5)	61.6 (54.0-74.5)
PulmonaryArtery	**41.3 (34.6-53.7)**	30.3 (25.3-35.6)	31.4 (24.8-35.1)
SuperiorVenaCava	15.9 (12.2-19.9)	10.8 (8.6-13.2)	10.7 (8.5-13.75)
InferiorVenaCava	11.2 (9.9-11.6)	10.9 (8.3-13.4)	10.0 (8.6-10.8)
PulmonicValve	10.0 (8.1-10.4)	7.3 (6.9-9.0)	7.7 (6.7-9.4)
AorticValve	**7.8 (6.8-8.5)**	8.3 (7.0-10.0)	**7.6 (6.9-8.4)**
MitralValve	**6.5 (6.2-6.8)**	6.3 (5.2-8.9)	5.6 (5.1-7.2)
TricuspidalValve	6.0 (5.7-7.7)	6.4 (6.0-7.9)	5.2 (5.1-7.1)
NodeSinus	4.0 (4.0-4.0)	4.0 (4.0-4.0)	4.0 (4.0-4.0)
NodeAV	4.0 (4.0-4.0)	4.0 (4.0-4.0)	4.0 (4.0-4.0)
RightCoronarArte	**2.9 (2.4-3.1)**	1.7 (1.5-2.0)	1.5 (1.4-2.2)
LeftAntDescArter	**2.8 (2.5-3.3)**	2.1 (1.8-2.6)	2.4 (2.0-2.6)
LeftCircumflex	**2.1 (1.9-3.2)**	1.7 (1.5-1.9)	1.6 (1.4-1.8)
LeftMainCoArtery	0.2 (0.2-0.3)	0.2 (0.2-0.3)	0.2 (0.2-0.3)

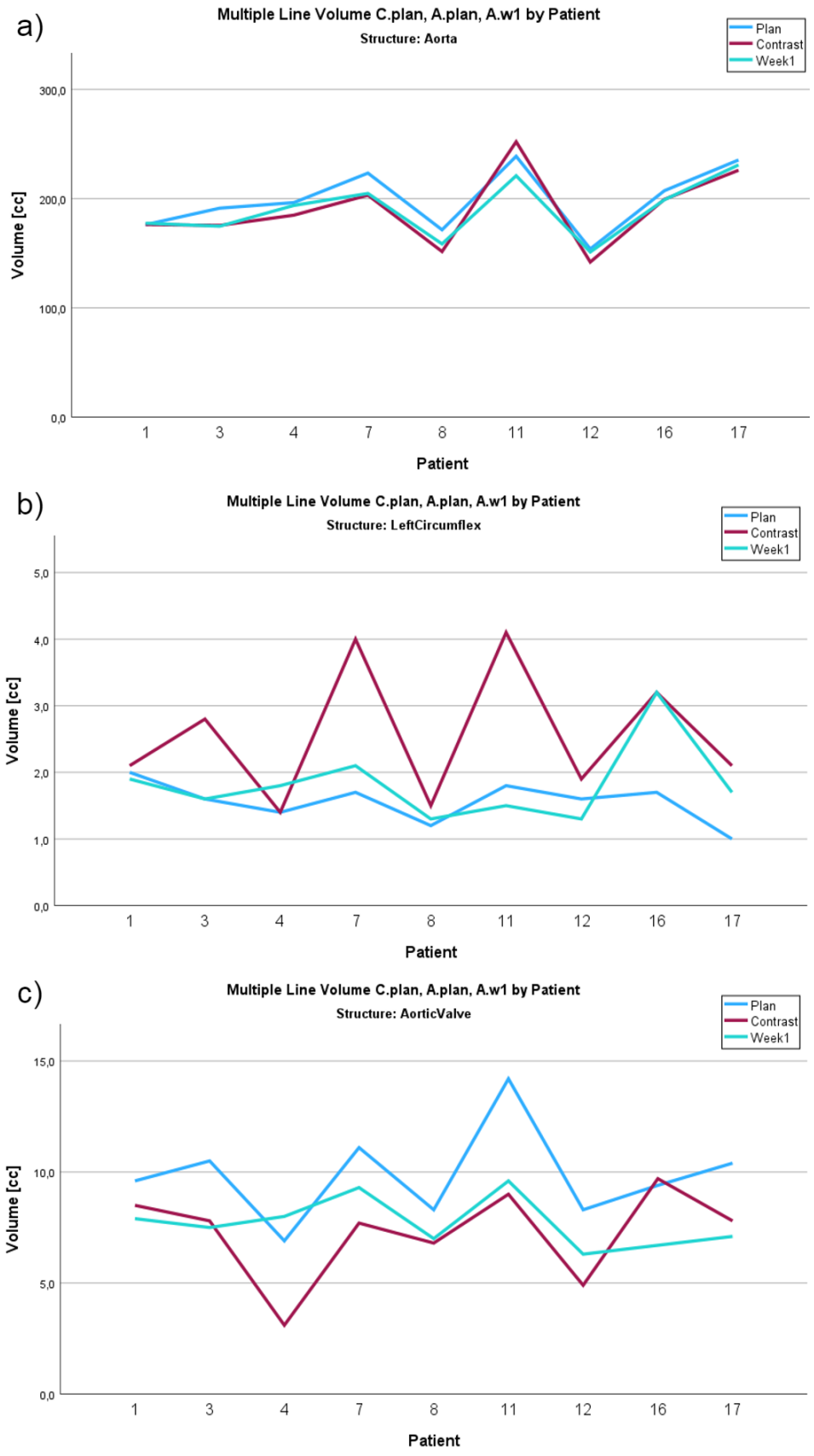

Figure 4.5: Multiple line plots of the median volume for each patient, for three substructures: a) the aorta, b) the left circumflex coronary artery, and c) the aortic valve.

Dice Coefficient

The script in Appendix B.2 generated visual representations of the areas in each slice for each structure, in addition to calculations. Figure 4.6 shows a slice where A.plan and A.w1 does not overlap completely, and is an example of the output and calculations of this script. It can be observed that D.C.Plan and D.A.w1 fall within a similar range for most of the structures listed in the Table 4.3.

A Wilcoxon signed-rank test was performed, pairing the Dice coefficients of C.plan and A.w1. The entire set of results from the test can be seen in Appendix C.2. Only two of the structures had p-values below $\alpha = 0.05$: pericardium (p = 0.038) and leftMainCoArtery (p = 0.043). Therefore, those were the only two structures where the null hypothesis was rejected. The tricuspid valve also is noticeably different in Table 4.3, even though it was not rejected in the test (p = 0.051).

Figure 4.7 describes the variety among the structures, and show that they have very different D values and ranges of uncertainty. Some of the structures also have clear outliers. With the exception of the pericardium, all of the structures with D median under 0.5 are in the small group. Some small structures perform better, the aortic and pulmonic valve, with D above 0.8. The large group all have D median above 0.7, except for the pericardium, that lies around 0.4.

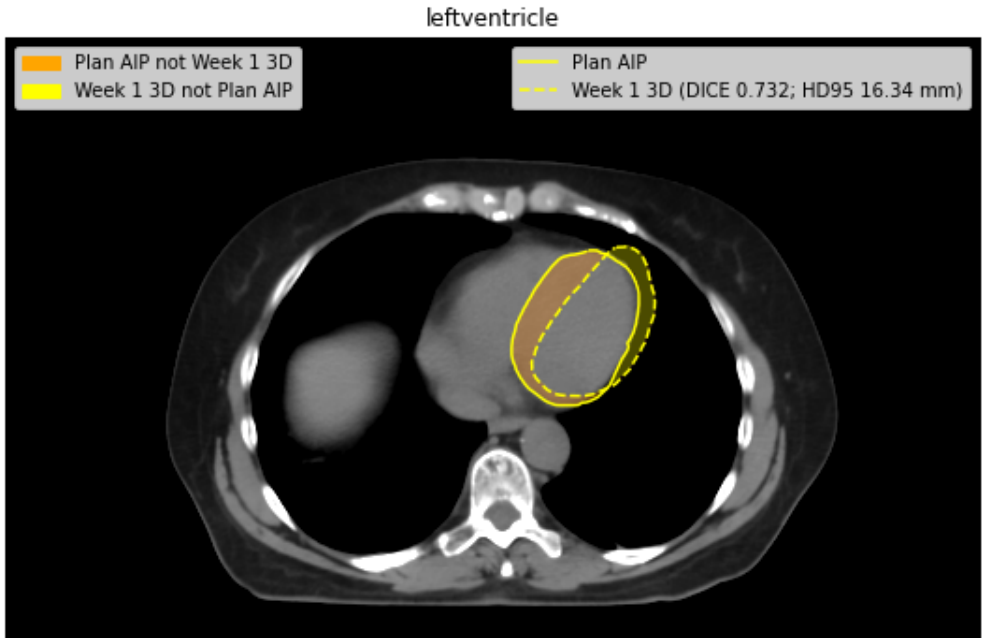

Figure 4.6: Left ventricle comparison of patient 12, Week 1 (3D transfer), slice 29. Credit [1].

[1] Image from patient group, added drawings by program created by Helge Egil Seime Pettersen.

Table 4.3: Median of Dice coefficient (D) for all patients on each structure, with interquartile range (IQR), sorted by volume. The values where the null hypothesis of the Wilcoxon signed-rank test were rejected are marked as bold ($\alpha = 0.05$).

	Median Dice coefficient			
Structure ID	**D.C.plan (IQR)**		**D.A.w1 (IQR)**	
Heart	0.92	(0.9-0.94)	0.90	(0.86-0.93)
Aorta	0.88	(0.86-0.89)	0.89	(0.87-0.91)
LeftVentricle	0.76	(0.75-0.81)	0.81	(0.72-0.83)
Pericard	**0.45**	**(0.40-0.54)**	**0.39**	**(0.30-0.41)**
RightVentricle	0.76	(0.74-0.77)	0.78	(0.72-0.80)
LeftAtrium	0.80	(0.79-0.83)	0.79	(0.76-0.81)
RightAtrium	0.72	(0.67-0.74)	0.75	(0.67-0.80)
PulmonaryArtery	0.75	(0.69-0.79)	0.74	(0.69-0.80)
SuperiorVenaCava	0.75	(0.72-0.77)	0.73	(0.69-0.78)
InferiorVenaCava	0.75	(0.74-0.82)	0.77	(0.70-0.82)
PulmonicValve	0.86	(0.78-0.89)	0.84	(0.75-0.86)
AorticValve	0.81	(0.76-0.83)	0.82	(0.76-0.85)
MitralValve	0.45	(0.36-0.49)	0.43	(0.32-0.50)
TricuspidalValve	0.15	(0.02-0.35)	0.45	(0.31-0.50)
NodeSinus	0.59	(0.52-0.68)	0.67	(0.48-0.72)
NodeAV	0.38	(0.28-0.42)	0.35	(0.21-0.63)
RightCoronarArte	0.12	(0.09-0.19)	0.17	(0.15-0.23)
LeftAntDescArter	0.20	(0.06-0.21)	0.12	(0.03-0.20)
LeftCircumflex	0.11	(0.08-0.19)	0.11	(0.08-0.17)
LeftMainCoArtery	**0.14**	**(0.00-0.19)**	**0.21**	**(0.09-0.37)**

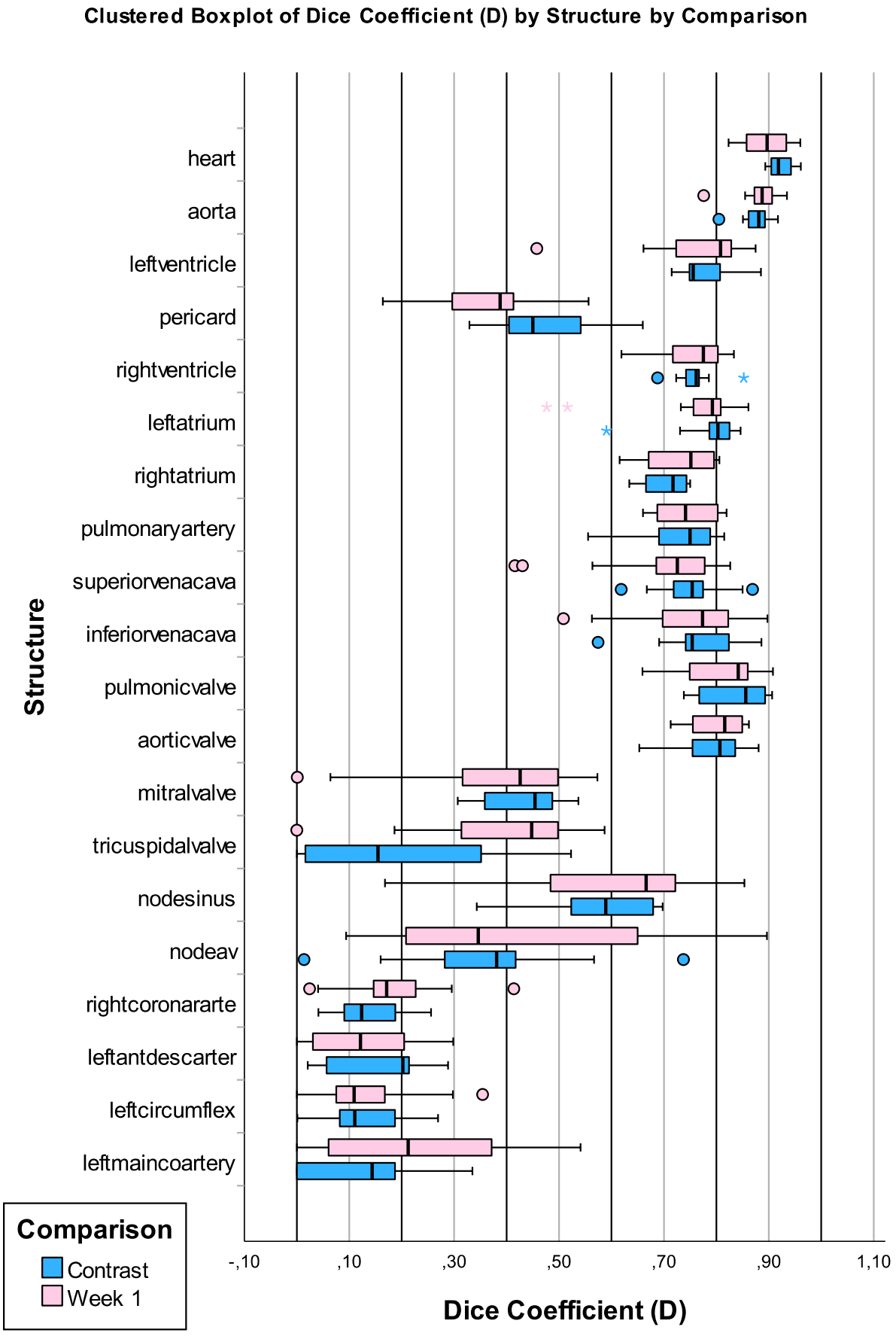

Figure 4.7: Clustered boxplot of Dice coefficient of contrast planning (C.plan) and week 1 (A.w1) CT, sorted by volume.

Hausdorff distance 95% percentile

Hausdorff distance 95% percentile (H) [mm] values were also generated with the script in Appendix B.2, comparing A.plan with both C.plan and A.w1 separately. When comparing H.C.plan and H.A.w1 of the specific structures in Table 4.4 one can see that they seem to generally be in the same range, but often a higher median for C.plan. With Figure 4.9 one can observe that the structures generally had values below 15 mm, but with some clear outliers and uncertainty. Here both small and large structures experienced both low H and high H. To find if there was a statistical difference between the distances found with C.plan and A.w1 they were paired in a Wilcoxon signed-rank test ($\alpha = 0.05$). The statistical results can be seen in Appendix C.3, where it was confirmed that no structure's H value varied among scans.

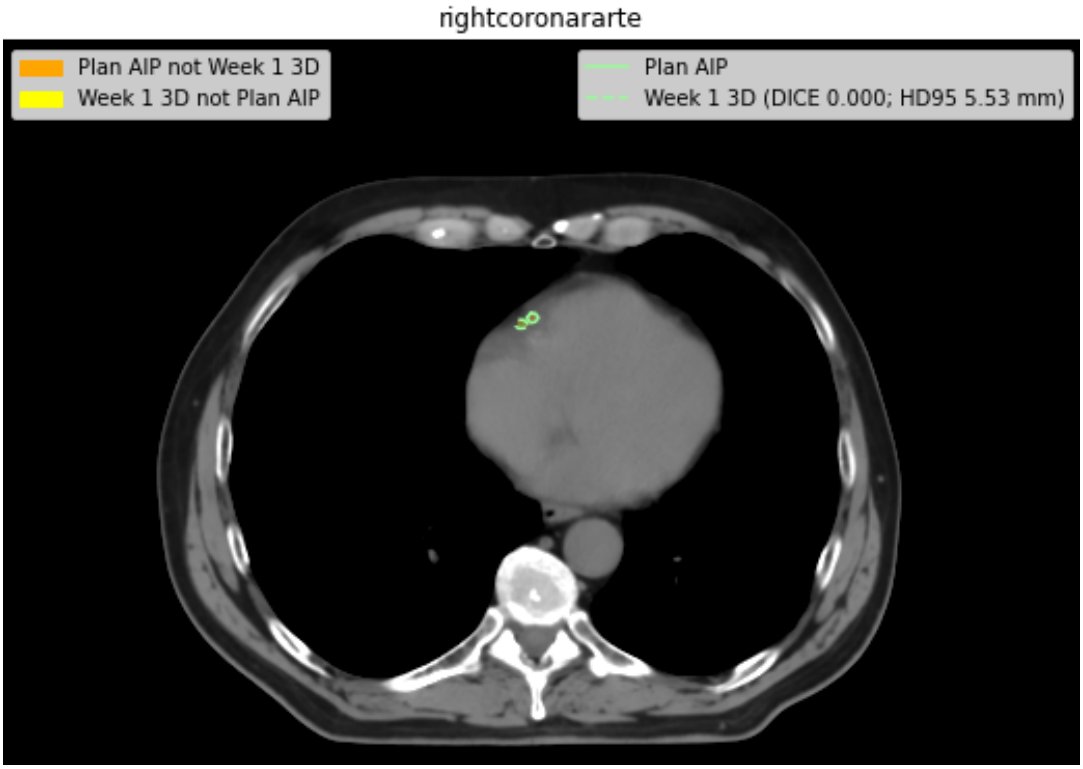

Figure 4.8: Right coronary artery comparison, patient 17, Week 1 (3D transfer), slice 22. Credit [2].

[2]Image from patient group, added drawings by program created by Helge Egil Seime Pettersen.

Table 4.4: Median of Hausdorff distance 95% percentile (H) for all patients on each structure, with interquartile range (IQR).

	Median Hausdorff Distance 95 Percentile [mm]			
Structure ID	**H.C.plan (IQR)**		**H.A.w1 (IQR)**	
Heart	7.12	(6.35-8.4)	8.94	(7.56-13.3)
Aorta	5.92	(4.26-6.36)	4.7	(3.77-5.68)
LeftVentricle	12.61	(12.3-13.95)	10.21	(8.32-14.18)
Pericard	7.06	(5.73-7.71)	8.71	(6.34-12.31)
RightVentricle	11.31	(10.54-13.58)	10.03	(9.29-12.92)
LeftAtrium	8.86	(7.58-9.01)	7.93	(7.24-9.55)
RightAtrium	10.71	(9.82-12.89)	8.07	(7.57-11.66)
PulmonaryArtery	12.68	(9.77-18.71)	9.22	(8.13-14.63)
SuperiorVenaCava	4.04	(3.34-4.21)	4.08	(3.34-4.74)
InferiorVenaCava	4.9	(4.18-6.6)	4.65	(3.97-5.89)
PulmonicValve	5.19	(3.75-6.82)	4.72	(3.95-7.3)
AorticValve	6.54	(5.64-8.48)	5.42	(4.64-6.85)
MitralValve	10.02	(8.53-12.1)	8.2	(7.22-10.62)
TricuspidalValve	11.79	(10.6-16.38)	8.19	(6.54-10.62)
NodeSinus	6.12	(4.32-7.07)	3.72	(3.31-7.87)
NodeAV	8.42	(6.89-10.93)	8.93	(5.26-11.53)
RightCoronarArte	11.36	(10.24-13.28)	8.17	(7.59-11.03)
LeftAntDescArter	8.69	(7.86-10.45)	8.56	(6.63-14.18)
LeftCircumflex	11.52	(9.53-13.33)	8.13	(7.74-10.98)
LeftMainCoArtery	8.23	(7.98-10.04)	6.93	(4.52-11.96)

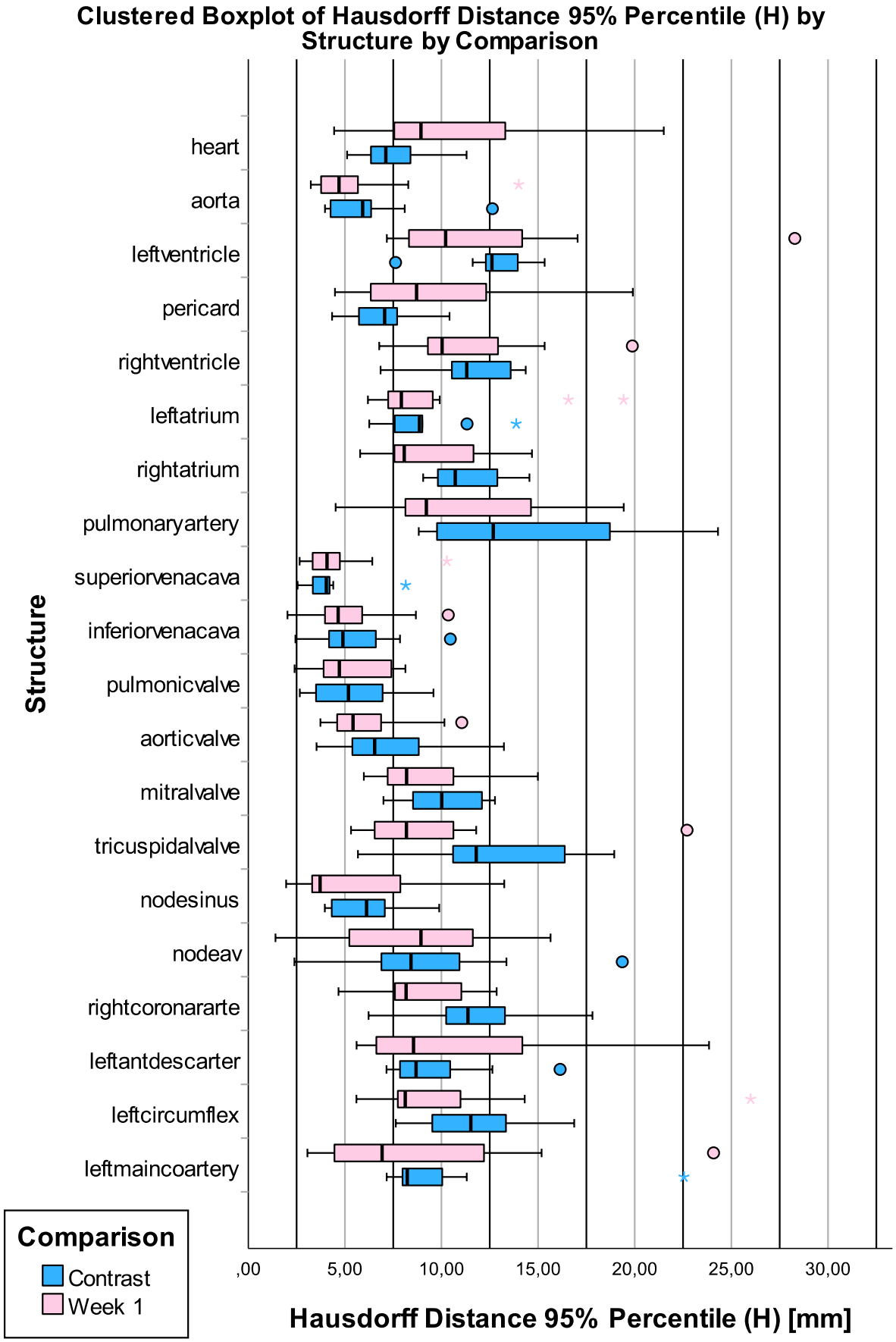

Figure 4.9: Clustered boxplot of Hausdorff distance 95% percentile for contrast planning (C.plan) and week 1 (A.w1) CT, sorted by volume of the structures.

Correlations

To study possible correlations between D/H and V scatter plots were used. Observe in Figure 4.10 that the large substructures generally had high D values, although some lower outliers and the pericardium were exceptions. The small substructures exhibited more variability, the coronary arteries had typically low D values, while the nodes varied considerably between patients. The valves, which had similar volumes, also demonstrated variability in D values, with the semilunar valves tending to have higher D values than the AV valves. The lack of correlation between H and V is illustrated in Figure 4.11. Volumes of all sizes can be seen to range in H value.

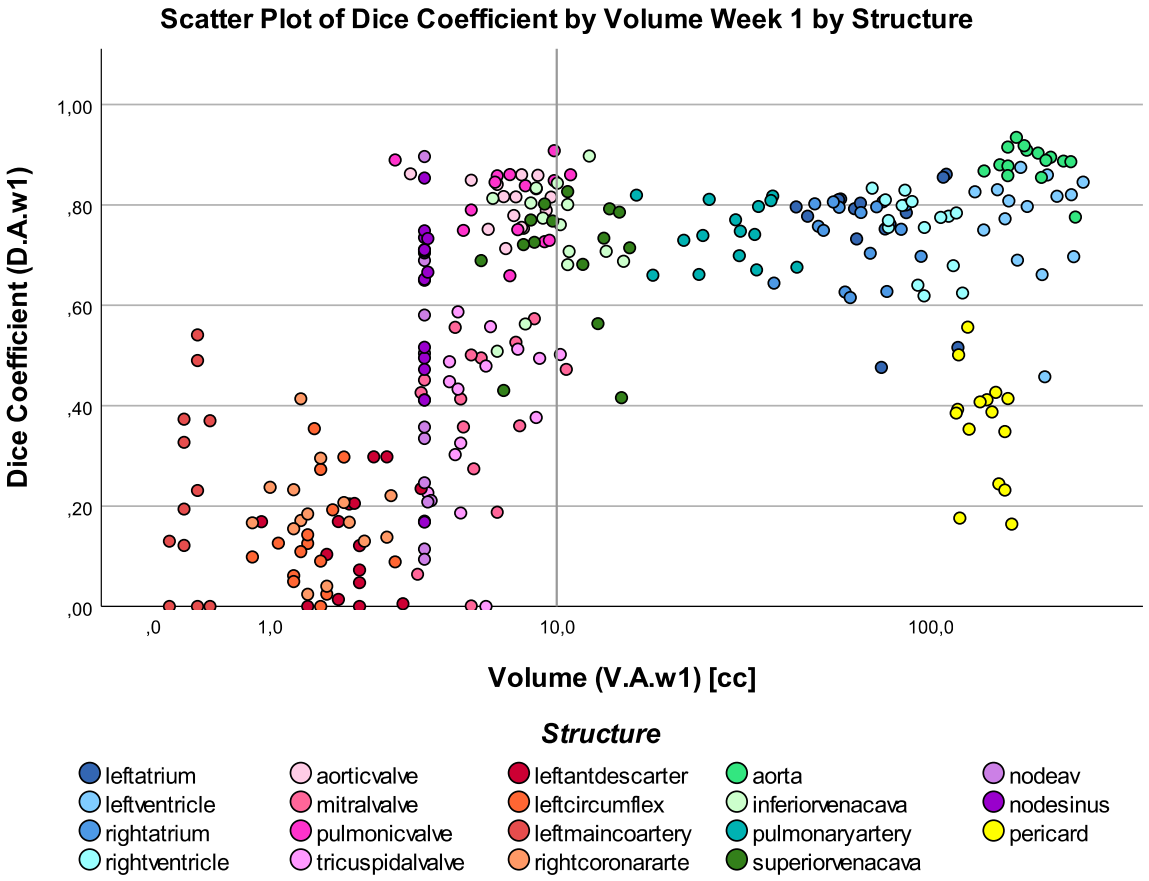

Figure 4.10: Scatter plot comparing volume (V) with Dice coefficient (D) in week 1 (VAw1-DAw1) for each substructure. The different groups are categorized by colors.

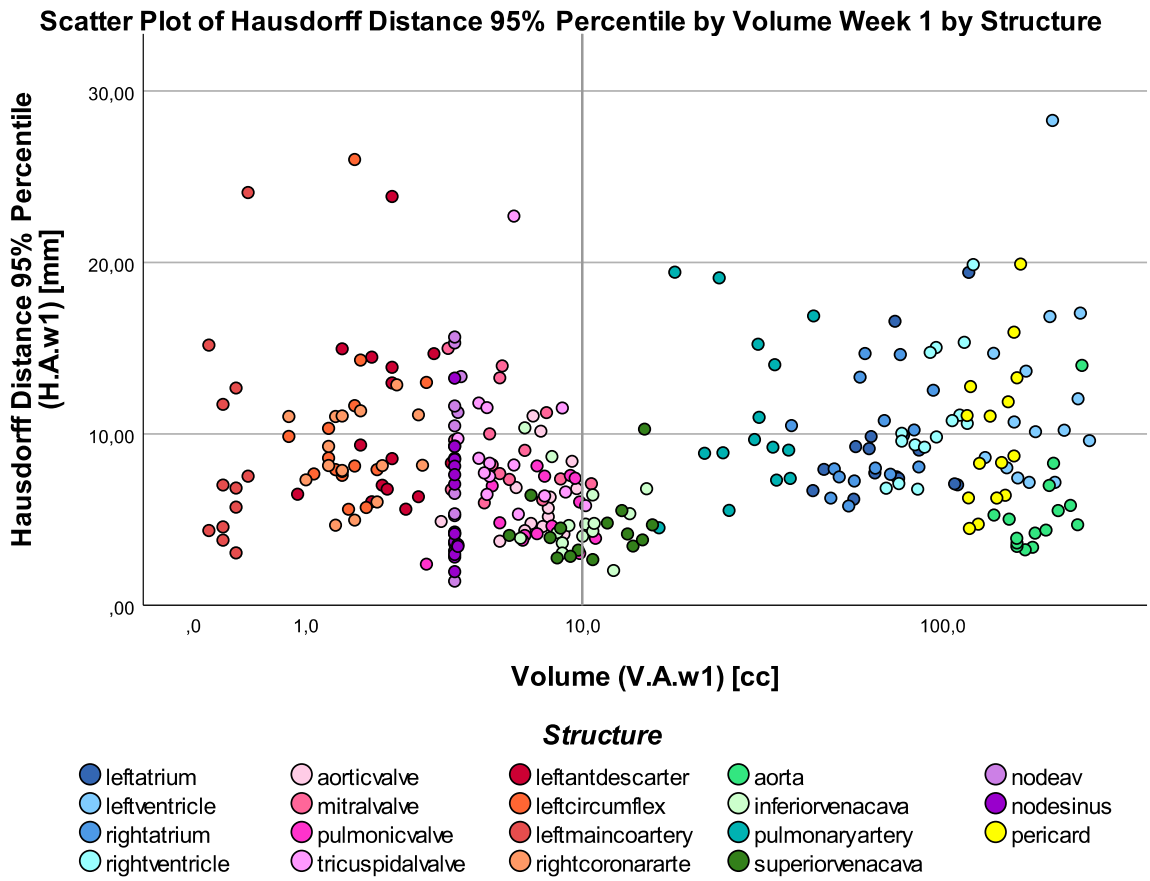

Figure 4.11: Scatter plot comparing volume (V) with Hausdorff distance 95% percentile (H) in week 1 (VAw1-HAw1) for each substructure. The different groups are categorized by colors.

4.4 Dose

4.4.1 Robustness of Planning

Continued Literature Search

The result of this expanded literature search by the candidate can be seen in Table 4.5. The studies listed in Table 4.5 were retrospective and used various substructures in their models to identify correlations, predict outcomes, or identify risk factors for specific endpoints. However, none of these studies had incorporated a dose constraint for the substructures. None of the studies used contrast CT scans. The statistics demonstrated that D45%, V15 and V30, along with Dmean and Dmax, can be effective dosage metrics for investigating the substructures.

Table 4.5: Summary of results from expanded literature search. *N.: number of patients in the study.

Reference	**Year**	**Cancer**	***N.**	**End point**	**Recommendation**
Wei *et al.*[43]	2008	Oesophagus	101	Pericardial effusion	rV30: Pericardium
Wang *et al.*[70]	2017	NSCLC	112	Cardiac events[1]	V30: right atrium, left atrium, left ventricle
Jacob *et al.*[66]	2019	Breast	120	Dosimetric study MHD[2]	Dmean: LAD, RCA
Thor *et al.*[32]	2020	NSCLC	437	Overall survival	D45%: Atria
Niedzielski *et al.*[35]	2020	NSCLC	141	Pericardial effusion	Dmean: left atrium
McWilliam *et al.*[71]	2020	NSCLC	1161	Overall survival	Dmax: RA, RCA, aorta[3]
Tjong *et al.*[38]	2022	LA-NSCLC	701	MACE[4]	V15: LAD
Wang *et al.*[39]	2022	Oesophagus	355	MCE[5] and overall survival	V30: LAD. Dmean: LMCA

[1]Symptomatic cardiac events, including: pericardial, ischemic, and arrhythmic.

[2]See if Mean Heart Dose (MHD) is a valid dose surrogate for LV and coronary arteries.

[3]Ascending aorta, the first section of the aorta, from the left ventricle and aortic valve.

[4]Major Adverse Cardiac Events: defined as "unstable angina (UA), Congestive heart failure(CHF) hospitalization or urgent visit, myocardial infarction (MI), coronary revascularization, and/or cardiac death." [38].

[5]Major Coronary Events: defined as: "diagnosis of myocardial infarction (International Classification of Diseases, 10th Revision, codes 121 to 124), coronary revascularization, or death resulting from ischemic heart disease (codes 120 to 125)." [39].

Dose Comparison over Time for Photon Beam

To analyse the robustness of the treatment dose over time, A.plan and A.w1 was compared. A Wilcoxon signed-rank test was performed, using the different found dose metrics, with the dose in A.plan and A.w1 paired. The structures that showed statistical difference over time can be seen in Table 4.6. The entire set of median dose values for all the metrics can be seen in Appendix C.4, also including the calculated values of the test. Figure 4.12 shows the variation in Dmean for each structure for both A.plan and A.w1. Figure 4.13 illustrates the anatomical placement of these rejected structures, while Figure 4.14 illustrates the DVH curves of the same structures, both for A.plan and A.w1, illustrating a higher dose in A.w1 than A.plan.

Table 4.6: The median dose values for each structure in photon beam planning of A.plan that rejected the null hypothesis of the Wilcoxon signed-rank test ($\alpha = 0.05$).

	Median A.plan (IQR)		**Median A.w1 (IQR)**	
Structure ID		**Dmean [Gy]**		
MitralValve	4.9	(2.75-15.2)	6.1	(3.1-18.8)
NodeAV	3.7	(2.1-7.75)	4.6	(2.4-10.6)
RightAtrium	5.1	(3.1-9.95)	5.8	(3.2-13.75)
		Dmax [Gy]		
NodeAV	6.0	(2.75-15.9)	7.6	(3.2-20.6)
		V15Gy [%]		
LeftAtrium	32.74	(20.57-48.28)	36.05	(27.11-47.9)
MitralValve	0.0	(0.0-20.71)	0.0	(0.0-38.48)
RightAtrium	0.78	(0.0-7.59)	0.73	(0.0-14.99)
		D45% [Gy]		
LeftAntDescArter	2.82	(1.71-8.58)	3.41	(2.75-12.97)
MitralValve	2.74	(1.74-9.09)	3.13	(1.93-11.81)
NodeAV	2.22	(1.38-4.91)	2.83	(1.62-6.73)

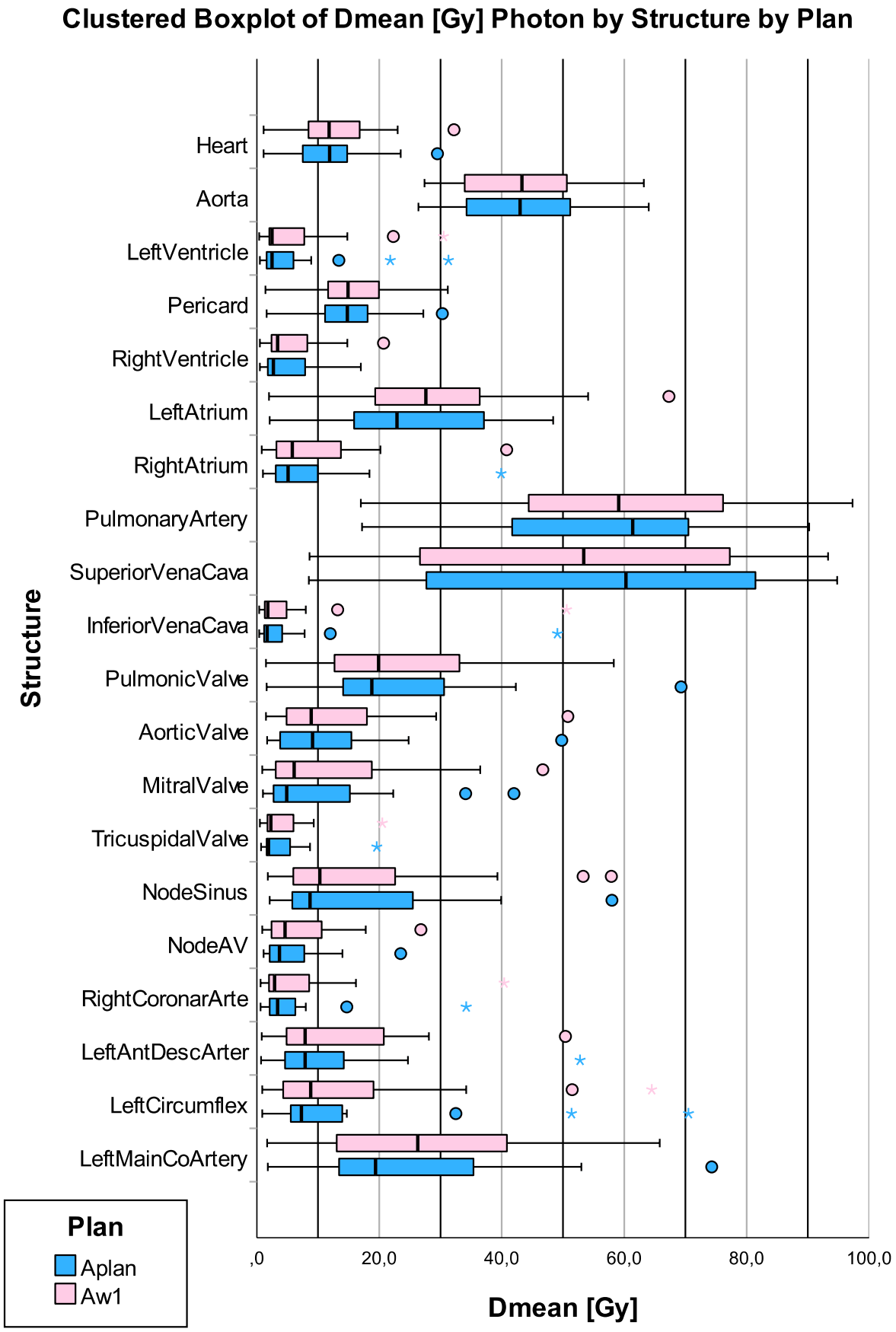

Figure 4.12: Clustered boxplot of Dmean for photon beam A.plan and A.w1, sorted by volume.

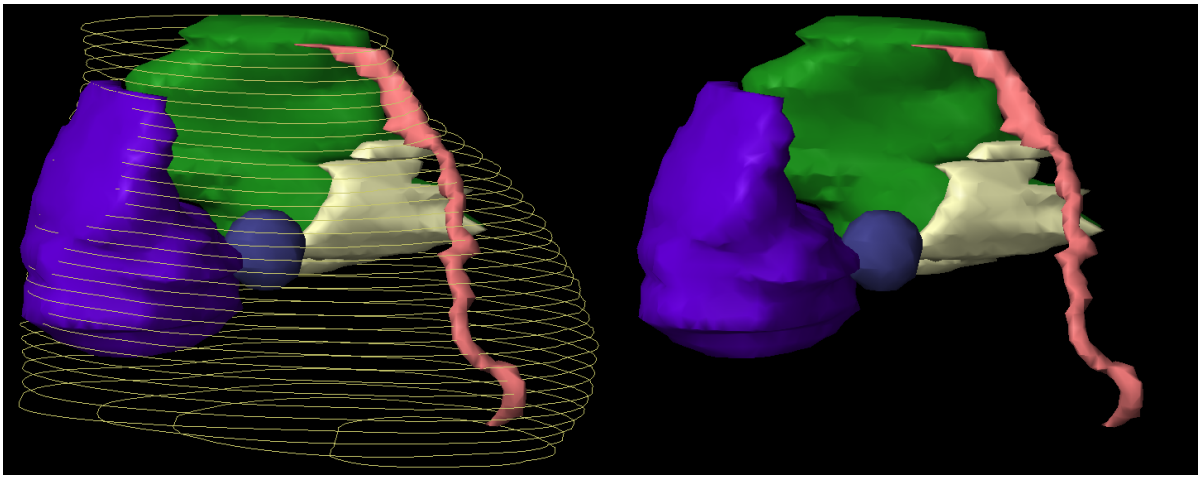

Figure 4.13: Illustration of the structures that showed statistical significant difference between A.plan and A.w1 for photon beam, frontal view, with and without the heart as contour.

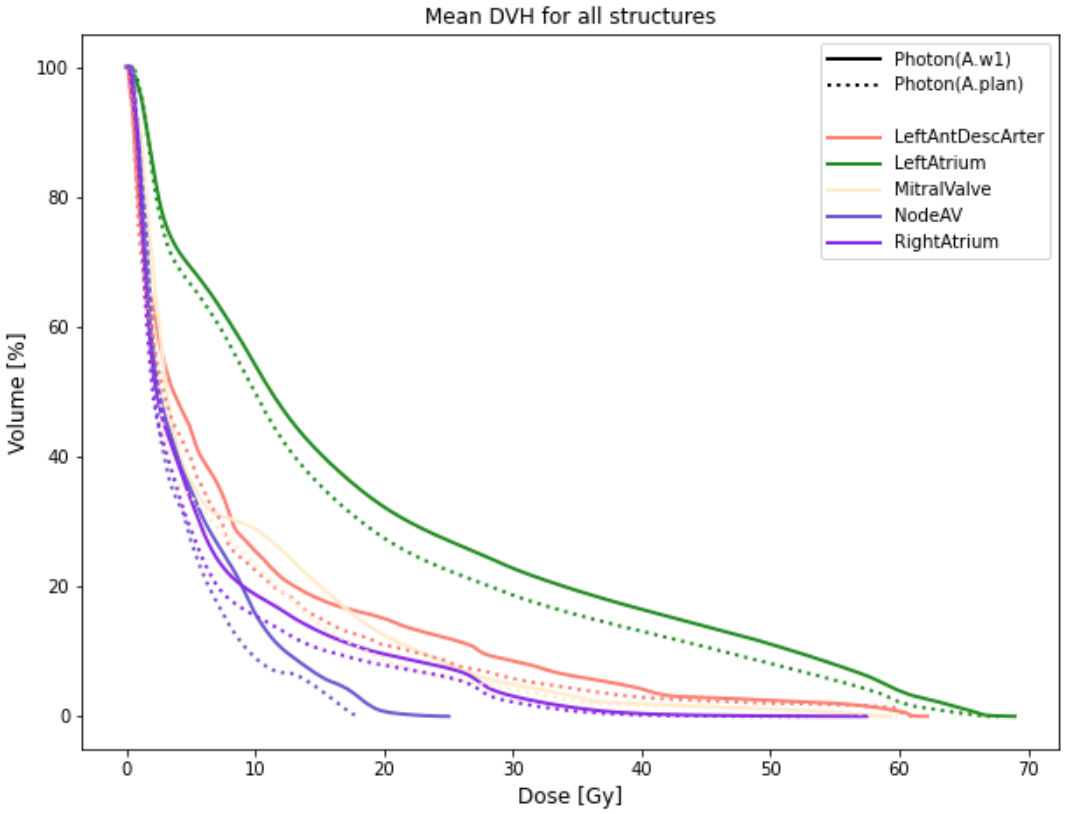

Figure 4.14: Mean DVH for the structures that showed statistical significant difference between A.plan and A.w1 for photon beam.

Dose Comparison over Time for Proton Beam

The same analysis of robustness of planning was done for proton beam, comparing A.plan and A.w1. A Wilcoxon signed-rank test was performed with the dose metrics to find the structures that showed statistical significant difference over time. The only structure that showed this difference was the superior vena cava, as showed in Table

4.7. All of the statistical measurements and descriptive statistics are in Appendix C.5. Figure 4.15 shows the DVH curve for the superior vena cava in both A.plan and A.w1, illustrating a lower dose in A.w1. It can seen in Figure 4.16 that for many of the structures the dose is low, with the median about the same for both occurrences, but contain many outliers. Some of the structures receives higher doses, but the structures mostly stay in the same range for both plans.

Table 4.7: Median and interquartile range (IQR) values of dose to rejected structure. The Wilcoxon signed-rank test for robustness of proton beam ($\alpha = 0.05$), the superior vena cava, comparing A.plan and A.w1, and showing statistical significant difference.

	Median A.plan (IQR)		**Median A.w1 (IQR)**	
Dose metric	**Superior Vena Cava**			
Dmean [Gy]	27.81	(1.64-50.55)	19.44	(0.44-41.64)
D0% [Gy]	61.79	(33.08-66.84)	61.56	(7.70-66.47)
D45% [Gy]	46.90	(0.37-56.19)	28.57	(0.31-53.46)
V15Gy [%]	67.70	(2.86-91.12)	62.30	(0.00-88.10)
V30Gy [%]	56.66	(0.04-75.74)	42.90	(0.00-73.00)

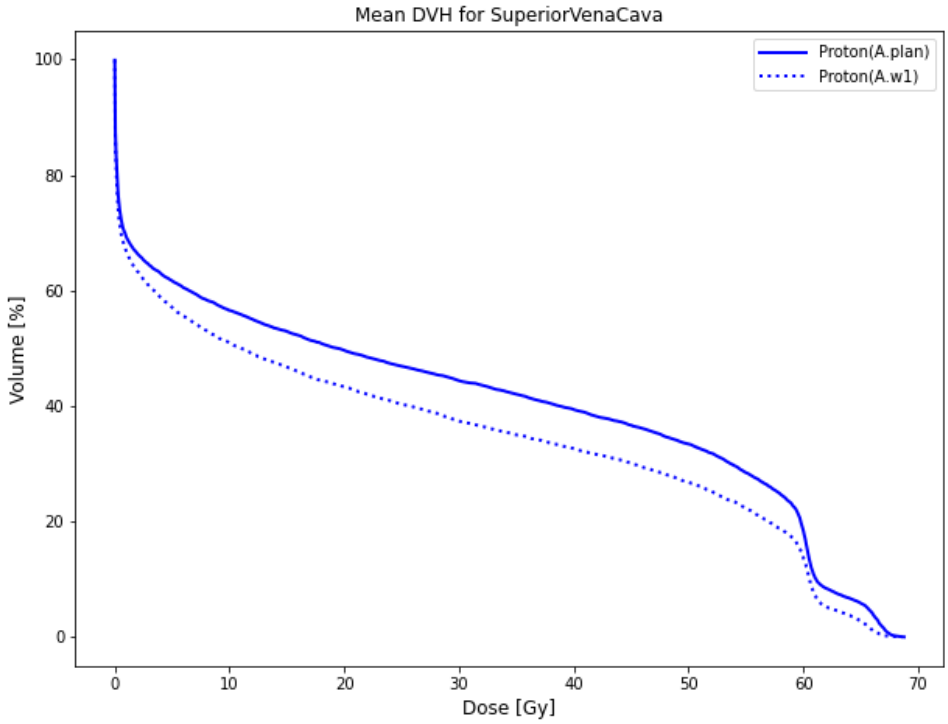

Figure 4.15: Mean DVH for superior vena cava for proton beam, the structure that showed statistical significant difference between A.plan and A.w1.

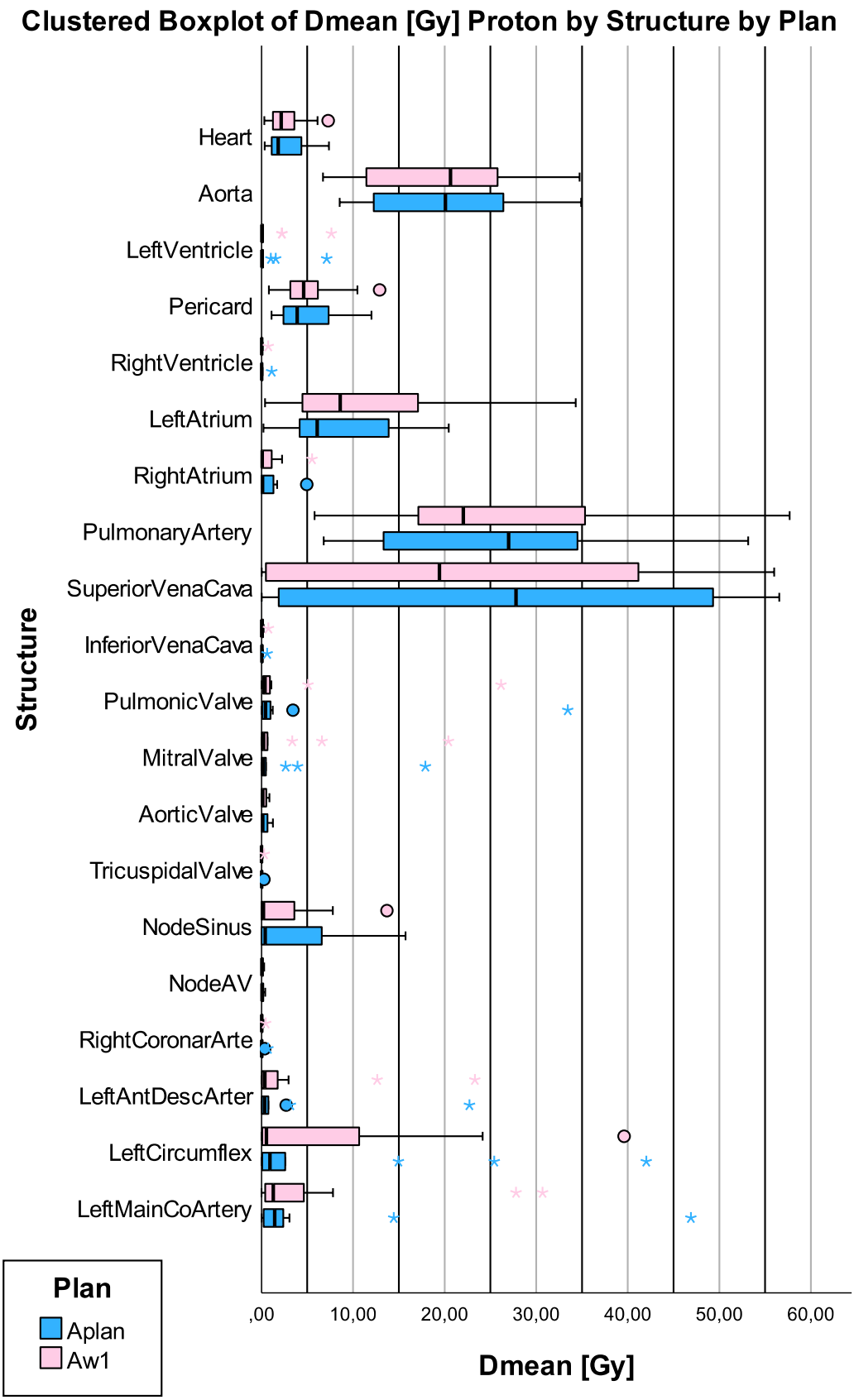

Figure 4.16: Clustered boxplot of Dmean for proton beam A.plan and A.w1, sorted by volume.

4.4.2 Photon Planning VS Proton Planning

Figure 4.17 illustrates that proton beam planning can reduce the dose to the structures. A Wilcoxon signed-rank test was performed to test this statistically for the different metrics. For Dmean and D45 all of the structures showed statistical significant difference between photon and proton beam, as illustrated in Table 4.8. Figure 4.18 also illustrates this difference, where one can see that the doses are lower with proton beam. Some of the structures did not show statistical significant difference with the dose metrics V15 and V30. These structures had very low doses, mostly around 0, as illustrated in Table 4.9 and Figure 4.19. All of the test statistics can be seen in Appendix C.6. The complete descriptive statistics for the dose metrics can be seen in Appendix C.7.

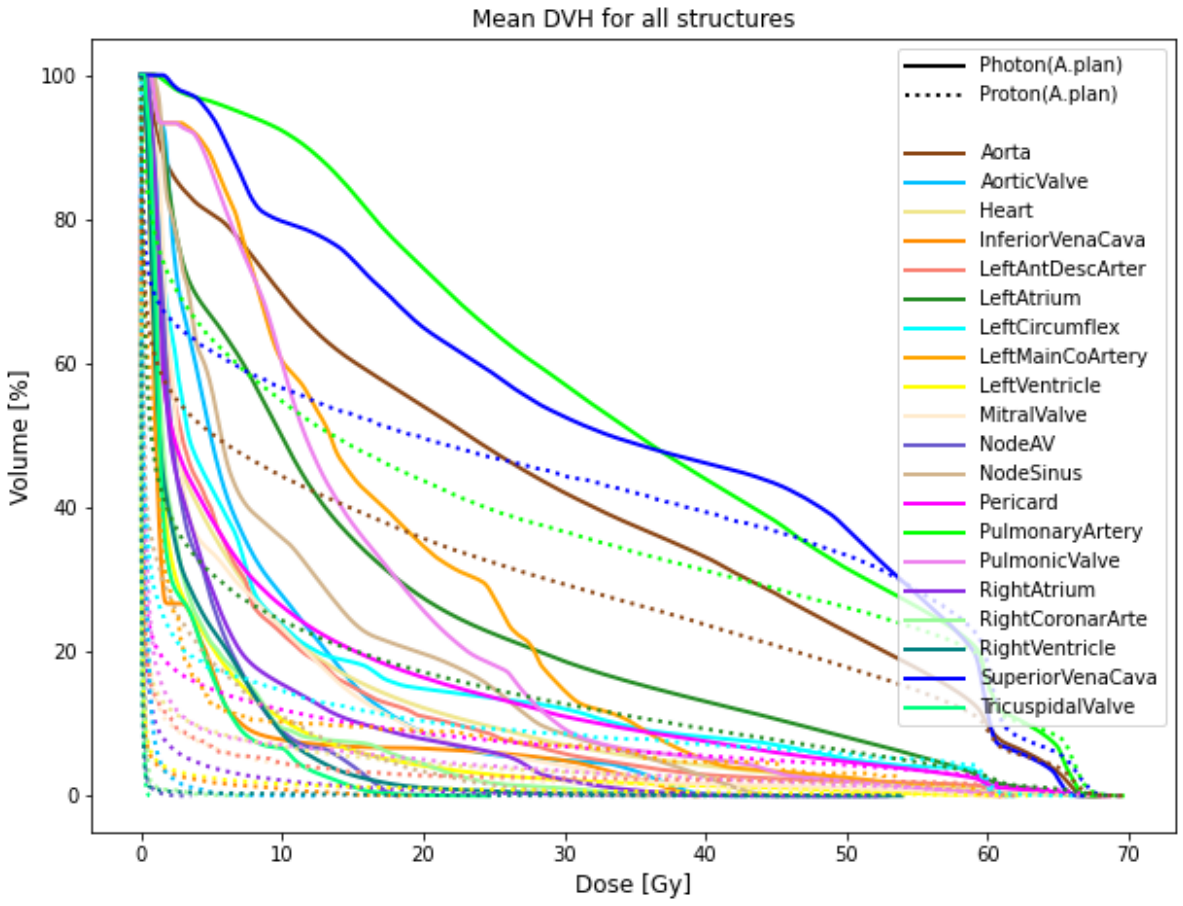

Figure 4.17: Plot of mean DVH curves for the structures, comparing proton and photon beam planning on A.plan.

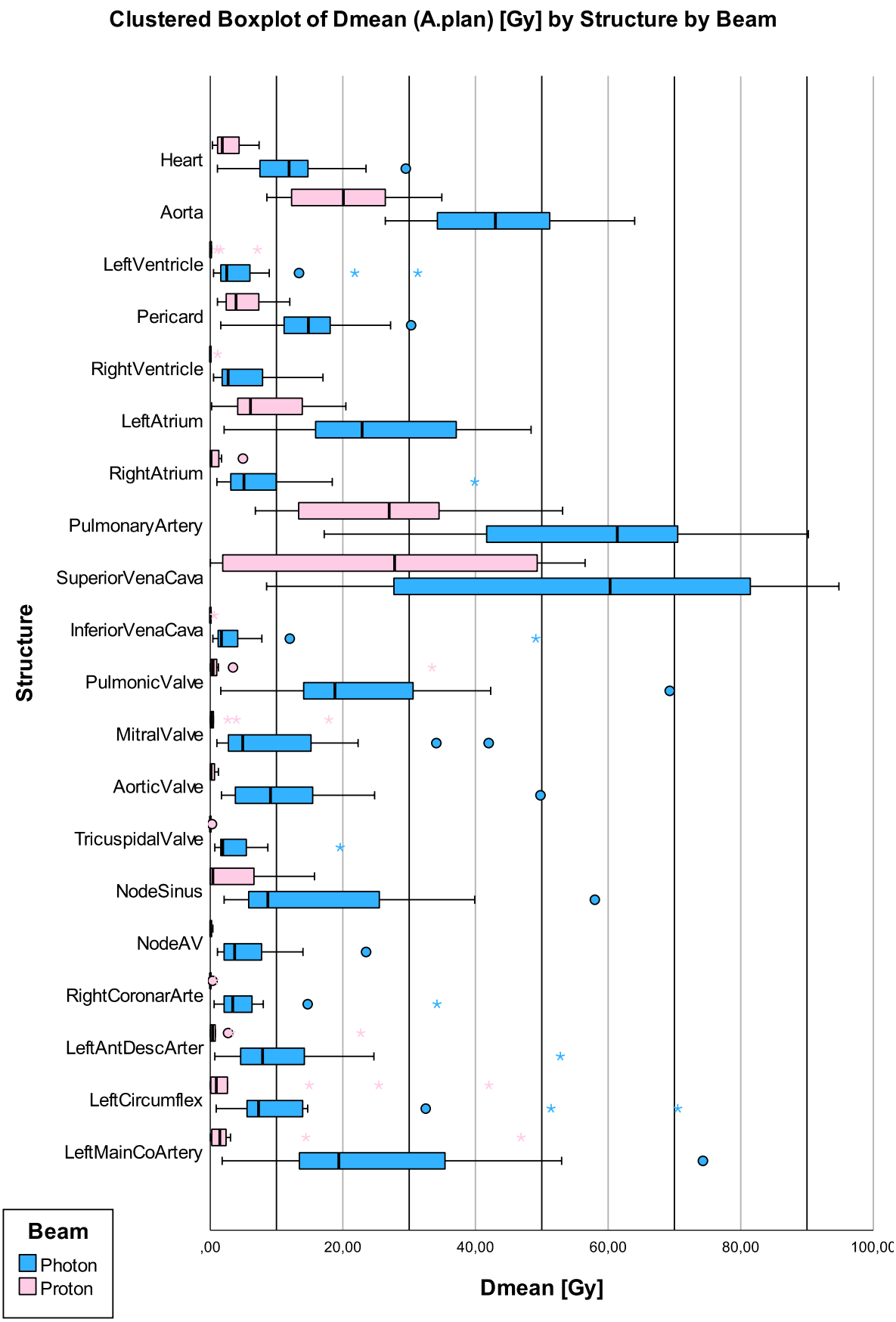

Figure 4.18: Boxplot of Dmean comparing proton and photon beam planning on A.plan, sorted by volume.

Table 4.8: Median Dmean dose [Gy] to the structures, comparing photon and proton beam planning of A.plan. All of the structures showed statistical significant difference between the photon and proton dose with the Wilcoxon signed-rank test ($\alpha = 0.05$). The reduction is the relative reduction from photon to proton.

	Median Dmean (IQR) [Gy]				
Structure ID	**Photon**		**Proton**		**Reduction [%]**
Heart	11.9	(7.5-14.75)	1.82	(1.24-4.17)	84.7
Aorta	43.0	(34.25-51.2)	20.08	(12.45-26.27)	53.3
LeftVentricle	2.5	(1.6-6.0)	0.05	(0.02-0.15)	98.0
Pericard	14.8	(11.15-18.1)	3.90	(2.65-7.13)	73.7
RightVentricle	2.7	(1.8-7.9)	0.02	(0.0-0.08)	99.3
LeftAtrium	22.9	(15.9-37.1)	6.08	(4.26-13.52)	73.4
RightAtrium	5.1	(3.1-9.95)	0.13	(0.01-1.26)	97.5
PulmonaryArtery	61.4	(41.7-70.5)	26.99	(15.39-33.18)	56.0
SuperiorVenaCava	60.3	(27.7-81.45)	27.81	(2.94-48.36)	53.9
InferiorVenaCava	1.7	(1.2-4.15)	0.04	(0.0-0.11)	97.9
NodeSinus	8.7	(5.8-25.5)	0.4	(0.02-5.81)	95.4
NodeAV	3.7	(2.1-7.75)	0.07	(0.02-0.18)	98.2
PulmonicValve	18.8	(14.1-30.6)	0.46	(0.12-0.94)	97.6
MitralValve	4.9	(2.75-15.2)	0.21	(0.06-0.48)	95.8
AorticValve	9.1	(3.8-15.45)	0.14	(0.05-0.57)	98.5
TricuspidalValve	1.9	(1.6-5.45)	0.02	(0.0-0.07)	98.9
RightCoronarArte	3.4	(2.1-6.3)	0.03	(0.0-0.1)	99.3
LeftAntDescArter	7.9	(4.6-14.2)	0.36	(0.07-0.73)	95.4
LeftCircumflex	7.3	(5.55-13.95)	0.93	(0.19-2.48)	87.3
LeftMainCoArtery	19.4	(13.45-35.4)	1.44	(0.36-2.35)	92.6

Table 4.9: Median V30Gy [%] dose to the structures, comparing photon and proton beam planning of A.plan. The structures that showed statistical significant difference between photon and proton dose with V30Gy are marked as bold. The structures that showed statistical significant difference between photon and proton dose with V15Gy are marked with * ($\alpha = 0.05$).

	Median V30Gy (IQR) [%]			
Structure ID	**Photon**		**Proton**	
Heart	**4.95***	(3.48-9.19)	**2.05**	(1.5-4.7)
Aorta	**38.68***	(31.1-54.1)	**30.67**	(14.37-41.23)
LeftVentricle	**0.0***	(0.0-0.17)	**0.0**	(0.0-0.0)
Pericard	**10.86***	(6.83-13.85)	**5.468**	(3.74-9.34)
RightVentricle	0.0	(0.0-0.0)	0.0	(nan-nan)
LeftAtrium	**13.33***	(8.51-30.43)	**8.051**	(4.55-19.22)
RightAtrium	**0.0***	(0.0-0.86)	**0.0**	(0.0-0.0)
PulmonaryArtery	**64.06***	(31.94-82.71)	**36.98**	(21.17-48.51)
SuperiorVenaCava	**60.59***	(3.28-97.46)	**56.66**	(0.17-75.38)
InferiorVenaCava	0.0*	(0.0-0.0)	0.0	(0.0-0.0)
NodeSinus	**0.0**	(0.0-3.35)	**0.0**	(0.0-0.0)
NodeAV	0.0	(0.0-0.0)	0.0	(0.0-0.0)
PulmonicValve	**0.0***	(0.0-7.25)	**0.0**	(0.0-0.0)
MitralValve	0.0*	(0.0-0.2)	0.0	(0.0-0.0)
AorticValve	0.0*	(0.0-0.0)	0.0	(0.0-0.0)
TricuspidalValve	0.0	(0.0-0.0)	0.0	(0.0-0.0)
RightCoronarArte	0.0	(0.0-0.0)	0.0	(nan-nan)
LeftAntDescArter	0.0*	(0.0-2.7)	0.0	(0.0-0.0)
LeftCircumflex	0.0*	(0.0-7.79)	0.0	(0.0-0.13)
LeftMainCoArtery	0.0*	(0.0-6.68)	0.0	(0.0-0.0)

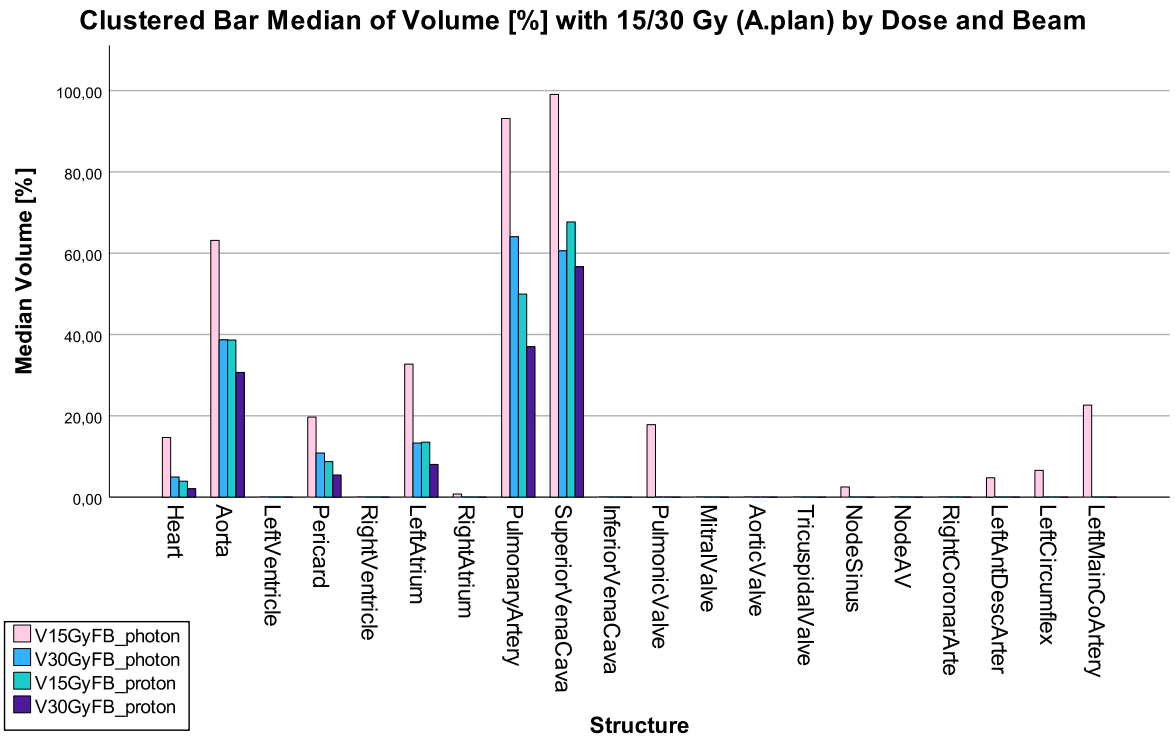

Figure 4.19: Clustered bar of median of the volume [%] receiving 15 or 30 Gy, for both proton and photon, sorted by volume of the structure.

4.4.3 The Heart as Surrogate Parameter

Photon Beam

The difference between the mean heart dose and the mean dose to the substructures of this project is illustrated by comparing Figures 4.20 and 4.21. A Wilcoxon signed-rank test was performed to find which substructures showed a statistical significant difference from the Dmean to the heart, shown in Table 4.10. The full test results can be found in Appendix C.8.

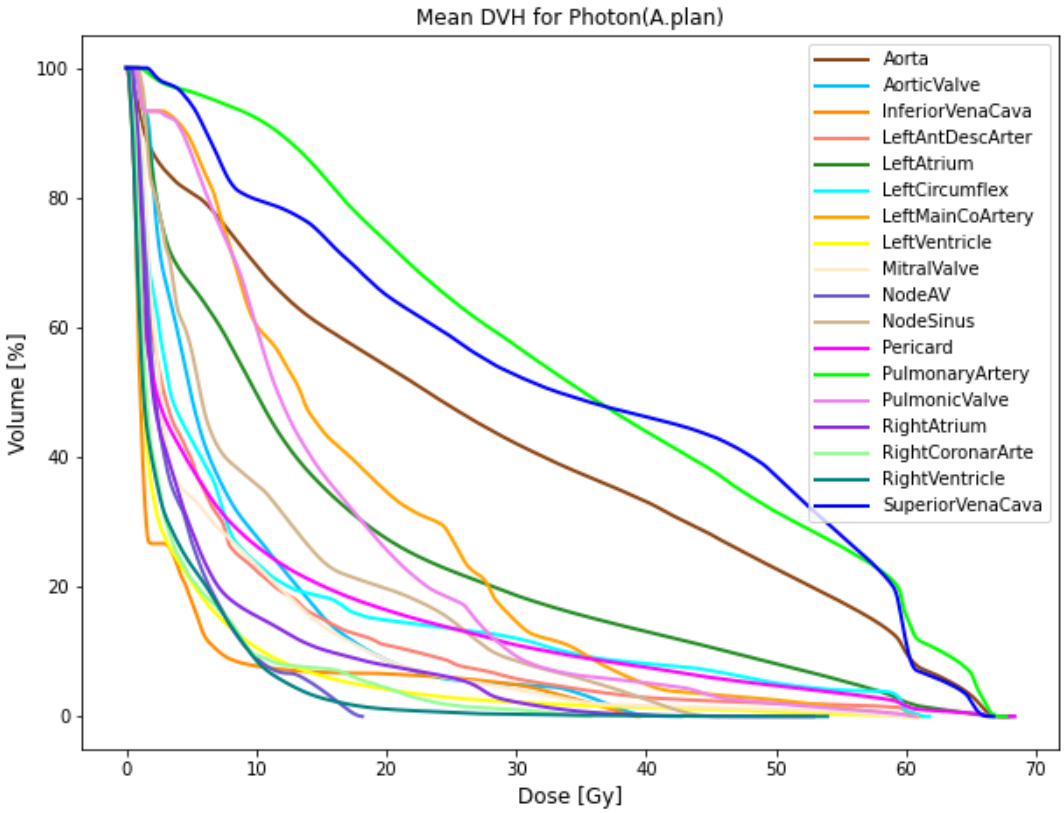

Figure 4.20: Plot of mean DVH curves for all substructures of all patients, from A.plan.

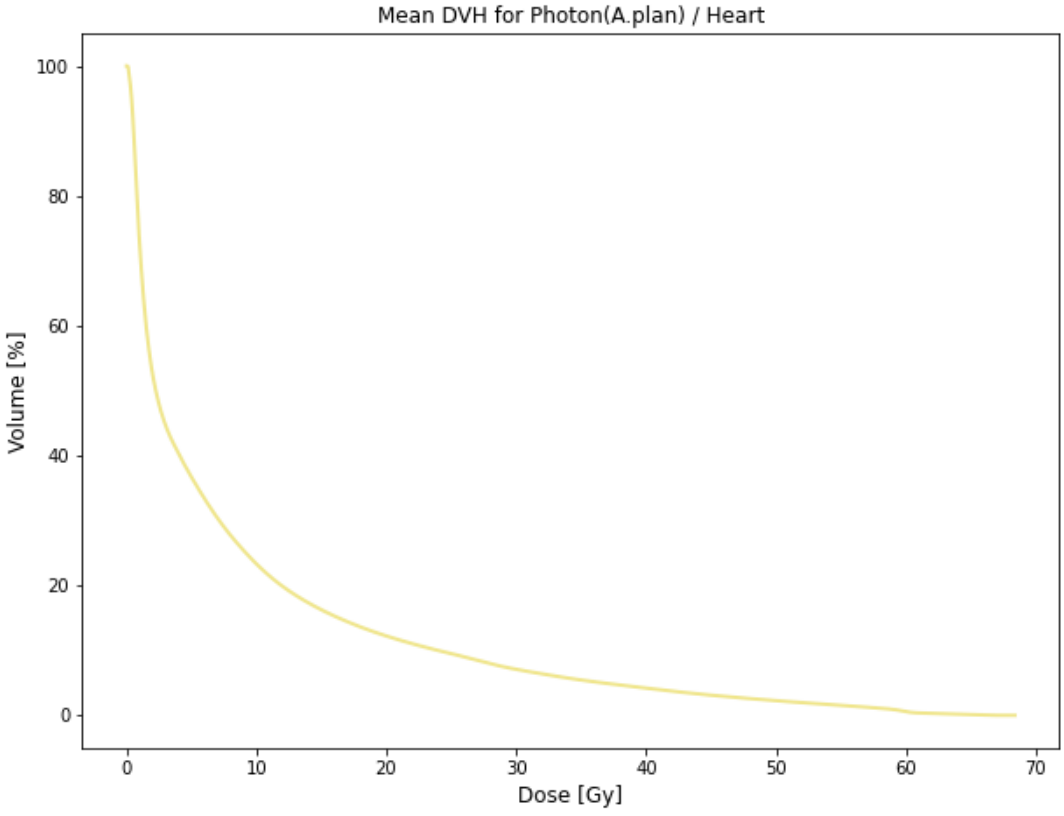

Figure 4.21: Plot of mean DVH curves for the heart of all patients, from A.plan.

Table 4.10: The median Dmean for each structure in photon beam planning of A.plan. The $+/-$ column represents if the dose to the substructure is significant greater or lesser than the dose to the heart. Diff means difference from Dmean heart, and the % were made by dividing with the Dmean heart value. The substructures that showed statistical significant difference with the heart dose are marked as bold ($\alpha = 0.05$).

		Median Photon Dmean				
Group	**Structure ID**	**Median (IQR) [Gy]**		**Diff [Gy]**	**Diff [%]**	**+ / -**
	Heart	*11.9*	*(7.5-14.75)*			
Chambers	RightAtrium	**5.1**	(3.1-9.95)	-6.8	-57.1	-
	RightVentricle	**2.7**	(1.8-7.9)	-9.2	-77.3	-
	LeftAtrium	**22.9**	(15.9-37.1)	11.0	92.4	+
	LeftVentricle	**2.5**	(1.6-6.0)	-9.4	-79	-
Valves	TricuspidalValve	**1.9**	(1.6-5.45)	-10.0	-84	-
	PulmonicValve	**18.8**	(14.1-30.6)	6.9	58	+
	MitralValve	**4.9**	(2.75-15.2)	-7.0	-58.8	-
	AorticValve	9.1	(3.8-15.45)	-2.8	-23.5	
Coronary arteries	LeftMainCoArtery	**19.4**	(13.45-35.4)	7.5	63	+
	LeftAntDescArter	7.9	(4.6-14.2)	-4.0	-33.6	
	LeftCircumflex	7.3	(5.55-13.95)	-4.6	-38.7	
	RightCoronarArte	**3.4**	(2.1-6.3)	-8.5	-71.4	-
Vessels	Aorta	**43.0**	(34.25-51.2)	31.1	261.3	+
	PulmonaryArtery	**61.4**	(41.7-70.5)	49.5	416	+
	SuperiorVenaCava	**60.3**	(27.7-81.45)	48.4	406.7	+
	InferiorVenaCava	**1.7**	(1.2-4.15)	-10.2	-85.7	-
Other	NodeSinus	8.7	(5.8-25.5)	-3.2	-26.9	
	NodeAV	**3.7**	(2.1-7.75)	-8.2	-68.9	-
	Pericard	**14.8**	(11.15-18.1)	2.9	24.4	+

Some of the structures had statistical significant difference from Dmean heart. This is visually presented in Figure 4.22. The anatomical shapes and placement of these structures are also illustrated in Figure 4.23. These structures' DVH curves for both photon and proton can be seen in Figure 4.25. Other structures received significant less than calculated to the heart, illustrated in Figure 4.24.

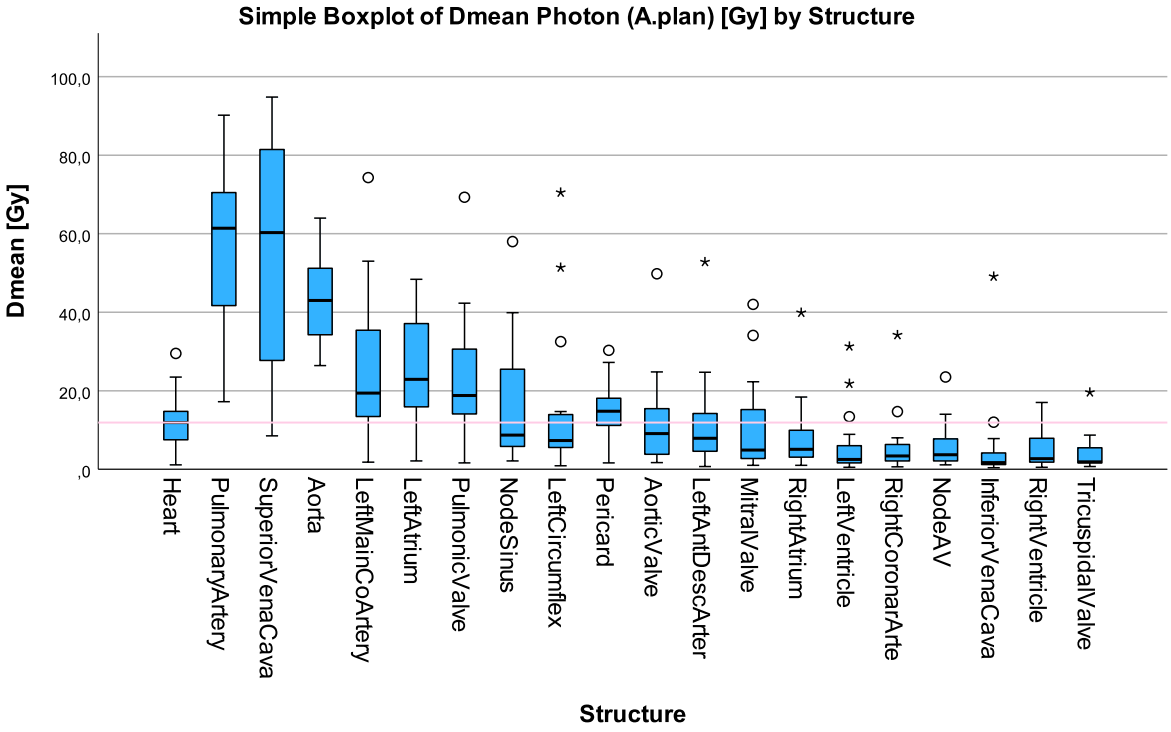

Figure 4.22: Boxplot of photon Dmean to the structures with A.plan. Sorted by Dmean value. The pink line represents the median Dmean for the heart (= 11.9 Gy).

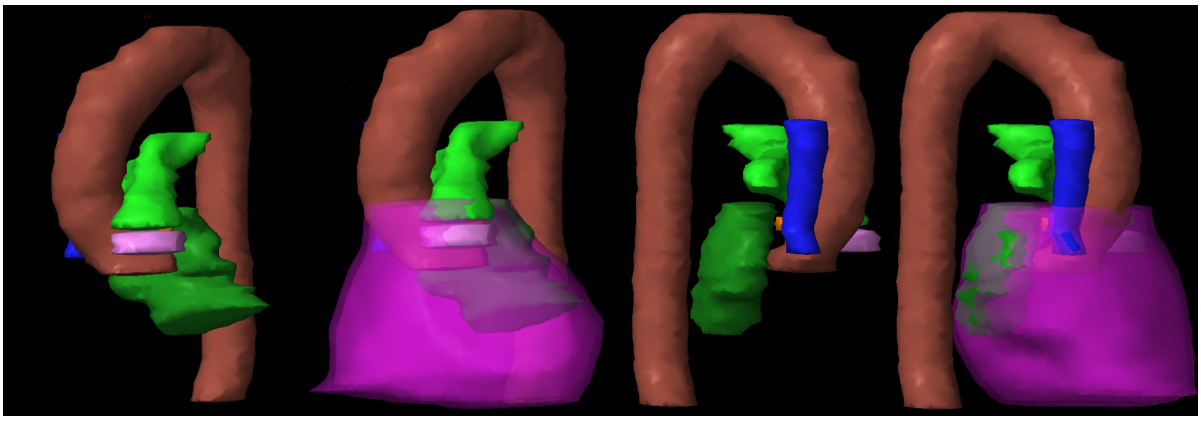

Figure 4.23: Illustration of the substructures with photon beam with a dose greater than the dose to the heart. Ventral and dorsal view, without and with the pericardium.

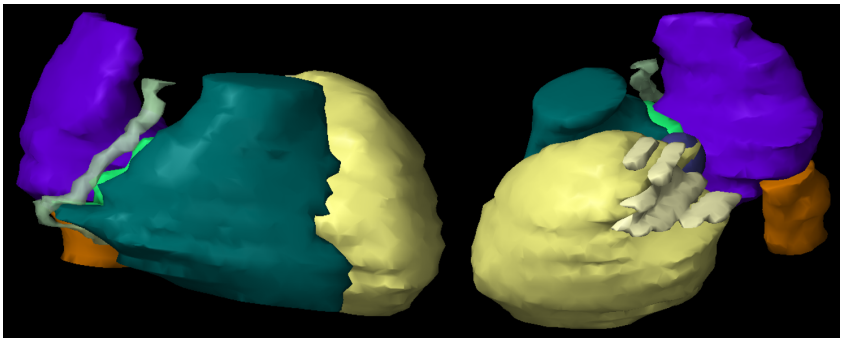

Figure 4.24: Illustration of the substructures with photon beam with significant lesser dose than the dose to the heart. Ventral and dorsal view.

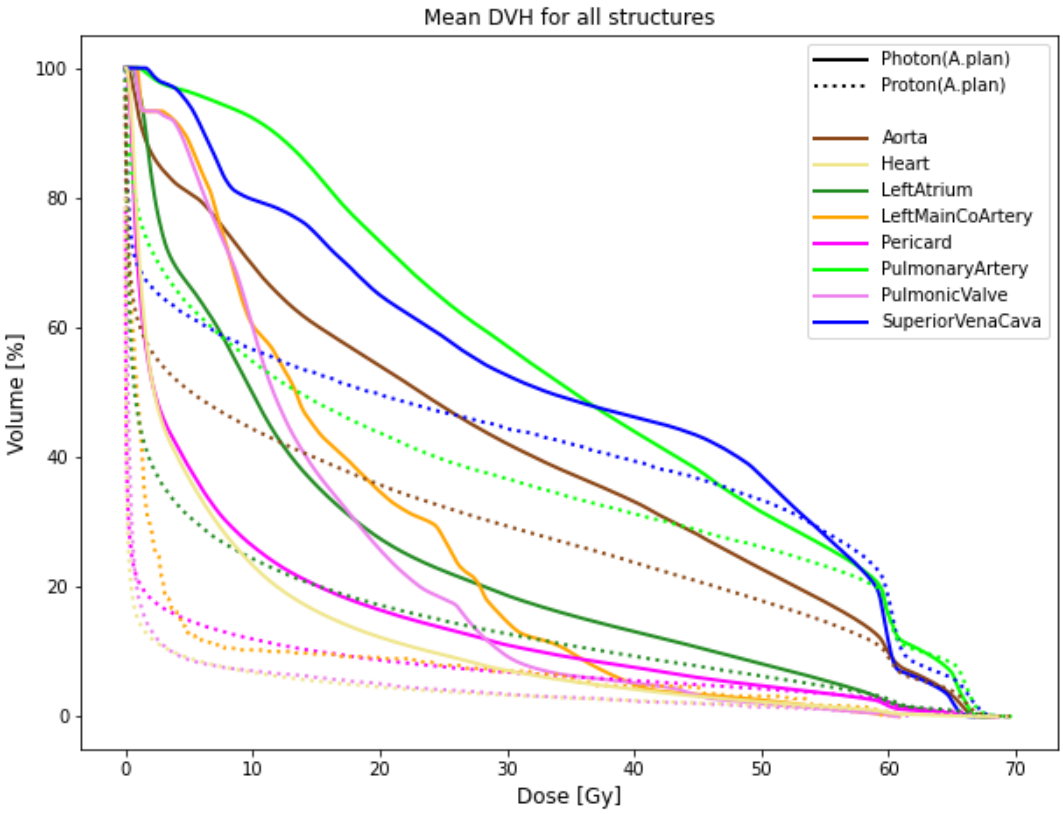

Figure 4.25: Mean DVH of the structures with significant change from the heart, and an increase in median Dmean. Can see the curves for both photon and proton beam planning.

Proton Beam

The same comparison of the mean heart dose and the mean dose to the different substructures was performed with proton beam dose. In which degree Dmean represents the substructures is illustrated in Figure 4.26. A Wilcoxon signed-rank test was performed to find if there were statistical significant difference between Dmean for the substructures and the heart, presented in Table 4.11. The full test results can be seen in Appendix C.9. The DVH of the substructures with significant greater mean dose than the heart can be seen in Figure 4.27.

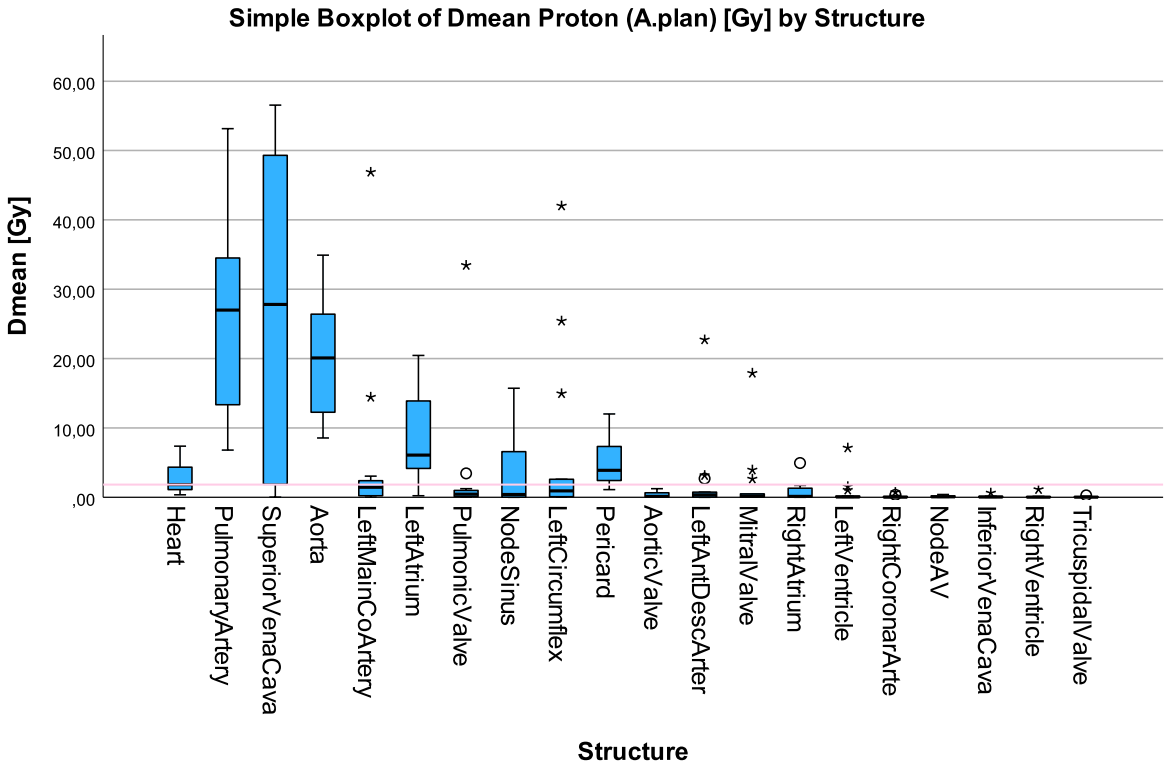

Figure 4.26: Boxplot of proton Dmean to the structures with A.plan. Sorted by value. The pink line represents the median Dmean for the heart (= 1.82 Gy).

Table 4.11: The median Dmean for each structure in proton beam planning of A.plan. The + / - column represents if the dose to the substructure is significant greater or lesser than the dose to the heart. Diff means difference from Dmean heart, and the % were made by dividing with the Dmean heart value. The substructures that showed statistical significant difference with the heart dose are marked as bold ($\alpha = 0.05$).

		Median Proton Dmean				
Group	**Structure ID**	**Median (IQR) [Gy]**		**Diff [Gy]**	**Diff [%]**	**+ / -**
	Heart	*1.82*	*(1.24-4.17)*	*0.0*	*0.0*	
Chambers	RightAtrium	**0.13**	(0.01-1.26)	-1.69	-93.1	-
	RightVentricle	**0.02**	(0.0-0.08)	-1.80	-98.9	-
	LeftAtrium	**6.08**	(4.26-13.52)	4.26	234.1	+
	LeftVentricle	**0.05**	(0.02-0.15)	-1.77	-97.3	-
Valves	TricuspidalValve	**0.02**	(0.0-0.07)	-1.8	-98.9	-
	PulmonicValve	**0.46**	(0.12-0.94)	-1.36	-75.0	-
	MitralValve	0.21	(0.06-0.48)	-1.61	-88.7	
	AorticValve	**0.14**	(0.05-0.57)	-1.68	-92.3	-
Coronary arteries	LeftMainCoArtery	1.44	(0.36-2.35)	-0.38	-20.9	
	LeftAntDescArter	**0.36**	(0.07-0.73)	-1.46	-80.2	-
	LeftCircumflex	0.93	(0.19-2.48)	-0.89	-48.9	
	RightCoronarArte	**0.03**	(0.0-0.1)	-1.80	-98.6	-
Vessels	Aorta	**20.08**	(12.45-26.27)	18.26	1003.3	+
	PulmonaryArtery	**26.99**	(15.39-33.18)	25.17	1383.0	+
	SuperiorVenaCava	**27.81**	(2.94-48.36)	25.99	1427.7	+
	InferiorVenaCava	**0.04**	(0.0-0.11)	-1.79	-98.1	-
Other	NodeSinus	0.4	(0.02-5.81)	-1.42	-78.0	
	NodeAV	**0.07**	(0.02-0.18)	-1.76	-96.4	-
	Pericard	**3.895**	(2.65-7.13)	2.075	114.0	+

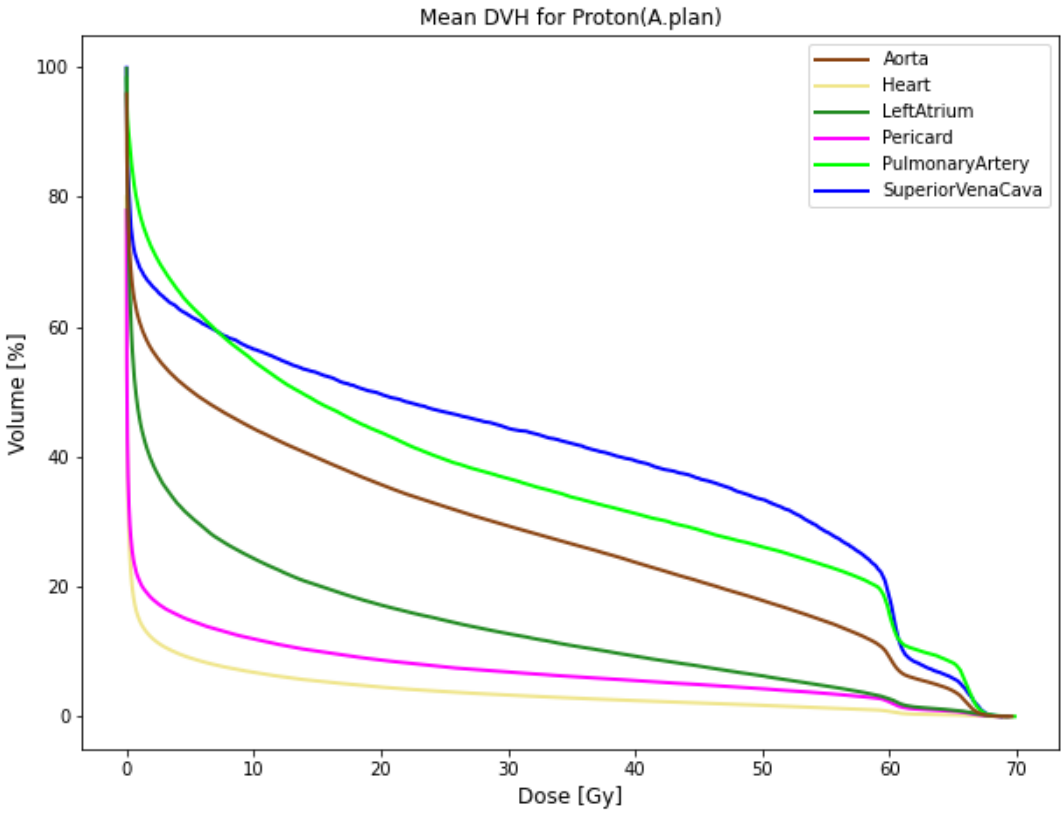

Figure 4.27: Mean DVH of the substructures with significant change from the heart Dmean and an increase in median Dmean, in proton beam planning.

Chapter 5

Discussion

In this chapter, an examination of the project's results is presented, focusing on a detailed analysis of each component. Selected results were compared with findings from existing literature and other relevant research studies. The uncertainties associated with the project are also discussed, shedding light on the limitations and potential areas for further exploration.

5.1 Geometric Comparison

Volume

Upon examining the volumes of the various structures, it became evident that they exhibit a wide range. Comparing these volumes to those in the Socha et al. atlas, it is apparent that they fall within a similar range [60]. The superior and inferior vena cava were just above the limit to be classified as a "large" structure. Many of the structures had a minor volume, that impacts how the results can be interpreted later. C.plan exhibited a higher frequency of deviations from A.plan compared to A.w1, with most structures being larger in C.plan. The heart was much larger with C.plan, and the pericardium naturally followed this, as it is defined by the heart. With contrast, the exact edge of the heart is easier to identify, making it larger. The right ventricle and the left atrium were also shown to be larger in volume for C.plan than A.plan, while the two other heart chambers not exhibited the same change. It seemed like the increase in heart volume was partly due to these two structures being larger defined for C.plan. The pulmonary artery was also much larger with C.plan, this can be because it is easier to define, and therefore defined higher in the scans.

The only structure with significant difference and lower median volume for C.plan

than A.plan, was the aortic valve. One can see that A.plan had a higher third quartile, and in Figure 4.5 one can see that especially one patient had a high value, while most values lied higher for A.plan than C.plan and A.w1. This may be explained by the selection bias of the candidate. In comparing C.plan to A.plan, three of the coronary arteries showed significant differences, all exhibiting higher median values for C.plan. This difference was expected, as the coronary arteries are easier to identify with the contrast liquid. However, the left main coronary artery, being the smallest, remained within the same range.

Dice coefficient

To avoid having any overlap, the structures must move over their entire width or height. Because large structures need to move farther to avoid overlapping, the Dice coefficient was predicted to be higher with larger structures than smaller structures. Poor overlap is therefore to be expected by the smaller structures. Figure 4.10 showed a correlation between volume and Dice coefficient, with the small structures having lower D, especially the coronary arteries. The figure also illustrated that the pericardium did not overlap well, as was expected even though it has a large total volume, but was made up of a 3 mm thin wall.

The geometric metrics, Dice coefficient and Hausdorff distance, were both calculated slice by slice, and then used with the mean value for each structure for each patient. An additional uncertainty then arises when using these metrics. The heart is expected to be alike in both metrics over the different scans as they are previously drawn by professionals, and the new ones were drawn with regard to the old ones.

Dice coefficient can also be used as a tool when creating atlases, to compare when different people contour the same structures. Some of the substructures in this project were provided with Dice values in the atlas publications, but not all of them. It is worth noting that the median values in this project represented variations across different patients, whereas the values for the atlases were obtained by averaging the contouring of different observers on the same patient. The atlases approach is therefore without the uncertainties related to anatomical movement and patient differences.

Duane et al. also experienced poor Dice coefficient for the coronary arteries, with mean values between 0.10 and 0.53. Their mean LMCA values was 0.45, with data ranging from 0.09 to 0.76. Their mean overlap was better than the median for this

project, with values 0.14 for C.plan and 0.21 for A.w1. From Figure 4.7 one can see that the fourth quartile of A.w1 also ranges up to above 0.50, but not close to 0.76, and can also see that results were also 0.0. Other than the LMCA the coronary arteries were split into segments that were not used in this project, and therefore can not be precisely compared. However, the average values of 0.10-0.53 exceed the median values of 0.11-0.21 in this project [59].

Duane et al. also calculated Dice coefficients for the left ventricle, with a mean of 0.91, and values ranging from 0.89-0.94 [59]. This was also higher than for this project, with median (IQR) 0.76(0.75-0.81) and 0.81(0.72-0.83) for C.plan and A.w1, respectively. This may suggest that that this project had lower accuracy, which might be caused by patient differences.

Socha et al., that were used for contouring heart valves, also calculated Dice coefficients when creating their atlas. The atlas was delineated based on AVE-4D-CT scans, making it suitable for comparison with the A.w1 values in this case. This project achieved higher median Dice coefficients for both the pulmonic and aortic valves. The mean values reported by Socha et al. for the pulmonic and aortic valves were 0.68 and 0.49, respectively, whereas in this project, the median values were 0.84 for the pulmonic valve and 0.82 for the aortic valve. These might be higher for this project because the Dice coefficient in this project only was calculated if they were present in the same scan, creating a falsely high Dice for a volume. The mitral valve had the mean value of 0.45 for Socha et al., while this project found a slightly lower median value of 0.43. Both Socha et al. and this project reported the same mean/median value of 0.45 for the tricuspid valve. It is evident that Socha et al. observed a similar trend as identified in this project, with lower overlap values for the AV valves [60].

The atlas by Socha et al. also included analysis of their atlas' performance on contouring of other structures. Most of these values were slightly higher than those observed in this project, which could be due to the fact that they were compared within the same patient. Socha et al. reported a mean Dice coefficient of 0.80 for the right ventricle, whereas this project obtained a median value of 0.78. In terms of the right atrium, they achieved a mean coefficient of 0.83, whereas the median value for this project was 0.75. Regarding the left atrium, they obtained a mean coefficient of 0.85, while the median for this project was 0.79. They also experienced higher Dice coefficients for the coronary arteries than this project [60].

Most of the Dice coefficient did not show significant change over time, with comparisons of C.plan and A.w1. The only two structures who did show a significant change were the pericardium and the LMCA. The pericardium were earlier found to be significant different in volume from C.plan to A.plan, with a higher median value for V.C.plan. That D.C.plan is significant different from D.A.w1, with a larger median D.C.plan, is therefore to be expected. With a larger volume more is able to overlap. LMCA had a lower median overlap with D.C.plan than D.A.w1. Both had little overlap, with low Dice coefficients. A.w1 might exhibit improved alignment with A.plan compared to C.plan due to both being contoured on AVE-4D-CT. With the smallest structure, the contours were based more on estimation rather than direct visualization, making the estimations in AVE-4D-CT a better match for each other than if they were based on what was seen in C.plan. So the better overlap with A.w1 might be because they are further from the actual location of the artery.

The tricuspid valve also stands out with visibly different Dice coefficients for C.plan and A.w1, and had a p-value very close to reject the null hypothesis. This shows that the border between the right atrium and the right ventricle varies. There is seen less difference on the mitral valve, suggesting that the border on the left side may vary less. Figure 4.10 shows a difference between the semilunar and AV valves, with higher D for the semilunar valves. This suggests that factors beyond size may influence the variation in D values among structures, at least for the heart valves. The semilunar valves, the aortic and pulmonic valve, had higher median Dice coefficient than the rest of the small structures. This can be because they were contoured in fewer slices, but with larger area in each slice, in the main window used for contouring.

Uncertainty arises in this case because the mean value was utilized for each patient's structure, leading to potential inaccuracies. This measure may not be suitable for small structures contoured in only a few transversal slices, as the limited number of slices makes it challenging to determine if the mean is a reliable indicator. Moreover, the Dice coefficient was exclusively calculated in the slices where the structures were present in both scans. This provides new insight into the high Dice coefficient observed for the aortic and pulmonic valves. Since the calculation was confined to the scans where both valves were present, it is expected that their overlap would be substantial, given the extensive contour area in each slice. Conversely, the other valves, which were often located in the same slices across more scans but with smaller areas, yielded lower Dice scores. It is possible that they would have performed better if analyzed from a different plane.

Given that only 15 patients were used to calculate D for A.w1, and even fewer (9) for C.plan, the presence of outliers should not be underestimated and should be carefully considered. Figure 4.7 indicates that many of the structures exhibit outliers in the D value. Moreover, several structures have a wide range of quantiles, while others display the presence of outliers. These findings highlight substantial variation in results among patients, emphasizing the need for a larger sample size for a comprehensive analysis.

Hausdorff Distance 95% Percentile

There was not found any statistical significant difference between the H values calculated for C.plan and A.w1. The H values of the structures showed variations, but remained in a consistent range. Some patients exhibited outlier values, indicating longer distances compared to others. The correlation between volume and H value was not evident, as structures of all sizes displayed both low and high H values. The variations in H values appeared to be more patient-specific rather than structural. The distances of both C.plan and A.w1 varied, implying that neither anatomical movement nor changes over time resulted in different alterations of the distances from A.plan. The atlases used in this project did not use this as a metric for comparison.

Visual Differences

Upon looking after structural variances between the substructures delineated with and without contrast, only small repeated differences were identified, explained by dissimilarities in the imaging techniques. One of the differences noted was that the coronary arteries appeared larger when depicted with contrast. Nonetheless, their placement remained consistent. This demonstrates that the contrast training may have been beneficial and made it simpler to make an educated assumption as to the location of the coronary arteries.

There was found a difference in the separation of the heart chambers. If a consistent pattern of either over-sizing or under-sizing of a particular structure was identified, it would be a cause for concern. However, in these instances, no such pattern has been observed. The logical explanation for the observed variation in the positioning of the pulmonic valve and pulmonary artery is attributed to the project's definition of the pulmonic valve, which is based on the left ventricle. This definition results in their

placement higher, as the left ventricle could have been more easily identified high on the contrast scans. Due to the increased complexity of determining visibility with AVE-4D-CT, the variability of the nodes also exhibited some variation. The placement of a small structure is observed to exhibit more variability, resulting in reduced accuracy for planning and determining the precise planned dose for that specific area.

5.2 Dose

Due to time constraints and in order to include all 15 patients, only AVE-4D-CT scans were utilized in this analysis. These scans were also previously observed to exhibit smaller volume changes compared to C.plan scans.

5.2.1 Robustness over Time

Photon Planning

Some structures showed statistical significant difference between the dose received in A.plan and A.w1, with different dose metrics. These being the left and right atrium, AVN and SVN, the mitral valve, and the left anterior descending coronary artery. All of these structures are placed at the top of the heart, as illustrated in Figure 4.13, except for LAD which begins at the top and then goes further down.

For all of the structures with significant change in dose the median dose metrics was higher for A.w1. This suggests that the structures actually get a higher dose than planned. This was also illustrated by the DVH curves in Figure 4.14. That the structures receives a greater dose than expected in planning is of concern and should be avoided. This may be because the structures have slightly moved between scans, making anatomical movement in the substructures an uncertainty for robust planning.

The dose varies among these structures, so there is no obvious correlation between dose size and robustness over time. The main thing in common between the significant structures seem to be the anatomical placement, at the superior part of the heart, except for the distal part of the LAD. Other than the LAD the structures also lie towards the posterior part of the heart. While some of the significantly changed structures were observed to have outliers, it is worth noting that other structures lacking this change also exhibited outliers.

As these structures lies close to each other it seems like in this location the dose matrix change more than for other regions of the heart. As the blood flows through the heart the density varies. During the cardiac cycle, as the heart pumps, the atria undergo complete emptying, effectively transferring blood into the ventricles. However, it is important to note that for the ventricles a portion of the blood remains within them [4]. This can cause a difference in density between the two groups of the heart chambers.

Due to the ventricles' larger size compared to the atria, the dose of radiation delivered to the ventricles is distributed over a larger volume and is subject to more changes [4]. Similar to the concept in geometric overlap, for small structures smaller changes in volume will have a more noticeable impact, resulting in variations in the received dose across the volume of the atria. This can explain the change in the dose to the atria over time. It would be interesting to see if the same structures varied to week 3 of treatment, but was not done in this project.

The fact that not all dose metrics were able to detect significant differences in dose for each structure suggests that the differences were not large-scale. However, utilizing multiple dose metrics proved to be valuable in identifying these differences, as multiple structures showed significant change with different metrics. All of the dose metrics was found with some statistical difference for certain structures, except for V30Gy. As many of the structures are small, the percent of the structure receiving this higher dose is most likely to be small. Then it makes sense that there was not found much difference between V30Gy of A.plan and A.w1. Multiple of the dose metrics were needed to detect statistical significant differences, and one might find others by using other metrics.

Due to the specific nature of this analysis, the candidate encountered difficulties in finding relevant literature to compare this particular aspect of the project with.

Proton Planning

For proton planning, the superior vena cava was the only structure that was found to show a statistical difference between the dose to A.plan and A.w1. This was showed in Figure 4.15, that the dose was decreased from A.plan to A.w1, meaning that the patient would get less than planned dose to the OAR. As the goal is to have the least amount of radiation to them it is not of as much concern, but it raises suspicion to the planning

process. This also means that proton beam planning seems more robust for most substructures of the heart, as most of the structures receive close to the exact planned dose.

Also for proton beam planning there were outliers present when comparing the dose, with some patients receiving higher doses. These outliers seem to exist for both A.plan and A.w1, showing that the doses stay the same over time, even though they range in value between patients.

5.2.2 Photon Planning VS Proton Planning

All of the structures had a statistical significant change in Dmean between photon and proton beam planning. All of the median Dmean doses were reduced with proton, with reductions between 53.5% and 99.3%. This shows that proton beam planning can reduce the dose to all of the substructures included in this project. Some of the structures did not have significant change of V15Gy or V30Gy between photon and proton. This is likely due to the percentage being very small for both, and therefore not much change were detected. There are mostly the small structures that have a very low V30Gy percentage, and some of the large ones, further away from the left base of the heart. The dose is also seen to be very low for many of the structures.

Certain structures receive minimal radiation doses with proton beam planning, with Dmean values below 0.05. These structures includes the right and left ventricle, inferior vena cava, tricuspid valve, and the right coronary artery. These are the structures towards the bottom and mostly right side of the heart. This suggest that these would likely not be harmed with proton therapy. If the structures not have much to gain from reducing the dose, if the photon beam planning dose already is quite low, it is not as important that the dose is very low with proton.

On the other hand, most of the great vessels, the aorta, the superior vena cava and pulmonary artery stand out. They have the three highest Dmean values of the structures, and are over 50% reduced with proton beam planning. This is substantial in sparing these substructures. They are all placed above the heart, making them closer to some possible targets for radiation in the lung.

That all of the structures were found to have significant change between the Dmean dose between IMRT and IMPT means that the entirety of the heart received less radiation. Boer et al. also found that the heart Dmean dose was lower with IMPT than IMRT

[3]. If a lower dose to heart will decrease the toxicity and increase the overall survival of patients this can be very important.

Both Niedzielski et al. and Wang et al. employed proton therapy and IMRT plans for radiation treatment in the chest region to make predictions regarding cardiac disease and patient survival. Niedzielski et al. found that Dmean dose to the left atrium performed the best as a predictor for pericardial effusion [35]. In another study by Wang et al., to predict MCEs, defined in Table 4.5, LAD V30Gy performed the best, while LMCA Dmean performed the best to predict OS of the patients [39]. This can be transferred to this project as these metrics were calculated. In this project, the median values for LAD V30Gy were 0 for both photon and proton beams, making it ineffective as a significant predictor for MCEs since there was little dose variation to study.

In their study, Ferris et al. discovered that when comparing IMPT to photon VMAT plans with cardiac substructure sparing intentions, IMPT still demonstrated superior performance for the cardiac structures. They observed a significant change in all substructures' mean dose (Dmean) with IMPT. The structures investigated in their research were identical to those considered in this project, except for the exclusion of the IVC, pericardium, and the sinus node [72]. When comparing Ferris et al. to this project, where IMRT plans did not incorporate cardiac substructure sparing, it can be inferred that implementing a dose constraint for the substructures in this project would not yield superior results or lower doses compared to the IMPT plan utilized here. Consequently, it is likely that IMPT will outperform photon plans, even when the latter are designed with substructure sparing in mind. This indicates significant potential for reducing the dose to all cardiac substructures through proton treatment of LA-NSCLC.

5.2.3 The Heart as Surrogate Parameter

For all radiation planning the placement of the tumor is crucial for the radiation of the surrounding tissue. Most of the patients included in this project had mediastinal lymph nodes (n = 14). As these nodes are located in the mediastinum, and the radiation is directed towards them, this will affect which substructures get the most radiation, most likely the ones that also are close to these lymph nodes. The heart is placed in mediastinum medium, while the mediastinal lymph nodes can be found in the mediastinum posterior, both superior and inferior. This means that the posterior structures of the heart are closer to the targeted lymph nodes, and more likely to receive a higher radiation dose. Also given that the mediastinal lymph nodes are located from superior above

the heart and extend inferior towards the end of the heart, the upper region is more susceptible to receiving a higher radiation dose compared to the lower region of the heart. The apex of the heart is situated at a distance from the mediastinal lymph nodes, making it less susceptible to receiving a higher radiation dose as a result of lymph nodes being targeted.

The tumors of the patients are varied and placed in different lobes of the lungs, which will cause different radiation among the patient group for this target. As only 1 patient only had target volume as primary tumor without mediastinal lymph nodes this group of patients of LA-NSCLC may be underrepresented in this project. Only one TNM combination of stage IIIA includes N0 status, without spread to the lymph nodes. Stage IIIA was the most common among Norwegians with NSCLC stage III in 2021 according to Kreftregisteret, but does not include the exact number of different classifications within the patient group [73]. This decreases the overall validity of this project, as its findings may not fully represent the entire patient group.

The heart is located in the center of the body, with a greater expansion towards the left side. This causes the right side of the heart to be more centrally located, while the left side extends more to cover a portion of the left lung. If one compares two patients, one with a tumor centrally in the right lung, and the other with a tumor centrally in the left lung, due to the positioning of the tumor, the left side is more prone to receiving a higher dose of radiation. This is because the left side of the heart is in closer proximity to the left lung compared to the right side of the heart and the right lung.

Accurate knowledge of the specific location of involved lymph nodes is crucial for assessing the radiation dose to various regions of the heart. This requires a comprehensive understanding of the anatomy of the cardiovascular system, lungs, and lymphatic system, as well as their spatial relationships. To determine the general applicability of this project's results to all patients with LA-NSCLC, a thorough understanding of the involved lymph nodes is necessary. Furthermore, precise identification and localization of affected lymph nodes within this patient group would be beneficial.

Photon Planning

Many of the substructures showed a difference in Dmean dose between the heart and the specific substructure. If they get less than the heart this is not of much concern, as it it less likely to cause harm with smaller dose. But the substructures that were not

well represented by the mean heart dose, and receives higher dose than expected by this parameter, could be an issue. This was found for seven of the substructures: the left atrium, the pulmonic valve, the LMCA, the aorta, the pulmonary artery, the superior vena cava and the pericardium.

The most significant increase in radiation exposure was observed in the three affected great vessels in comparison to the heart. The aorta, pulmonary artery, and superior vena cava received considerably higher radiation doses, with median Dmean values of 43.0 Gy, 61.4 Gy, and 60.3 Gy, respectively, whereas the heart received 11.9 Gy. Momin et al. conducted a study focusing on 15 substructures of the heart and cardiovascular system. In their routine clinical treatment plans, which resemble the approach in this project, the ascending aorta, had a Dmean of 47.47 Gy. The pulmonary artery received a Dmean of 53.02 Gy, and the superior vena cava received a Dmean of 51.9 Gy [67]. The higher Dmean observed in the ascending aorta compared to the combined descending and ascending aorta in this project implies that a larger proportion of the dose is delivered to the former. Additionally, both the pulmonary artery and superior vena cava received higher doses in this project compared to the findings of Momin et al. This indicates that lymph node involvement in the patients of this project may contribute to increased dose to these structures. It is worth noting that in Momin et al.'s study, patients with NSCLC were treated with a lower dose, of 60 Gy, which could explain the lower mean doses observed in their results. They also used a different atlas for contouring, which can explain some of the differences.

All of these vessels are mostly outside of the heart structure in contouring, and therefore not expected to fit as well as the structures inside the heart when it comes to dose. However, it is of concern, and could influence the patient. These structures transport a significant portion of the blood that circulates throughout the body, and within this blood, various types of immune cells are present among other components [4]. Exploring how the radiation treatment at this radiation dosage level impacts the efficacy of immune therapy would be interesting.

The other structures with significant difference and higher median than the heart are located within the heart. The left atrium, the pulmonic valve, LMCA and the pericardium are all in different groups of the heart, but lie within the same region of the heart, as illustrated in Figure 4.23. Pericardium is particularly interesting as it is based on the heart volume, and is therefore expected to receive similar dose as the heart. Therefore this increase may be because of the volume of the pericardium laying at the

base of the heart.

That the base of the heart receives higher dose has been found in multiple other studies. In 2017, McWilliam et al. published a retrospective study that found that as a region, the base of the heart, was significant. The study discovered a correlation between radiation doses above 8.5 Gy to this region and poorer survival outcomes among a group of 1101 patients with NSCLC [69]. They suggested that "the sparing of specific sub-structures in the base of the heart could lead to significant improvements in survival in lung cancer patients." [69]. Considering that the dose to the left atrium, pulmonic valve, and LMCA was considerably higher (22.9 Gy, 18.8 Gy, 19.4 Gy, respectively) than this value, it strongly indicates the need for dose reduction in the planning process. McWilliam et al. also used similar methods to analyse the results of RTOG0617 [27, 1]. Similarly, their findings indicated that the radiation dose to the base of the heart was correlated with OS. They identified this region to be anatomically where the LMCA, and the SAN are located. This partly correlates with this project, where the LMCA was found to receive much higher mean dose than the heart, but also difficult to contour. Their study had the advantage of not outlining specific structures, as this project have found that the LMCA is difficult to identify, especially using 4D-AVE-CT.

Niedzielski et al. found the left atrium as the substructure within the heart that received the highest dose [35], like in this project. In their study they also found that both atria received significantly higher dose the the heart, while the right atrium received significantly less in this project. Thor et al. developed a predictive model for OS and achieved excellent performance by incorporating D45%[Gy] to the atria, among other factors [32]. Although this metric was not utilized in this specific phase of the project, it holds potential for further investigation, as earlier parts of the project demonstrated its beneficial value. Wang et al. found that left atrium V30Gy dose was correlated to both pericardial and arrhythmic events of the heart [70]. Although this metric was not employed in this particular analysis, it presents an intriguing area for future research.

The discovery of a higher than expected dose delivered to the left atrium holds potential clinical significance. Cella et al., as mentioned in section 2.6.2, found that doses between 25 and 30 Gy to a large volume of the left atrium and ventricle to increase the chances of developing radiation induced mitral or aortic valvular disease. From Appendix C.4 one can see that the left atrium had a median value V15 of 32.7%, and V30 of 13.3%. Although it is not a substantial volume, it should not be overlooked or disregarded.

Despite the fact that there is less research directly linking radiation induceed heart diseases to the atria compared to the ventricles, explained in section 2.6.2, it is important to consider the dose to the atria, specifically the left atrium, as it may be relevant to other diseases and substructures. Due to its larger size and proximity to other smaller structures such as the coronary arteries, valves, and parts of the electrical conduction system, the dose to the left atrium could potentially serve as an indicator of the dose received by these smaller structures within the heart. Considering the poor overlap observed in smaller structures, a potential approach for treatment planning could involve using a larger volume to represent the area of the heart where these structures are located, rather than focusing on their precise localization. This method, which would be less time-consuming, could be implemented with AVE-4D-CT scans, as there would be less requirements for accuracy.

The structures with significant change and smaller median Dmean dose were the right atrium and ventricle, the left ventricle, the tricuspid valve, the mitral valve, the right coronary artery, inferior vena cava and the AVN. These all lies on the right side or towards the apex of the heart, as illustrated in Figure 4.24. This implies that the heart's dosage is not uniformly distributed, and the mean dose to the heart underestimates the dosage to the upper left region of the heart. This also illustrates the potential to decrease the dose by using proton beam planning.

Proton Planning

Mean dose to the heart is less sufficient as surrogate parameter for proton beam planning, with greater relative difference between the heart dose and the dose to the structures. On the other hand the doses are all lower, so a larger change is not of as much concern. Also, there are less structures with significant change and higher median dose to the structure than to the heart. The structures with these significant changes were the left atrium,, the aorta, the pulmonary artery, the superior vena cava and the pericardium, the same structures as for photon, without the pulmonic valve and LMCA. The pulmonic valve is actually shown to have a lower median than the heart and significant change between the two. The LMCA does not show significant difference from the heart in proton beam planning.

Especially the left atrium is of concern here, as it receives more dose than expected by just using the heart mean dose as a parameter for the whole heart. Even though the

dose is lower than for photon beam planning, one want to know that the proton beam planning is true to nature. Also here the three largest great vessels on the top of the heart are of interest with a larger dose than the heart. A similar pattern can be observed in the study conducted by Ferris et al. The mean Dmean values with IMPT plans for Ferris et al. and this project were as follows: for the heart, 5.91 and 1.82 Gy; for the left atrium, 9.83 and 6.08 Gy; for the aorta, (ascending) 9.16 and 20.08 Gy; for the pulmonary artery, 27.33 and 26.99 Gy; and for the superior vena cava, 24.42 and 27.81 Gy. It can be observed that the doses were higher for the mentioned substructures compared to the heart, although the same test was not performed by Ferris et al., as they had a different objective. The dose to the heart differed between these studies, which could potentially explain some of the differences in the substructures. In general, Ferris et al. observed higher mean Dmean doses to the other coherent substructures with this project compared to the median Dmean in this project [72].

5.3 Methodology

Literature Search

The literature search was performed by the candidate who initially had little knowledge of the field. Several articles were interconnected, directing the candidate towards specific articles, potentially excluding other articles. All of the found structures were included in this project, creating a time consuming project. By reducing the number of structures included, the candidate could dedicate more time to accommodate additional patients. At the same time the structures showed various results, and many structures could be seen at the same time, and the candidate could get a full perspective, with little missing volume. From the literature search some parts outside of the heart, but part of the cardiovascular system, was included. These were interesting to study as they are linked to the heart, and also as they are closely related with the amount of radiation the blood gets.

Extended Literature Search

The literature search performed to select dose metrics was very specific, and only a few articles were selected to use. Another search might find other metrics to use, and find different results. For some structures there was not found specific dose metrics used in literature, and their performance may differ when evaluated with other metrics than used in this project. The chosen metrics worked well for this project, considering the

time and scope limitations, which prevented the inclusion of a large number of metrics.

Contouring

Initially there were only 15 proton simulation plans available to the candidate, which reduced the number of patients included in this project. Preferably there would be more patients included to get a better view of the structures and to be more certain of the statistical significance. As only nine of the 15 patient had contrast images this reduced the significance of analysis of the structures drawn in these scans.

Upon contouring, certain uncertainties were discovered. It would have been preferable to divide the aorta into two segments: the ascending aorta, which is linked to the heart, and the descending aorta, which transports blood to the remaining parts of the body. This division would make it easier to determine precisely where the dose was administered and would eliminate any problems that may arise when a single structure appears in two separate locations in a CT scan simultaneously, making comparisons difficult.

This project encountered various uncertainties when it came to contouring. Using different atlases presents an uncertainty. The main atlas used, by Duane et al., used non-contrast rapid CT scans, unlike the scans used in this project, creating an uncertainty [59]. Selection bias also presents an uncertainty in the contouring of this project, that the candidate may have changed technique during contouring the different patients and scans. This can be the reason that the candidate found a difference in the drawings of the left atria in the different scans. The QA was performed by the candidate, and the project would likely benefit from an external QA. This QA approach focused more on ensuring the consistency of contouring across different scans rather than on the accuracy of the contouring. Simultaneously, this QA process was purposeful and effective within the limitations of this particular project.

5.4 Future Work

There are several potential improvements that could be implemented in similar projects to increase the reliability of the results. One approach would involve expanding the inclusion of patients and possibly incorporating CT scans from the third week of treatment. By increasing the sample size and including additional scans, a more comprehen-

sive analysis can be conducted. Additionally, the various scans for each patient could be individually analyzed by including and contouring only one. In the current study, IMRT and IMPT plans are utilized and compared. It would be intriguing to explore the effects of other radiation techniques on dose distribution to the anatomical structures.

Another interesting project idea would involve dose planning, where specific dose constraints are established for one or more structures, and new treatment plans are created accordingly. For instance, investigating the dose constraints for the left atrium, which may provide more robust results than the mean heart dose, could be interesting to study.

Further exploration of the findings regarding the significant radiation received by the great vessels and its correlation with blood volume radiation would also be of interest. Analyzing the anatomy of these vessels and exploring different segmentation techniques to assess region-specific radiation effects could give valuable insights.

To study the structures further, the utilization or development of auto-segmentation algorithms should be considered. These algorithms can save time by automating the contouring process, allowing for the inclusion of more patients and diverse treatment plans, without relying solely on manual contouring methods.

Chapter 6

Conclusions

In this project, numerous substructures of the heart and cardiovascular system were delineated, with varying extent of literature linking them to RIHD. The structures demonstrated variations in their characteristics, effectively illustrating differences in both geometric and dosimetric analyses. The study revealed that both anatomical changes over time and contouring inconsistency including breathing motion uncertainties contribute to varying alterations. The latter introduces greater uncertainty in the volume of substructures, while the overlap and spatial relationship between structures remain relatively consistent when comparing all scans. Larger volumes (> 10 cc) exhibited best overlap, suggesting their potential suitability for further utilization.

Certain substructures, all located in the superior region of the heart, namely the LAD, left atrium, mitral valve, AVN, and right atrium, exhibited significant differences in actual dose compared to the planned dose in photon beam planning. In RT, these structures received a higher mean dose than what was initially calculated during the planning phase. In contrast, proton beam planning displayed more robustness in this regard, with only one structure with significant change, the superior vena cava, receiving a lower dose than originally planned. In comparison to photon beam planning, proton beam planning resulted in significantly lower doses across all structures, indicating that proton beam treatment has the potential to minimize radiation exposure to all regions of the heart and all selected structures within the cardiovascular system used in this project.

In both photon and proton beam planning, certain structures, namely the left atrium, pericardium, and three of the great vessels (aorta, pulmonary artery, and superior vena cava), were discovered to receive a significantly higher dose than what was initially calculated to the heart. Additionally, in photon beam planning, the LMCA and pulmonic

valve were included among these structures. All of these structures are also situated in the superior region called the base of the heart. These findings indicate that the heart may not serve as an effective surrogate parameter for assessing the dose to these specific structures. Considering the observed reduction in dose to all structures in proton beam planning, it holds promise for lowering the radiation exposure to this specific region of the heart. This becomes particularly important as literature suggests that an elevated dose to these regions may potentially contribute to decreased overall survival in patients. Thus, the ability of proton beam planning to reduce the radiation dosage in this context becomes even more consequential.

In future studies, it would be advantageous to expand the patient cohort while narrowing down the selection of specific structures for focused investigation. This could focus on regions like the base of the heart, with the left atrium as a representative substructure, or the superior great vessels positioned above the heart. By increasing the sample size and concentrating on these specific structures, a more targeted and comprehensive understanding can be gained. Based on the findings of this project, it appears that employing AVE-4D-CT in contouring for larger substructures in the base of the heart or the cardiovascular system could prove advantageous and valuable in the radiation treatment planning of LA-NSCLC.

Appendix A

TNM Explanation

Table A.1: TNM classification of lung cancer, based on the UICC 8th edition from [11]

Tx		Primary tumor cannot be assessed
T0		No evidence of primary tumor
T1		Tumor 3 cm or less in greatest diameter
	T1a(mi)	Minimally invasive adenocarcinoma
	T1a	Tumor 1 cm or less
	T1b	Tumor more than 1 cm but not more than 2 cm
	T1c	Tumor more than 2 cm but not more than 3 cm
T2		Tumor more than 3 cm but not more than 5 cm; or tumor woth any of the following features: Involves main bronchus without involvement of the carina, or invades visceral pleura or associated with atelectasis or obstructive pneumonitis
	T2a	Tumor more than 3 cm but not more than 4 cm
	T2b	Tumor more than 4 cm but not more than 5 cm
T3		Tumor more than 5 cm but not more than 7 cm or directly invades: parietal pleura, chest wall, phrenic nerve, or parietal pericardium; or separate tumor nodule(s) in the same lobe
T4		Tumor more than 7 cm or of any size that invades any of the following: diaphragm, mediastinum, heart, great vessels, trachea, recurrent laryngeal nerve, oesophagus, vertebral body, carina; or separate tumor nodule(s) in a different ipsilateral lobe to the primary
N1		Peribronchial, ipsilateral hilar lymph node involvement
N2		Ipsilateral mediastinal
N3		Contralateral mediastinal, scalene or supraclavicular
M0		No distant metastasis
M1		Metastasis present

Appendix B

Python Code

B.1 volumesPreperation.py

Created by the candidate.

```
# -*- coding: utf-8 -*-
"""
Created on Fri Mar 24 15:33:47 2023

@author: linfra
"""
import pandas as pd
import numpy as np

structureNames = ['heart', 'tricuspidalvalve', 'superiorvenacava','rightventricle', 'rightcoronararte', 'rightatrium', 'pulmonicvalve', 'pulmonaryartery', 'pericard', 'nodesinus', 'nodeav', 'mitralvalve', 'leftventricle', 'leftmaincoartery', 'leftcircumflex', 'leftatrium', 'leftantdescarter', 'inferiorvenacava', 'aorticvalve', 'aorta']
structureNames_c = []
for structureName in structureNames:
    structureNames_c.append(f'{structureName}+k')

df = pd.read_csv("dvhValuesx_cleaned_new.csv", sep=';', decimal=',')


# sets up empty dataframes:
column_names = ["Patient", 'Plan', "Comparison", "Structure", "Volume"]
df_plan = pd.DataFrame(columns=column_names)
df_contrast = pd.DataFrame(columns=column_names)
df_w1 = pd.DataFrame(columns=column_names)

df['Structure'] = df['Structure'].apply(str.lower)
```

```
26
27 for index,row in df.iterrows():
28     if row['Structure'] in structureNames:
29         if row['Plan'] == 'FB':
30             new_row = {'Patient': row['Patient'], 'Plan': row['Plan'],
    'Comparison': 'Plan',  'Structure': row['Structure'], 'Volume': row[
    'Volume']}
31             df_plan = pd.concat([df_plan, pd.DataFrame([new_row])],
    axis=0, ignore_index=True)
32
33         elif row['Plan'] == 'FB_w1':
34             new_row = {'Patient': row['Patient'], 'Plan': row['Plan'],
    'Comparison': 'Week 1',  'Structure': row['Structure'], 'Volume':
    row['Volume']}
35             df_w1 = pd.concat([df_w1, pd.DataFrame([new_row])], axis=0,
     ignore_index=True)
36
37     elif row['Structure'] in structureNames_c:
38         new_row = {'Patient': row['Patient'], 'Plan': row['Plan'], '
    Comparison': 'Contrast',  'Structure': row['Structure'][:-2], '
    Volume': row['Volume']}
39         df_contrast = pd.concat([df_contrast, pd.DataFrame([new_row])],
     axis=0, ignore_index=True)
40
41 df_plan = df_plan.drop('Plan', axis = 1)
42 df_w1 = df_w1.drop('Plan', axis = 1)
43 df_contrast = df_contrast.drop('Plan', axis = 1)
44
45 # turn tables around to useful format
46 df_comp_c_plan_w1 = pd.concat([df_plan, df_contrast, df_w1])
47 df_comp_c_plan_w1 = df_comp_c_plan_w1.pivot_table(values='Volume',
    index=['Structure', 'Patient'], columns='Comparison', aggfunc='first
    ')
48 df_comp_c_plan_w1.to_csv("CompareVolumePlanAndContrastAndWeek1.csv",
    sep=";", decimal=",", na_rep = np.nan)
```

B.2 compareContoursGeometrically.py

Created by Helge Egil Seime Pettersen, modified by the candidate.

```
1 import matplotlib.pyplot as plt
2 import os
3 import numpy as np
4 from classes import Images, Structures
5 import pandas as pd
6 import seg_metrics.seg_metrics as sg
```

```
from tqdm import tqdm
import matplotlib.patches as mpatches

patientNumbers = ['4','7','8','12','16','17']


for patientNumber in patientNumbers:

    print('Processing patient number:', patientNumber)

    images = Images(patientNumber)

    ww = 400
    wl = 50

    plt.figure(figsize=(8,8))

    # naming folders for different images:
    hiddenVendorNames = ['A','B','C']
    vendorNames = ["Contrast", "Week 1 3D", "Week 1 6D"]

    hiddenVendorNamesDict = {vendorNames[k] : hiddenVendorNames[k] for k in range(len(vendorNames))}

    structuresHUS = Structures(patientNumber, "GroundTruth")


    with open(f"{patientNumber}/Output/namingKey.txt",'w') as keyFile:
        for vendorName, hiddenVendorName in hiddenVendorNamesDict.items():
            keyFile.write(f"{hiddenVendorName}: {vendorName}\n")


    # choosing structures and colors for drawings
    structureNames = ['heart','tricuspidalvalve', 'rightventricle', 'rightcoronararte', 'rightatrium', 'pulmonicvalve', 'pulmonaryartery', 'pericard', 'nodesinus', 'nodeav', 'mitralvalve', 'leftventricle', 'leftmaincoartery', 'leftcircumflex', 'leftatrium', 'leftantdescarter', 'inferiorvenacava', 'aorticvalve', 'aorta', 'superiorvenacava']
    colors = {'heart':'khaki','tricuspidalvalve': 'springgreen', 'superiorvenacava':'blue', 'rightventricle':'teal', 'rightcoronararte':'palegreen', 'rightatrium':'blueviolet', 'pulmonicvalve':'violet', 'pulmonaryartery':'lime', 'pericard':'magenta', 'nodesinus':'tan', 'nodeav':'slateblue', 'mitralvalve':'blanchedalmond', 'leftventricle':'yellow', 'leftmaincoartery':'orange', 'leftcircumflex':'cyan', 'leftatrium':'forestgreen', 'leftantdescarter':'salmon', '
```

```
    inferiorvenacava':'darkorange', 'aorticvalve':'deepskyblue', 'aorta'
    :'saddlebrown'}
41
42      column_names = ["Patient", "Slice number", "Structure", "Comparison
    ", "DICE", "HD", "HD95", "MSD", "VS"]
43      df = pd.DataFrame(columns=column_names)
44
45      original = "Plan AIP"
46
47
48      for structureName in structureNames:
49          print(f"Processing {structureName}...")
50
51          file = -1
52          # makes a lopp that goes through the extra structures for
    comparison
53          extraStructureNames = [f"{structureName}+k", f"{structureName
    }1.3D", f"{structureName}1.6D"]
54
55          for extraStructureName in extraStructureNames:
56
57              structuresHUS.makeIndexForStructureName(structureName)
58              structuresHUS.makeIndexForStructureName(extraStructureName)
59
60              # use only images refered to in both structure sets (
    intersection)
61              UIDs1 = set(structuresHUS.getListOfUIDs(structureName))
62              UIDs2 = set(structuresHUS.getListOfUIDs(extraStructureName)
    )
63              UIDs = UIDs1.intersection(UIDs2)
64
65              # increases for each extra structure, to save in seperate
    files, and add correct name to the column in the cvs file
66              file += 1
67              hiddenVendorName = hiddenVendorNames[file]
68              vendorName = vendorNames[file]
69              print(original, 'compared with:', vendorName)
70
71              for thisUID in tqdm(UIDs):
72                  thisDs = images.loadDicomNoImage(thisUID)
73                  filenum = thisDs.InstanceNumber
74
75                  thisImg = images.loadImage(thisUID)
76                  plt.clf()
77                  plt.imshow(thisImg, cmap="gray", vmin=wl-ww/2, vmax=wl+
    ww/2)
78
```

```
79                contoursHUS, masksHUS = structuresHUS.
   loadStructurePolygonAndMask(structureName, thisUID, thisDs)
80
81
82                maskHUS = masksHUS[0]
83                if len(masksHUS) > 1:
84                    for idx, moreMaskHUS in enumerate(masksHUS[1:]):
85                        maskHUS = np.logical_xor(moreMaskHUS, maskHUS)
86
87                for idx, contourHUS in enumerate(contoursHUS):
88                    label = "HUS"
89                    if idx > 0:
90                        label=None
91                    plt.plot(*contourHUS, color=colors[structureName],
   linestyle="solid", label=f"{original}")
92
93                contoursVendor, masksVendor = structuresHUS.
   loadStructurePolygonAndMask(extraStructureName, thisUID, thisDs)
94
95                maskVendor = masksVendor[0]
96                if len(masksVendor) > 1:
97                     for moreMaskVendor in masksVendor[1:]:
98                         maskVendor = np.logical_xor(maskVendor,
   moreMaskVendor)
99
100               metrics = sg.write_metrics(labels=[1], gdth_img=maskHUS
   , pred_img=maskVendor, csv_file=None,
101                                          spacing=thisDs.PixelSpacing
   , metrics=['dice','hd','hd95','msd','vs'], verbose=False)
102
103               positive_difference = np.fliplr(np.rot90(np.where(
   maskHUS > maskVendor, 1, 0), k=3))
104               negative_difference = np.fliplr(np.rot90(np.where(
   maskHUS < maskVendor, 1, 0), k=3))
105
106               DICE_sg = round(metrics[0]['dice'][0], 3)
107               HD95_sg = round(metrics[0]['hd95'][0], 2)
108               MSD_sg = round(metrics[0]['msd'][0],2)
109               #added metrics:
110               VS_sg = round(metrics[0]['vs'][0],2)
111               HD_sg = round(metrics[0]['hd'][0],2)
112
113               for idx, contourVendor in enumerate(contoursVendor):
114                    label = f"{vendorName} (DICE {DICE_sg:.3f}; HD95 {
   HD95_sg:.2f} mm)"
115                    if idx > 0:
116                        label=None
```

```
                    plt.plot(*contourVendor, color=colors[
    structureName], linestyle="dashed", label=label)

                plt.imshow(positive_difference, label="False Negative",
     cmap="Wistia", alpha=0.3*(positive_difference>0))
                plt.imshow(negative_difference, label="False Positive",
     cmap="spring", alpha=0.3*(negative_difference>0))

                new_row = {"Patient": patientNumber,"Slice number":
    filenum, "Structure": structureName, "Comparison": vendorName, "DICE
    ": DICE_sg, "HD" :HD_sg, "HD95": HD95_sg, "MSD":MSD_sg, "VS":VS_sg}
                df = pd.concat([df, pd.DataFrame([new_row])], axis=0,
    ignore_index=True)

                orange_patch = mpatches.Patch(color="orange", label=f"{
    original} not {vendorName}")
                yellow_patch = mpatches.Patch(color="yellow", label=f"{
    vendorName} not {original}")

                plt.title(f"{structureName}")
                l1 = plt.legend(loc=1)
                plt.legend(handles=[orange_patch, yellow_patch], loc=2)
                plt.gca().add_artist(l1)
                plt.tight_layout()
                plt.axis('off')

                path = f"{patientNumber}/Output/{hiddenVendorName}/{
    structureName}"
                if not os.path.exists(path):
                    os.makedirs(path)
                plt.savefig(f"{path}/{filenum}.png")

     df = df.sort_values(["Structure", "Comparison", "Slice number"])
     df.to_csv(f"{patientNumber}/Output/indices{patientNumber}.csv", sep
    =";", decimal=",")

     plt.figure()

print('Program done')
```

B.3 classes.py

Created by Helge Egil Seime Pettersen.

```

import numpy as np
```

```
import pydicom
from skimage.draw import polygon
import matplotlib.pyplot as plt
import glob

def findDICE(a,b):
    return np.sum(b[a==1])*2 / (np.sum(a) + np.sum(b))

class Images:
    def __init__(self, folder):
        self.folder = folder
        self.fileList = None
        # self.SOPInstanceUIDDict = dict()

        self.makeFileList()
        self.sortImagesAndMakeIndex()

    def makeFileList(self):
        self.fileList = glob.glob(f"{self.folder}/Images/*.dcm")

    def sortImagesAndMakeIndex(self):
        unsortedFileList = self.fileList

        sortingDict = dict()
        sortingDictSOP = dict()


        for file in unsortedFileList:
            ds = pydicom.dcmread(file, stop_before_pixels=True)
            sortingDict[ds.InstanceNumber] = file
            sortingDictSOP[ds.InstanceNumber] = ds.SOPInstanceUID
            #self.SOPInstanceUIDDict[ds.SOPInstanceUID] = file

        sortedKeys = sorted(list(sortingDict.keys()))
        sortedFileList = [ sortingDict[key] for key in sortedKeys ]


        self.SOPInstanceUIDDict = { sortingDictSOP[key] : sortingDict[
    key] for key in sortedKeys}
        self.SOPInstanceUIDList =  [ sortingDictSOP[key] for key in
    sortedKeys ]

        self.fileList = sortedFileList

    def getFileList(self):
        print(self.fileList)
        return self.fileList
```

```
48
49      def getUIDList(self):
50          return list(self.SOPInstanceUIDList)
51
52      def loadDicom(self, SOPInstanceUID):
53
54          filename = self.SOPInstanceUIDDict[SOPInstanceUID]
55          ds = pydicom.dcmread(filename)
56          return ds
57
58      def loadDicomNoImage(self, SOPInstanceUID):
59          filename = self.SOPInstanceUIDDict[SOPInstanceUID]
60          ds = pydicom.dcmread(filename, stop_before_pixels=True)
61          return ds
62
63      def loadImage(self, SOPInstanceUID):
64          ds = self.loadDicom(SOPInstanceUID)
65          img = ds.pixel_array * ds.RescaleSlope + ds.RescaleIntercept
66          assert img.shape == (512, 512)
67          return img
68
69  class Structures:
70      def __init__(self, folder, structureOrigin):
71          self.folder = folder
72          self.structureOrigin = structureOrigin
73          self.ROIDict = dict()
74          self.ROIIdxDict = dict()
75          self.SOPInstanceUIDForStructureDict = dict()
76          self.file = None
77
78          self.loadFile()
79          self.findROINumbers()
80
81      def loadFile(self):
82          self.files = glob.glob(f"{self.folder}/Structures/{self.
    structureOrigin}/*.dcm")
83          self.rsDict = { file : pydicom.dcmread(file) for file in self.
    files }
84
85      def getVendorName(self, rsFilename = None):
86          if not rsFilename:
87              rsFilename = list(self.rsDict.keys())[0]
88
89          #vendorName = #rsFilename.split(".")[-2].split(" ")[0]
90          vendorName = rsFilename.split(".")[0]
91
92          return vendorName
```

```
93
94      def getRsFilenames(self):
95          return list(self.rsDict.keys())
96
97      def findROINumbers(self):
98          for rsFilename, rs in self.rsDict.items():
99              self.ROIDict[rsFilename] = dict()
100             self.ROIIdxDict[rsFilename] = dict()
101             for ROI in rs.StructureSetROISequence:
102                 name = ROI.ROIName.lower()
103                 number = ROI.ROINumber
104
105                 if name == "bag_bowel":
106                     name = "bowelbag"
107
108                 if not "ptv" in name and not "ctv" in name:
109                     self.ROIDict[rsFilename][name] = number
110
111             nameNumber = list()
112             print(f"Found the following ROIs in the {self.folder} / {
    self.structureOrigin} dataset: ")
113             for name, number in self.ROIDict[rsFilename].items():
114                 nameNumber.append(f"{name}")
115             print(", ".join(nameNumber), end=".\n\n")
116
117     def makeIndexForStructureName(self, structureName):
118         for rsFilename, rs in self.rsDict.items():
119             if not rsFilename in self.SOPInstanceUIDForStructureDict:
120                 self.SOPInstanceUIDForStructureDict[rsFilename] = dict
    ()
121             self.SOPInstanceUIDForStructureDict[rsFilename][
    structureName] = list()
122             number = self.ROIDict[rsFilename][structureName.lower()]
123
124             for idx, ROI in enumerate(rs.ROIContourSequence):
125                 if ROI.ReferencedROINumber == number:
126                     self.ROIIdxDict[rsFilename][structureName.lower()]
    = idx
127                     for cseq in ROI.ContourSequence:
128                         assert len(cseq.ContourImageSequence) == 1
129
130                         for ciseq in cseq.ContourImageSequence:
131                             UID = ciseq.ReferencedSOPInstanceUID
132                             self.SOPInstanceUIDForStructureDict[
    rsFilename][structureName].append(UID)
133
134     def getListOfUIDs(self, structureName, rsFilename = None):
```

```
135         if not rsFilename:
136             rsFilename = list(self.rsDict.keys())[0]
137 
138         return self.SOPInstanceUIDForStructureDict[rsFilename][
    structureName]
139 
140     def getListOfIdxSeq(self, rsFilename, SOPInstanceUID, structureName
    ):
141         idxSeqs = list()
142 
143         for idx, uid in enumerate(self.SOPInstanceUIDForStructureDict[
    rsFilename][structureName]):
144             if uid == SOPInstanceUID:
145                 idxSeqs.append(idx)
146 
147         return idxSeqs
148 
149     def loadStructurePolygonAndMask(self, structureName, SOPInstanceUID
    , ds, rsFilename = None):
150         if not rsFilename:
151             rsFilename = list(self.rsDict.keys())[0]
152 
153         rs = self.rsDict[rsFilename]
154         x0, y0 = ds.ImagePositionPatient[0:2]
155         ps = ds.PixelSpacing[0]
156         #mask = np.zeros([ds.pixel_array.shape[0], ds.pixel_array.shape
    [1]])
157 
158         # Might be more than one idxSeq
159         idxSeqs = self.getListOfIdxSeq(rsFilename, SOPInstanceUID,
    structureName)
160         idxROI = self.ROIIdxDict[rsFilename][structureName.lower()]
161 
162         contours = list()
163         masks = list()
164 
165         for idxSeq in idxSeqs:
166             mask = np.zeros([512, 512])
167 
168             contourRaw = rs.ROIContourSequence[idxROI].ContourSequence[
    idxSeq].ContourData
169             contour = np.reshape(contourRaw, (len(contourRaw) // 3, 3))
170 
171             contour_x = (contour[:, 0] - x0) / ps
172             contour_y = (contour[:, 1] - y0) / ps
173             contours.append([contour_x, contour_y])
174 
```

```
175             r, c = polygon(contour_x, contour_y, mask.shape)
176             mask[r,c] = 1
177             masks.append(mask)
178 
179         return contours, masks
```

B.4 createFilesAllMetrics.py

Created by the candidate.

```
1  import pandas as pd
2  import numpy as np
3  from scipy import stats
4  
5  
6  patientNumbers_c = [1,3,4,7,8,11,12,16,17]
7  # patientNumbers_wc = ['2','5','6','13','14','15']
8  structureNames = ['heart','tricuspidalvalve','superiorvenacava', '
       rightventricle', 'rightcoronararte', 'rightatrium', 'pulmonicvalve',
        'pulmonaryartery', 'pericard', 'nodesinus', 'nodeav', 'mitralvalve'
       , 'leftventricle', 'leftmaincoartery', 'leftcircumflex', 'leftatrium
       ', 'leftantdescarter', 'inferiorvenacava', 'aorticvalve', 'aorta']
9  comparisonNames = ["Contrast", "Week 1"]
10 
11 column_names = ["Patient", "Slice number", "Structure", "Comparison", "
       DICE", "HD95", "MSD", "VS", 'HD']
12 df = pd.DataFrame(columns=column_names)
13 
14 done = ['1','2','3','4','5','6','7','8','11','12','13','14','15','16','
       17']
15 
16 # only takes with 3D for patient 1,m that is missing 6D
17 for patientNumberDf in done:
18     if patientNumberDf != '1':
19         patientNumberDf = pd.read_csv(f"{patientNumberDf}/Output/
       indices{patientNumberDf}.csv", sep = ';', decimal = ',')
20         patientNumberDf = patientNumberDf[patientNumberDf.Comparison !=
        'Week 1 3D']
21         df = pd.concat([df, patientNumberDf], axis=0, ignore_index=True
       )
22     else:
23         patientNumberDf = pd.read_csv(f"{patientNumberDf}/Output/
       indices{patientNumberDf}.csv", sep = ';', decimal = ',')
24         df = pd.concat([df, patientNumberDf], axis=0, ignore_index=True
       )
25 
```

```
# replaces column name for Week 1, so that they have the same value, even though they had different transfers
df = df.drop(df.columns[-1], axis = 1)
df = df.replace('Week 1 3D', 'Week 1')
df = df.replace('Week 1 6D', 'Week 1')

#removes outliers, by computing z-score
df = df[(np.abs(stats.zscore(df['HD95'])) < 3)]

df.to_csv("DataFrames/FULLcombindedDF.csv", sep=";", decimal=",")
```

B.5 meanStructuresGeometrically.py

Created by the candidate.

```

import pandas as pd
import numpy as np

df = pd.read_csv('FULLcombindedDF.csv', sep=';', decimal=',')

# combine by structure: to calculate mean D and H
df_mean2 = df.groupby(['Structure', 'Comparison'], as_index = False).aggregate({'DICE':'mean', 'HD95':'mean'})
df_mean3 = df.groupby(['Structure', 'Comparison'], as_index = False).aggregate({'DICE':np.std, 'HD95':np.std})
df_mean3 = df_mean3.rename(columns = {'DICE':'Dstd', 'HD95':'Hstd'})
df_mean4 = pd.concat([df_mean2, df_mean3[['Dstd', 'Hstd']]], axis = 1)

df_mean4.to_csv("Filer/Compare.D-H.Cplan.Aw1.Aplan.csv", sep=";", decimal=",")

df_write = df_mean4.pivot_table(values=['DICE', 'HD95', 'Dstd', 'Hstd'], index=['Structure'], columns='Comparison', aggfunc='first')
df_write.columns = df_write.columns.to_flat_index()
df_write.to_csv("Filer/Compare.D-H.Cplan.Aw1.AplanSTD.csv", sep=";", decimal=",")

# combine by structure and patient: mean d and H
df_mean5 = df.groupby(['Structure', 'Comparison', 'Patient'], as_index = False).aggregate({'DICE':'mean', 'HD95':'mean'})
df_mean5_std = df.groupby(['Structure', 'Comparison', 'Patient'], as_index = False).aggregate({'DICE':np.std, 'HD95':np.std})
df_mean5_std = df_mean5_std.rename(columns = {'DICE':'Dstd', 'HD95':'Hstd'})
```

```
df_mean5_std = pd.concat([df_mean5, df_mean5_std[['Dstd', 'Hstd']]], axis = 1)

df_mean5_std = df_mean5_std.pivot_table(values=['DICE', 'HD95', 'Dstd', 'Hstd'], index=['Structure', 'Patient'], columns='Comparison', aggfunc='first')
df_mean5_std.columns = df_mean5_std.columns.to_flat_index()
df_mean5_std = df_mean5_std.rename(columns = {('DICE', 'Contrast'):'D.Cplan', ('DICE', 'Week 1'):'DAw1', ('HD95', 'Contrast'):'HCplan', ('HD95', 'Week 1'):'HAw1'})
df_mean5_std = df_mean5_std.rename(columns = {('Dstd', 'Contrast'):'DstdCplan', ('Dstd', 'Week 1'):'DstdAw1', ('Hstd', 'Contrast'):'HstdCplan', ('Hstd', 'Week 1'):'HstdAw1'})

df_mean5_std.to_csv("Filer/Compare.D-H.Cplan.Aw1.Aplan.Patients.csv", sep=";", decimal=",")

df_mean6 = df_mean5.pivot_table(values=['DICE', 'HD95'], index=['Structure', 'Patient'], columns='Comparison', aggfunc='first')
df_mean6.columns = df_mean6.columns.to_flat_index()
df_mean6 = df_mean6.rename(columns  = {('DICE', 'Contrast'):'DCplan', ('DICE', 'Week 1'):'DAw1', ('HD95', 'Contrast'):'HCplan', ('HD95', 'Week 1'):'HAw1'})

# including volume:

df_v = pd.read_csv('Filer/CompareVolumePlanAndContrastAndWeek1.csv', sep=';', decimal=',', index_col = ('Structure', 'Patient'))
df_v = df_v.rename(columns = {'Contrast':'VCplan', 'Plan': 'VAplan', 'Week 1': 'VAw1'})


df_mean7 = pd.concat([df_mean6, df_v], axis =1)

df_mean7.to_csv("Filer/CompareV-D-H.Cplan.Aw1.Aplan.csv", sep=";", decimal=",")
```

B.6 DVHforStatistics.py

```
    import pandas as pd

# reads in the file
df = pd.read_csv("dvhValues5-65.csv", sep=';', decimal=',')
# renames the columns for V5Gy to be sorted correctly later
df = df.rename(columns = {'V5Gy':'V05Gy'})
```

```
7
8  column_names = df.columns.values.tolist()
9  values_names = column_names[5:]
10
11 # changes rows to columns
12 df_test = df.pivot_table(values=values_names, index=['Structure', 'Name
       '], columns='Plan', aggfunc='first')
13 df_test.columns = df_test.columns.to_flat_index()
14
15 df_test.to_csv("DVHvaluesPivot.csv", sep=";", decimal=",")
```

B.7 calculateMedianIQR-forStatistics.py

```
1  # -*- coding: utf-8 -*-
2  """
3  Created on Thu May  4 16:30:54 2023
4
5  @author: linfra
6  """
7
8  import pandas as pd
9  import numpy as np
10
11 # photon:
12 df_photon = pd.read_csv("dvhValues2104.csv", sep=';', decimal=',')
13 df_photon = df_photon.drop(['V30%', 'Unnamed: 0', 'Cohort', '
       ECLIPSEMinDose [Gy]', 'ECLIPSEVolume [cc]'], axis=1)
14
15 column_names = df_photon.columns.values.tolist()
16 values_names = column_names[3:]
17 # changes rows to columns
18 df_pivot_photon = df_photon.pivot_table(values=values_names, index=['
       Name', 'Structure'], columns='Plan', aggfunc='first')
19 df_pivot_photon.columns = df_pivot_photon.columns.to_flat_index()
20 df_pivot_photon['Beam'] = 'Photon'
21 df_pivot_photon.to_csv("export/PhotonDVH-plans-in-separate-columns.csv"
       , sep=";", decimal=",")
22
23 #proton:
24 df_proton = pd.read_csv("dvhValuesRaystation.csv", sep=';', decimal=','
       ,  encoding='cp1252')
25 df_proton = df_proton.drop(['Unnamed: 0', 'Cohort', 'ECLIPSEMinDose [Gy
       ]', 'ECLIPSEMeanDose [Gy]', 'ECLIPSEMaxDose [Gy]',
26                             'ECLIPSEVolume [cc]'], axis=1)
```

```
df_proton['Plan'] = df_proton['Plan'].replace({'autoFB(AIP_plan)':'FB', 'autoFB(AIP_uke1)':'FB_w1'})

column_names = df_proton.columns.values.tolist()
values_names = column_names[3:]
# sepeartes plans:
df_pivot_proton = df_proton.pivot_table(values=values_names, index=['Name', 'Structure'], columns='Plan', aggfunc='first')
df_pivot_proton.columns = df_pivot_proton.columns.to_flat_index()
df_pivot_proton['Beam'] = 'Proton'

#imports Dmean for proton from Raystation seperately
df_dmean_proton =  pd.read_csv("RaystationDmean.csv", sep=';', decimal=',', encoding= 'unicode_escape')
# removes empty columns
df_dmean_proton = df_dmean_proton[['Name', 'Structure', 'AplanDmean', 'CplanDmean', 'Aw1Dmean']]
df_dmean_proton['Beam'] = 'Proton'

# reimports photon pivot to have without index
df_photon_new = pd.read_csv("PhotonDVH-plans-in-separate-columns.csv", sep=';', decimal=',')
df_photon_new2 = df_photon_new.iloc[:,[6,7,-1]]
# concat
df_combine_photon_proton = pd.concat([df_dmean_proton, df_photon_new2], axis = 1)
df_combine_photon_proton = df_combine_photon_proton.drop(['Beam'], axis = 1)
df_combine_photon_proton.to_csv("export/Photon-Proton-DVH-plans-in-separate-columns.csv", sep=";", decimal=",")

#calculate difference (in percent) photon to proton
df_combine_photon_proton2 = df_combine_photon_proton.groupby(['Structure']).aggregate('median').reset_index()
df_combine_photon_proton2 = df_combine_photon_proton2.iloc[:,[0,2,5]]
df_combine_photon_proton2 = df_combine_photon_proton2.rename(columns = {'AplanDmean': 'ProtonDmean', "('ECLIPSEMeanDose [Gy]', 'FB')":'PhotonDmean'})
df_diff = pd.DataFrame(columns = ['Structure', 'PhotonDmean','ProtonDmean', 'Diff'])

for index, row in df_combine_photon_proton2.iterrows():
    photon = row['PhotonDmean']
    proton = row['ProtonDmean']
    diff = photon-proton
    diff_p = round(diff/photon *100,1)

```

```
62      new_row = {'Structure': row['Structure'], 'PhotonDmean': photon, '
    ProtonDmean': proton,'Diff': diff_p}
63      df_diff = pd.concat([df_diff, pd.DataFrame([new_row])], axis=0,
    ignore_index=True)
64
65 #seperate column for Dmean, separeted by Beam column value
66 df_dmean_proton_aplan = df_dmean_proton.iloc[:, [0,1,2,-1]]
67 df_photon_new_aplan = df_photon_new.iloc[:,[0,1,6,-1]]
68 df_photon_new_aplan = df_photon_new_aplan.rename(columns = {"('
    ECLIPSEMeanDose [Gy]', 'FB')":'AplanDmean'})
69
70 df_rows = pd.concat([df_dmean_proton_aplan, df_photon_new_aplan])
71 df_rows = df_rows.sort_values(['Structure', 'Name'])
72 df_rows.to_csv("export/Photon-Proton-DVH-plans-in-separate-rows.csv",
    sep=";", decimal=",")
73
74 # create Heart VS sub:
75 df_dmean_proton = df_dmean_proton.drop(['Beam'], axis = 1)
76 column_names = df_dmean_proton.columns.values.tolist()
77 # only Dmean
78 values_names = column_names[2]
79 df_pivot_proton_heart = df_dmean_proton.pivot_table(values=values_names
    , index=['Name'], columns=['Structure'], aggfunc='first')
80 df_pivot_proton_heart.to_csv("export/HeartVSSub-Proton-DVH-plans-in-
    separate-columns.csv", sep=";", decimal=",")
81
82 # calculate median and IQR for dmean proton:
83 df_dmean_proton_plan = df_dmean_proton.drop(['Name', 'CplanDmean', '
    Aw1Dmean'], axis =1)
84 median_dmean_proton = df_dmean_proton_plan.groupby(['Structure']).
    aggregate('median').reset_index()
85 df_iqr_proton_dmean = pd.DataFrame(columns=['Structure', '(q1 - q3)'])
86
87 for col in df_pivot_proton_heart:
88      q3 = round(np.quantile(df_pivot_proton_heart[col], 0.75), 2)
89      q1 = round(np.quantile(df_pivot_proton_heart[col], 0.25), 2)
90
91      new_row = {'Structure':col, '(q1 - q3)': f"({q1}-{q3})" }
92      df_iqr_proton_dmean = pd.concat([df_iqr_proton_dmean, pd.DataFrame
    ([new_row])], axis=0, ignore_index=True)
93
94 #change dmean to lot plan and w1 - one column
95 #split in two, concat to one column
96 df_dmean_proton_w1 = df_dmean_proton.drop(['Name', 'CplanDmean', '
    AplanDmean'], axis =1)
97 df_dmean_proton_w1['Plan'] = 'Aw1'
```

```
df_dmean_proton_w1 = df_dmean_proton_w1.rename(columns ={'Aw1Dmean':'Dmean'})
df_dmean_proton_plan['Plan'] = 'Aplan'
df_dmean_proton_plan = df_dmean_proton_plan.rename(columns ={'AplanDmean':'Dmean'})
df_dmean_box = pd.concat([df_dmean_proton_plan, df_dmean_proton_w1])
df_dmean_box.to_csv("export/Proton-DVH-plans-in-same-columns.csv", sep=";", decimal=",")

df_dmean_proton.set_index(['Name', 'Structure'], inplace=True)
df_proton_all = pd.concat([df_pivot_proton, df_dmean_proton], axis = 1)
df_proton_all = df_proton_all.drop(['Beam'], axis = 1)
df_proton_all.to_csv("export/Proton-DVH-plans-in-separate-columns.csv", sep=";", decimal=",")

#concat proton and photon, other than dmean
df_pivot_photon = df_pivot_photon.add_suffix('_photon')
df_pivot_proton = df_pivot_proton.add_suffix('_proton')
df_pivot_all = pd.concat([df_pivot_photon, df_pivot_proton], axis = 1)
df_pivot_all.to_csv("export/Proton-Photon-DVH-metrics-in-seperate-columns.csv", sep=";", decimal=",")
df_pivot_all_median = df_pivot_all.groupby(['Structure']).aggregate('median')


#calculate diff photon, precentage reduction
df_photon_new_aplan_heartvssub = df_photon_new_aplan.iloc[:,1:3]
df_photon_new_aplan_heartvssub = df_photon_new_aplan_heartvssub.groupby(['Structure']).aggregate('median').reset_index()
df_photon_new_aplan_heartvssub_diff = pd.DataFrame(columns=['Structure', 'Diff [Gy]', 'Diff [%]'])

for index, row in df_photon_new_aplan_heartvssub.iterrows():
    new = row['AplanDmean']
    heart = df_photon_new_aplan_heartvssub.iloc[2,1]
    diff = new - heart
    diff_p = round(diff/heart *100,1)

    new_row = {'Structure': row['Structure'], 'Diff [Gy]': diff, 'Diff [%]': diff_p}
    df_photon_new_aplan_heartvssub_diff = pd.concat([df_photon_new_aplan_heartvssub_diff, pd.DataFrame([new_row])], axis=0, ignore_index=True)

#for proton:
df_proton_new_aplan_heartvssub_diff = pd.DataFrame(columns=['Structure', 'Diff [Gy]', 'Diff [%]'])
```

```
for index, row in median_dmean_proton.iterrows():
    new = row['AplanDmean']
    heart = median_dmean_proton.iloc[2,1]
    diff = new - heart
    diff_p = round(diff/heart *100,1)

    new_row = {'Structure': row['Structure'], 'Diff [Gy]': diff, 'Diff [%]': diff_p}
    df_proton_new_aplan_heartvssub_diff = pd.concat([df_proton_new_aplan_heartvssub_diff, pd.DataFrame([new_row])], axis=0, ignore_index=True)

#calculate iqr for v15 and v30
df_iqr_proton_photon = pd.DataFrame(columns=['Metric','Structure', '(q1 - q3)'])
df_pivot_all = df_pivot_all.drop(columns = ['Beam_photon', 'Beam_proton'])


for col in df_pivot_all:
    df_pivot_all2 = pd.DataFrame(df_pivot_all[col])
    df_pivot_all2 = df_pivot_all2.pivot_table(values=col, index=['Name'], columns=['Structure'], aggfunc='first')
    for col2 in df_pivot_all2:
        q3 = round(np.quantile(df_pivot_all2[col2], 0.75), 2)
        q1 = round(np.quantile(df_pivot_all2[col2], 0.25), 2)

        new_row = {'Metric': col,'Structure':col2, '(q1 - q3)': f"({q1}-{q3})" }
        df_iqr_proton_photon = pd.concat([df_iqr_proton_photon, pd.DataFrame([new_row])], axis=0, ignore_index=True)
```

Appendix C

Statistical Tests and Descriptive Statistics

C.1 Volumes(V): A.plan and C.plan, A.plan and A.w1: Wilcoxon Signed Rank Test

Test Statistics[a]

Structure		Aplan - Cplan	Aplan - Aw1
aorta	Z	-1,836[b]	-1,647[b]
	Asymp. Sig. (2-tailed)	,066	,099
aorticvalve	Z	-2,549[b]	-2,045[b]
	Asymp. Sig. (2-tailed)	,011	,041
heart	Z	-2,666[c]	-1,136[c]
	Asymp. Sig. (2-tailed)	,008	,256
inferiorvenacava	Z	-,280[b]	-,653[b]
	Asymp. Sig. (2-tailed)	,779	,514
leftantdescarter	Z	-2,666[c]	-,629[c]
	Asymp. Sig. (2-tailed)	,008	,529
leftatrium	Z	-2,666[c]	-,909[c]
	Asymp. Sig. (2-tailed)	,008	,363
leftcircumflex	Z	-2,527[c]	-,315[b]
	Asymp. Sig. (2-tailed)	,012	,753
leftmaincoartery	Z	-,213[b]	-,711[b]
	Asymp. Sig. (2-tailed)	,832	,477
leftventricle	Z	-1,836[b]	-1,193[b]
	Asymp. Sig. (2-tailed)	,066	,233
mitralvalve	Z	-2,431[b]	-1,875[b]
	Asymp. Sig. (2-tailed)	,015	,061
nodeav	Z	-1,604[b]	-,816[c]
	Asymp. Sig. (2-tailed)	,109	,414
nodesinus	Z	-1,633[b]	-,577[c]
	Asymp. Sig. (2-tailed)	,102	,564
pericard	Z	-2,668[c]	-1,647[c]
	Asymp. Sig. (2-tailed)	,008	,100
pulmonaryartery	Z	-2,073[c]	-,454[b]
	Asymp. Sig. (2-tailed)	,038	,650
pulmonicvalve	Z	-1,364[c]	-,315[b]
	Asymp. Sig. (2-tailed)	,173	,753
rightatrium	Z	-,178[c]	-,341[c]
	Asymp. Sig. (2-tailed)	,859	,733
rightcoronararte	Z	-2,668[c]	-,399[b]
	Asymp. Sig. (2-tailed)	,008	,690
rightventricle	Z	-2,380[c]	-,937[c]
	Asymp. Sig. (2-tailed)	,017	,349
superiorvenacava	Z	-1,400[c]	-,653[b]
	Asymp. Sig. (2-tailed)	,161	,514
tricuspidalvalve	Z	-,296[c]	-,540[b]
	Asymp. Sig. (2-tailed)	,767	,589

a. Wilcoxon Signed Ranks Test

b. Based on negative ranks.

c. Based on positive ranks.

C.2 Dice(D): A.plan and C.plan, A.plan and A.w1: Wilcoxon Signed Rank Test

Test Statistics[a]

Structure		DAw1 - DCplan
aorta	Z	-1,481[b]
	Asymp. Sig. (2-tailed)	,139
aorticvalve	Z	-,420[c]
	Asymp. Sig. (2-tailed)	,674
heart	Z	-1,599[c]
	Asymp. Sig. (2-tailed)	,110
inferiorvenacava	Z	-,889[c]
	Asymp. Sig. (2-tailed)	,374
leftantdescarter	Z	-,533[c]
	Asymp. Sig. (2-tailed)	,594
leftatrium	Z	-,652[c]
	Asymp. Sig. (2-tailed)	,515
leftcircumflex	Z	-,533[b]
	Asymp. Sig. (2-tailed)	,594
leftmaincoartery	Z	-2,023[b]
	Asymp. Sig. (2-tailed)	,043
leftventricle	Z	-,178[b]
	Asymp. Sig. (2-tailed)	,859
mitralvalve	Z	-,415[c]
	Asymp. Sig. (2-tailed)	,678
nodeav	Z	-,280[b]
	Asymp. Sig. (2-tailed)	,779
nodesinus	Z	-,533[b]
	Asymp. Sig. (2-tailed)	,594
pericard	Z	-2,073[c]
	Asymp. Sig. (2-tailed)	,038
pulmonaryartery	Z	-1,007[b]
	Asymp. Sig. (2-tailed)	,314
pulmonicvalve	Z	-1,120[c]
	Asymp. Sig. (2-tailed)	,263
rightatrium	Z	-,889[b]
	Asymp. Sig. (2-tailed)	,374
rightcoronararte	Z	-,652[b]
	Asymp. Sig. (2-tailed)	,515
rightventricle	Z	-,178[c]
	Asymp. Sig. (2-tailed)	,859
superiorvenacava	Z	-1,599[c]
	Asymp. Sig. (2-tailed)	,110
tricuspidalvalve	Z	-1,955[b]
	Asymp. Sig. (2-tailed)	,051

a. Wilcoxon Signed Ranks Test

b. Based on negative ranks.

c. Based on positive ranks.

C.3 Hausdorff distance 95 percentile(H): A.plan and C.plan, A.plan and A.w1: Wilcoxon Signed Rank Test

Test Statistics[a]

Structure		HAw1 - HCplan
aorta	Z	-,770[b]
	Asymp. Sig. (2-tailed)	,441
aorticvalve	Z	-,140[b]
	Asymp. Sig. (2-tailed)	,889
heart	Z	-1,362[c]
	Asymp. Sig. (2-tailed)	,173
inferiorvenacava	Z	-,533[b]
	Asymp. Sig. (2-tailed)	,594
leftantdescarter	Z	-,178[c]
	Asymp. Sig. (2-tailed)	,859
leftatrium	Z	-,059[c]
	Asymp. Sig. (2-tailed)	,953
leftcircumflex	Z	-1,481[b]
	Asymp. Sig. (2-tailed)	,139
leftmaincoartery	Z	-1,183[b]
	Asymp. Sig. (2-tailed)	,237
leftventricle	Z	-,652[b]
	Asymp. Sig. (2-tailed)	,515
mitralvalve	Z	-,415[b]
	Asymp. Sig. (2-tailed)	,678
nodeav	Z	-,420[b]
	Asymp. Sig. (2-tailed)	,674
nodesinus	Z	-,296[b]
	Asymp. Sig. (2-tailed)	,767
pericard	Z	-1,481[c]
	Asymp. Sig. (2-tailed)	,139
pulmonaryartery	Z	-1,836[b]
	Asymp. Sig. (2-tailed)	,066
pulmonicvalve	Z	-,280[c]
	Asymp. Sig. (2-tailed)	,779
rightatrium	Z	-,770[b]
	Asymp. Sig. (2-tailed)	,441
rightcoronararte	Z	-1,599[b]
	Asymp. Sig. (2-tailed)	,110
rightventricle	Z	-,770[b]
	Asymp. Sig. (2-tailed)	,441
superiorvenacava	Z	-1,718[c]
	Asymp. Sig. (2-tailed)	,086
tricuspidalvalve	Z	-1,481[b]
	Asymp. Sig. (2-tailed)	,139

a. Wilcoxon Signed Ranks Test

b. Based on positive ranks.

c. Based on negative ranks.

C.4 Descriptive Statistics, Wilcoxon Signed Rank Test, Photon Robustness: Dmean, Dmax, D45, V15, V30

Descriptive Statistics

Structure		N	Percentiles 25th	Percentiles 50th (Median)
Aorta	D45FB	15	15,92827966000	24,68185540000
	ECLIPSEMaxDoseGyFB	15	101,400	102,200
	ECLIPSEMeanDoseGyFB	15	34,000	43,000
	V15GyFB	15	47,22500000000	63,14990909000
	V30GyFB	15	31,08550000000	38,67677273000
	D45FB_w1	15	16,54552548000	25,20081312000
	ECLIPSEMaxDoseGyFB_w1	15	101,300	101,900
	ECLIPSEMeanDoseGyFB_w1	15	33,900	43,300
	V15GyFB_w1	15	48,32843636000	64,32958182000
	V30GyFB_w1	15	30,34940000000	39,44346364000
AorticValve	D45FB	15	2,39905756800	5,31936719100
	ECLIPSEMaxDoseGyFB	15	8,100	19,100
	ECLIPSEMeanDoseGyFB	15	3,700	9,100
	V15GyFB	15	,00000000000	,00000000000
	V30GyFB	15	,00000000000	,00000000000
	D45FB_w1	15	2,57620810400	5,30719015000
	ECLIPSEMaxDoseGyFB_w1	15	6,500	18,300
	ECLIPSEMeanDoseGyFB_w1	15	4,000	8,900
	V15GyFB_w1	15	,00000000000	,00000000000
	V30GyFB_w1	15	,00000000000	,00000000000
Heart	D45FB	15	1,33875761700	1,97182253900
	ECLIPSEMaxDoseGyFB	15	100,700	102,000
	ECLIPSEMeanDoseGyFB	15	6,900	11,900
	V15GyFB	15	8,83395363600	14,68450000000
	V30GyFB	15	3,34870090900	4,94725000000
	D45FB_w1	15	1,55192049900	2,00716394800
	ECLIPSEMaxDoseGyFB_w1	15	99,700	101,600
	ECLIPSEMeanDoseGyFB_w1	15	8,100	11,800
	V15GyFB_w1	15	10,27337273000	16,65350000000
	V30GyFB_w1	15	4,42202909100	5,12809090900
InferiorVenaCava	D45FB	15	,67078512300	1,13958944000
	ECLIPSEMaxDoseGyFB	15	1,700	2,800
	ECLIPSEMeanDoseGyFB	15	1,100	1,700
	V15GyFB	15	,00000000000	,00000000000
	V30GyFB	15	,00000000000	,00000000000
	D45FB_w1	15	,80005016900	1,10532750000
	ECLIPSEMaxDoseGyFB_w1	15	1,800	2,600
	ECLIPSEMeanDoseGyFB_w1	15	1,200	1,800
	V15GyFB_w1	15	,00000000000	,00000000000
	V30GyFB_w1	15	,00000000000	,00000000000
LeftAntDescArter	D45FB	15	1,66066204800	2,81886355500
	ECLIPSEMaxDoseGyFB	15	14,100	36,700
	ECLIPSEMeanDoseGyFB	15	4,300	7,900
	V15GyFB	15	,00000000000	4,74243454500
	V30GyFB	15	,00000000000	,00000000000
	D45FB_w1	15	2,63341176500	3,41054232100
	ECLIPSEMaxDoseGyFB_w1	15	16,900	42,900

Descriptive Statistics

Structure		Percentiles 75th
Aorta	D45FB	38,50357500000
	ECLIPSEMaxDoseGyFB	102,600
	ECLIPSEMeanDoseGyFB	51,800
	V15GyFB	75,63228182000
	V30GyFB	57,94465455000
	D45FB_w1	41,98527758000
	ECLIPSEMaxDoseGyFB_w1	103,800
	ECLIPSEMeanDoseGyFB_w1	50,700
	V15GyFB_w1	74,57451818000
	V30GyFB_w1	56,13318182000
AorticValve	D45FB	10,66883707000
	ECLIPSEMaxDoseGyFB	38,500
	ECLIPSEMeanDoseGyFB	16,500
	V15GyFB	16,44945455000
	V30GyFB	,00000000000
	D45FB_w1	12,42787556000
	ECLIPSEMaxDoseGyFB_w1	41,100
	ECLIPSEMeanDoseGyFB_w1	18,300
	V15GyFB_w1	26,28443636000
	V30GyFB_w1	,00000000000
Heart	D45FB	7,87877883300
	ECLIPSEMaxDoseGyFB	102,900
	ECLIPSEMeanDoseGyFB	16,300
	V15GyFB	21,55194545000
	V30GyFB	9,42737000000
	D45FB_w1	7,40747640500
	ECLIPSEMaxDoseGyFB_w1	104,300
	ECLIPSEMeanDoseGyFB_w1	18,800
	V15GyFB_w1	25,05110000000
	V30GyFB_w1	11,08400000000
InferiorVenaCava	D45FB	3,98660211300
	ECLIPSEMaxDoseGyFB	9,000
	ECLIPSEMeanDoseGyFB	6,100
	V15GyFB	,00000000000
	V30GyFB	,00000000000
	D45FB_w1	4,82958987200
	ECLIPSEMaxDoseGyFB_w1	11,300
	ECLIPSEMeanDoseGyFB_w1	7,400
	V15GyFB_w1	,00000000000
	V30GyFB_w1	,00000000000
LeftAntDescArter	D45FB	9,45202173900
	ECLIPSEMaxDoseGyFB	56,800
	ECLIPSEMeanDoseGyFB	15,900
	V15GyFB	34,63627273000
	V30GyFB	5,40464454500
	D45FB_w1	13,77658119000
	ECLIPSEMaxDoseGyFB_w1	54,900

Descriptive Statistics

Structure		N	Percentiles 25th	Percentiles 50th (Median)
	ECLIPSEMeanDoseGyFB_w1	15	4,800	7,900
	V15GyFB_w1	15	,00000000000	4,09329181800
	V30GyFB_w1	15	,00000000000	,00000000000
LeftAtrium	D45FB	15	2,97668507400	11,79208257000
	ECLIPSEMaxDoseGyFB	15	96,200	101,100
	ECLIPSEMeanDoseGyFB	15	15,400	22,900
	V15GyFB	15	20,50324545000	32,73760000000
	V30GyFB	15	7,43447909100	13,32940909000
	D45FB_w1	15	6,53914678900	12,87852571000
	ECLIPSEMaxDoseGyFB_w1	15	97,200	100,600
	ECLIPSEMeanDoseGyFB_w1	15	15,700	27,600
	V15GyFB_w1	15	21,53292727000	36,04810000000
	V30GyFB_w1	15	8,59343181800	16,99470909000
LeftCircumflex	D45FB	15	2,14711632000	3,06158505900
	ECLIPSEMaxDoseGyFB	15	13,500	29,000
	ECLIPSEMeanDoseGyFB	15	5,400	7,300
	V15GyFB	15	,00000000000	6,59193545500
	V30GyFB	15	,00000000000	,00000000000
	D45FB_w1	15	2,30139280900	4,39384256600
	ECLIPSEMaxDoseGyFB_w1	15	11,200	27,600
	ECLIPSEMeanDoseGyFB_w1	15	4,000	8,800
	V15GyFB_w1	15	,00000000000	1,64775000000
	V30GyFB_w1	15	,00000000000	,00000000000
LeftMainCoArtery	D45FB	15	8,16917403900	12,82261975000
	ECLIPSEMaxDoseGyFB	15	16,200	34,000
	ECLIPSEMeanDoseGyFB	15	12,400	19,400
	V15GyFB	15	,00000000000	22,65008182000
	V30GyFB	15	,00000000000	,00000000000
	D45FB_w1	15	8,43825592300	14,73214124000
	ECLIPSEMaxDoseGyFB_w1	15	17,000	42,000
	ECLIPSEMeanDoseGyFB_w1	15	12,600	26,300
	V15GyFB_w1	15	,00000000000	41,38820000000
	V30GyFB_w1	15	,00000000000	,00000000000
LeftVentricle	D45FB	15	,86911745200	1,19306425400
	ECLIPSEMaxDoseGyFB	15	6,300	15,300
	ECLIPSEMeanDoseGyFB	15	1,500	2,500
	V15GyFB	15	,00000000000	,00000000000
	V30GyFB	15	,00000000000	,00000000000
	D45FB_w1	15	1,00579148300	1,21513719100
	ECLIPSEMaxDoseGyFB_w1	15	10,900	15,600
	ECLIPSEMeanDoseGyFB_w1	15	1,800	2,500
	V15GyFB_w1	15	,00000000000	,00000000000
	V30GyFB_w1	15	,00000000000	,00000000000
MitralValve	D45FB	15	1,72691324500	2,73517170100
	ECLIPSEMaxDoseGyFB	15	4,400	14,200
	ECLIPSEMeanDoseGyFB	15	2,600	4,900
	V15GyFB	15	,00000000000	,00000000000

Descriptive Statistics

Structure		Percentiles 75th
	ECLIPSEMeanDoseGyFB_w1	23,300
	V15GyFB_w1	39,76623636000
	V30GyFB_w1	11,51432727000
LeftAtrium	D45FB	17,41651210000
	ECLIPSEMaxDoseGyFB	103,000
	ECLIPSEMeanDoseGyFB	37,300
	V15GyFB	48,64230000000
	V30GyFB	31,53550000000
	D45FB_w1	17,56023529000
	ECLIPSEMaxDoseGyFB_w1	102,800
	ECLIPSEMeanDoseGyFB_w1	37,000
	V15GyFB_w1	49,86590000000
	V30GyFB_w1	31,36470000000
LeftCircumflex	D45FB	8,34844067800
	ECLIPSEMaxDoseGyFB	64,200
	ECLIPSEMeanDoseGyFB	14,700
	V15GyFB	21,32182727000
	V30GyFB	13,21017273000
	D45FB_w1	10,49973109000
	ECLIPSEMaxDoseGyFB_w1	70,600
	ECLIPSEMeanDoseGyFB_w1	22,400
	V15GyFB_w1	40,28875455000
	V30GyFB_w1	21,42093636000
LeftMainCoArtery	D45FB	25,43289576000
	ECLIPSEMaxDoseGyFB	48,700
	ECLIPSEMeanDoseGyFB	38,200
	V15GyFB	100,0000000000
	V30GyFB	12,27881818000
	D45FB_w1	24,93890328000
	ECLIPSEMaxDoseGyFB_w1	62,800
	ECLIPSEMeanDoseGyFB_w1	44,500
	V15GyFB_w1	100,0000000000
	V30GyFB_w1	26,20280000000
LeftVentricle	D45FB	4,98781208100
	ECLIPSEMaxDoseGyFB	51,700
	ECLIPSEMeanDoseGyFB	8,900
	V15GyFB	2,82342181800
	V30GyFB	,31507536400
	D45FB_w1	6,45008799400
	ECLIPSEMaxDoseGyFB_w1	51,900
	ECLIPSEMeanDoseGyFB_w1	11,700
	V15GyFB_w1	9,45288818200
	V30GyFB_w1	,23135800000
MitralValve	D45FB	11,08155417000
	ECLIPSEMaxDoseGyFB	49,200
	ECLIPSEMeanDoseGyFB	17,300
	V15GyFB	22,27391818000

Descriptive Statistics

Structure		N	Percentiles 25th	Percentiles 50th (Median)
	V30GyFB	15	,00000000000	,00000000000
	D45FB_w1	15	1,53376460500	3,13163217300
	ECLIPSEMaxDoseGyFB_w1	15	7,500	12,300
	ECLIPSEMeanDoseGyFB_w1	15	2,600	6,100
	V15GyFB_w1	15	,00000000000	,00000000000
	V30GyFB_w1	15	,00000000000	,00000000000
NodeAV	D45FB	15	1,21511298300	2,21812082300
	ECLIPSEMaxDoseGyFB	15	2,500	6,000
	ECLIPSEMeanDoseGyFB	15	1,900	3,700
	V15GyFB	15	,00000000000	,00000000000
	V30GyFB	15	,00000000000	,00000000000
	D45FB_w1	15	1,48854947800	2,83231657000
	ECLIPSEMaxDoseGyFB_w1	15	2,900	7,600
	ECLIPSEMeanDoseGyFB_w1	15	2,200	4,600
	V15GyFB_w1	15	,00000000000	,00000000000
	V30GyFB_w1	15	,00000000000	,00000000000
NodeSinus	D45FB	15	2,87068590800	5,30222895100
	ECLIPSEMaxDoseGyFB	15	6,500	25,100
	ECLIPSEMeanDoseGyFB	15	5,500	8,700
	V15GyFB	15	,00000000000	2,50846454500
	V30GyFB	15	,00000000000	,00000000000
	D45FB_w1	15	3,20404918500	6,30847365900
	ECLIPSEMaxDoseGyFB_w1	15	10,200	25,600
	ECLIPSEMeanDoseGyFB_w1	15	5,700	10,300
	V15GyFB_w1	15	,00000000000	2,30833181800
	V30GyFB_w1	15	,00000000000	,00000000000
Pericard	D45FB	15	1,27568714300	2,00608004500
	ECLIPSEMaxDoseGyFB	15	100,700	102,000
	ECLIPSEMeanDoseGyFB	15	10,600	14,800
	V15GyFB	15	13,57047273000	19,69292727000
	V30GyFB	15	6,52899181800	10,86052727000
	D45FB_w1	15	1,49741925300	1,99508903900
	ECLIPSEMaxDoseGyFB_w1	15	99,700	101,600
	ECLIPSEMeanDoseGyFB_w1	15	10,600	14,900
	V15GyFB_w1	15	13,88419091000	20,93277273000
	V30GyFB_w1	15	7,99111272700	9,44564000000
PulmonaryArtery	D45FB	15	22,13777403000	42,73161731000
	ECLIPSEMaxDoseGyFB	15	100,400	101,500
	ECLIPSEMeanDoseGyFB	15	40,000	61,400
	V15GyFB	15	72,08137273000	93,11901818000
	V30GyFB	15	31,62520000000	64,06450000000
	D45FB_w1	15	23,08633894000	39,10401450000
	ECLIPSEMaxDoseGyFB_w1	15	99,600	101,700
	ECLIPSEMeanDoseGyFB_w1	15	39,400	59,100
	V15GyFB_w1	15	79,30518182000	93,63090000000
	V30GyFB_w1	15	27,84273636000	69,91260000000

Descriptive Statistics

Structure		Percentiles 75th
	V30GyFB	,40161181800
	D45FB_w1	17,03305934000
	ECLIPSEMaxDoseGyFB_w1	48,800
	ECLIPSEMeanDoseGyFB_w1	25,800
	V15GyFB_w1	59,30258182000
	V30GyFB_w1	,27915472700
NodeAV	D45FB	5,02758842800
	ECLIPSEMaxDoseGyFB	18,000
	ECLIPSEMeanDoseGyFB	7,900
	V15GyFB	,00000000000
	V30GyFB	,00000000000
	D45FB_w1	7,16434925400
	ECLIPSEMaxDoseGyFB_w1	20,800
	ECLIPSEMeanDoseGyFB_w1	10,900
	V15GyFB_w1	,00000000000
	V30GyFB_w1	,00000000000
NodeSinus	D45FB	14,52078133000
	ECLIPSEMaxDoseGyFB	55,300
	ECLIPSEMeanDoseGyFB	27,300
	V15GyFB	43,56020000000
	V30GyFB	4,07803000000
	D45FB_w1	14,16844933000
	ECLIPSEMaxDoseGyFB_w1	62,900
	ECLIPSEMeanDoseGyFB_w1	24,100
	V15GyFB_w1	36,65940000000
	V30GyFB_w1	12,24660000000
Pericard	D45FB	6,64932026600
	ECLIPSEMaxDoseGyFB	102,900
	ECLIPSEMeanDoseGyFB	19,600
	V15GyFB	25,39063636000
	V30GyFB	14,19983636000
	D45FB_w1	6,82394075100
	ECLIPSEMaxDoseGyFB_w1	104,300
	ECLIPSEMeanDoseGyFB_w1	20,800
	V15GyFB_w1	24,99400000000
	V30GyFB_w1	17,70270909000
PulmonaryArtery	D45FB	52,35230880000
	ECLIPSEMaxDoseGyFB	102,200
	ECLIPSEMeanDoseGyFB	70,600
	V15GyFB	99,75781818000
	V30GyFB	83,28590000000
	D45FB_w1	58,24317231000
	ECLIPSEMaxDoseGyFB_w1	102,100
	ECLIPSEMeanDoseGyFB_w1	77,200
	V15GyFB_w1	100,0000000000
	V30GyFB_w1	91,98977273000

Descriptive Statistics

Structure		N	Percentiles 25th	Percentiles 50th (Median)
PulmonicValve	D45FB	15	9,20348606000	11,67092353000
	ECLIPSEMaxDoseGyFB	15	23,700	38,900
	ECLIPSEMeanDoseGyFB	15	13,800	18,800
	V15GyFB	15	,10129971800	17,80460000000
	V30GyFB	15	,00000000000	,00000000000
	D45FB_w1	15	7,50720849600	12,79361910000
	ECLIPSEMaxDoseGyFB_w1	15	23,800	38,200
	ECLIPSEMeanDoseGyFB_w1	15	12,600	19,900
	V15GyFB_w1	15	,00000000000	31,12030000000
	V30GyFB_w1	15	,00000000000	,00000000000
RightAtrium	D45FB	15	1,18383287900	1,87190691800
	ECLIPSEMaxDoseGyFB	15	13,700	25,800
	ECLIPSEMeanDoseGyFB	15	3,000	5,100
	V15GyFB	15	,00000000000	,77810354500
	V30GyFB	15	,00000000000	,00000000000
	D45FB_w1	15	1,50073844300	2,14291521200
	ECLIPSEMaxDoseGyFB_w1	15	17,900	53,100
	ECLIPSEMeanDoseGyFB_w1	15	2,900	5,800
	V15GyFB_w1	15	,00000000000	,72565927300
	V30GyFB_w1	15	,00000000000	,02167453600
RightCoronarArte	D45FB	15	1,09346353700	1,56309770100
	ECLIPSEMaxDoseGyFB	15	5,900	12,300
	ECLIPSEMeanDoseGyFB	15	2,100	3,400
	V15GyFB	15	,00000000000	,00000000000
	V30GyFB	15	,00000000000	,00000000000
	D45FB_w1	15	1,15769242700	1,30158557600
	ECLIPSEMaxDoseGyFB_w1	15	4,400	12,700
	ECLIPSEMeanDoseGyFB_w1	15	2,000	2,900
	V15GyFB_w1	15	,00000000000	,00000000000
	V30GyFB_w1	15	,00000000000	,00000000000
RightVentricle	D45FB	15	,88598837100	1,15954962200
	ECLIPSEMaxDoseGyFB	15	8,600	19,400
	ECLIPSEMeanDoseGyFB	15	1,600	2,700
	V15GyFB	15	,00000000000	,00000000000
	V30GyFB	15	,00000000000	,00000000000
	D45FB_w1	15	,99897227100	1,24276487300
	ECLIPSEMaxDoseGyFB_w1	15	15,600	26,600
	ECLIPSEMeanDoseGyFB_w1	15	2,100	3,400
	V15GyFB_w1	15	,00000000000	,06889330000
	V30GyFB_w1	15	,00000000000	,00000000000
SuperiorVenaCava	D45FB	15	15,49032500000	52,63665191000
	ECLIPSEMaxDoseGyFB	15	43,200	89,800
	ECLIPSEMeanDoseGyFB	15	22,500	60,300
	V15GyFB	15	48,91560909000	99,05761818000
	V30GyFB	15	,00000000000	60,59210000000
	D45FB_w1	15	16,55188446000	47,19205479000
	ECLIPSEMaxDoseGyFB_w1	15	52,200	86,200

Descriptive Statistics

Structure		Percentiles 75th
PulmonicValve	D45FB	21,98894292000
	ECLIPSEMaxDoseGyFB	54,400
	ECLIPSEMeanDoseGyFB	34,000
	V15GyFB	75,36028182000
	V30GyFB	10,18310000000
	D45FB_w1	22,34248797000
	ECLIPSEMaxDoseGyFB_w1	53,200
	ECLIPSEMeanDoseGyFB_w1	34,400
	V15GyFB_w1	97,35728182000
	V30GyFB_w1	9,83883636400
RightAtrium	D45FB	4,51055799100
	ECLIPSEMaxDoseGyFB	62,900
	ECLIPSEMeanDoseGyFB	11,200
	V15GyFB	12,50450000000
	V30GyFB	1,10108090900
	D45FB_w1	5,06531808900
	ECLIPSEMaxDoseGyFB_w1	67,800
	ECLIPSEMeanDoseGyFB_w1	15,700
	V15GyFB_w1	16,23669091000
	V30GyFB_w1	2,43465909100
RightCoronarArte	D45FB	3,99340440000
	ECLIPSEMaxDoseGyFB	22,400
	ECLIPSEMeanDoseGyFB	7,400
	V15GyFB	,00000000000
	V30GyFB	,00000000000
	D45FB_w1	5,59503878800
	ECLIPSEMaxDoseGyFB_w1	32,200
	ECLIPSEMeanDoseGyFB_w1	9,700
	V15GyFB_w1	4,62219000000
	V30GyFB_w1	,00000000000
RightVentricle	D45FB	3,81157695500
	ECLIPSEMaxDoseGyFB	41,000
	ECLIPSEMeanDoseGyFB	8,100
	V15GyFB	6,51714181800
	V30GyFB	,00000000000
	D45FB_w1	4,24751628400
	ECLIPSEMaxDoseGyFB_w1	39,600
	ECLIPSEMeanDoseGyFB_w1	8,500
	V15GyFB_w1	5,14574272700
	V30GyFB_w1	,00000000000
SuperiorVenaCava	D45FB	54,43000814000
	ECLIPSEMaxDoseGyFB	101,200
	ECLIPSEMeanDoseGyFB	82,000
	V15GyFB	100,0000000000
	V30GyFB	98,10557273000
	D45FB_w1	58,26707193000
	ECLIPSEMaxDoseGyFB_w1	100,900

Descriptive Statistics

Structure		N	Percentiles 25th	Percentiles 50th (Median)
	ECLIPSEMeanDoseGyFB_w1	15	25,200	53,400
	V15GyFB_w1	15	60,22130000000	94,58490000000
	V30GyFB_w1	15	,23080509100	54,15290000000
TricuspidalValve	D45FB	15	,95902151600	1,28595308900
	ECLIPSEMaxDoseGyFB	15	2,200	3,300
	ECLIPSEMeanDoseGyFB	15	1,500	1,900
	V15GyFB	15	,00000000000	,00000000000
	V30GyFB	15	,00000000000	,00000000000
	D45FB_w1	15	1,11610647100	1,42652774300
	ECLIPSEMaxDoseGyFB_w1	15	2,300	3,500
	ECLIPSEMeanDoseGyFB_w1	15	1,700	2,300
	V15GyFB_w1	15	,00000000000	,00000000000
	V30GyFB_w1	15	,00000000000	,00000000000

Descriptive Statistics

Structure		Percentiles 75th
	ECLIPSEMeanDoseGyFB_w1	77,600
	V15GyFB_w1	100,0000000000
	V30GyFB_w1	98,45308182000
TricuspidalValve	D45FB	4,92093772200
	ECLIPSEMaxDoseGyFB	11,300
	ECLIPSEMeanDoseGyFB	7,400
	V15GyFB	,00000000000
	V30GyFB	,00000000000
	D45FB_w1	5,66532346000
	ECLIPSEMaxDoseGyFB_w1	13,000
	ECLIPSEMeanDoseGyFB_w1	8,600
	V15GyFB_w1	,00000000000
	V30GyFB_w1	,00000000000

Wilcoxon Signed Ranks Test

Test Statistics[a]

Structure		D45FB_w1 - D45FB	ECLIPSEMaxDoseGyFB_w1 - ECLIPSEMaxDoseGyFB	ECLIPSEMeanDoseGyFB_w1 - ECLIPSEMeanDoseGyFB
Aorta	Z	-,511[b]	-,057[c]	-,094[b]
	Asymp. Sig. (2-tailed)	,609	,955	,925
AorticValve	Z	-,966[b]	-,085[b]	-1,136[b]
	Asymp. Sig. (2-tailed)	,334	,932	,256
Heart	Z	-1,420[b]	-,028[b]	-1,468[b]
	Asymp. Sig. (2-tailed)	,156	,977	,142
InferiorVenaCava	Z	-1,363[b]	-,769[b]	-1,577[b]
	Asymp. Sig. (2-tailed)	,173	,442	,115
LeftAntDescArter	Z	-3,237[b]	-,625[b]	-1,590[b]
	Asymp. Sig. (2-tailed)	,001	,532	,112
LeftAtrium	Z	-1,306[b]	-,754[b]	-1,478[b]
	Asymp. Sig. (2-tailed)	,191	,451	,139
LeftCircumflex	Z	-1,874[b]	-,738[c]	-,510[b]
	Asymp. Sig. (2-tailed)	,061	,460	,610
LeftMainCoArtery	Z	-,114[c]	-,852[b]	-,057[b]
	Asymp. Sig. (2-tailed)	,910	,394	,955
LeftVentricle	Z	-1,647[b]	-,426[c]	-1,731[b]
	Asymp. Sig. (2-tailed)	,100	,670	,083
MitralValve	Z	-2,272[b]	-,114[c]	-2,330[b]
	Asymp. Sig. (2-tailed)	,023	,910	,020
NodeAV	Z	-2,215[b]	-2,692[b]	-2,552[b]
	Asymp. Sig. (2-tailed)	,027	,007	,011
NodeSinus	Z	-,284[b]	-1,079[b]	-,512[b]
	Asymp. Sig. (2-tailed)	,776	,280	,609
Pericard	Z	-1,704[b]	-,057[b]	-1,287[b]
	Asymp. Sig. (2-tailed)	,088	,955	,198
PulmonaryArtery	Z	-1,022[b]	-1,250[c]	-1,079[b]
	Asymp. Sig. (2-tailed)	,307	,211	,281
PulmonicValve	Z	-,966[b]	-1,250[b]	-1,099[b]
	Asymp. Sig. (2-tailed)	,334	,211	,272
RightAtrium	Z	-1,931[b]	-1,307[b]	-2,472[b]
	Asymp. Sig. (2-tailed)	,053	,191	,013
RightCoronarArte	Z	-1,193[b]	-,171[b]	-1,434[b]
	Asymp. Sig. (2-tailed)	,233	,865	,151
RightVentricle	Z	-1,533[b]	-,471[b]	-1,854[b]
	Asymp. Sig. (2-tailed)	,125	,637	,064
SuperiorVenaCava	Z	-1,079[c]	-1,601[c]	-1,506[c]
	Asymp. Sig. (2-tailed)	,281	,109	,132
TricuspidalValve	Z	-1,533[b]	-,094[b]	-1,857[b]
	Asymp. Sig. (2-tailed)	,125	,925	,063

Test Statistics[a]

Structure		V15GyFB_w1 - V15GyFB	V30GyFB_w1 - V30GyFB
Aorta	Z	-,114[c]	-,454[b]
	Asymp. Sig. (2-tailed)	,910	,650
AorticValve	Z	-,943[b]	-1,342[b]
	Asymp. Sig. (2-tailed)	,345	,180
Heart	Z	-1,420[b]	-1,412[b]
	Asymp. Sig. (2-tailed)	,156	,158
InferiorVenaCava	Z	-1,000[b]	-1,000[b]
	Asymp. Sig. (2-tailed)	,317	,317
LeftAntDescArter	Z	-,889[b]	-1,859[b]
	Asymp. Sig. (2-tailed)	,374	,063
LeftAtrium	Z	-2,291[b]	-1,664[b]
	Asymp. Sig. (2-tailed)	,022	,096
LeftCircumflex	Z	-,663[b]	-,676[b]
	Asymp. Sig. (2-tailed)	,508	,499
LeftMainCoArtery	Z	-,280[b]	-,338[b]
	Asymp. Sig. (2-tailed)	,779	,735
LeftVentricle	Z	-1,352[b]	-1,214[c]
	Asymp. Sig. (2-tailed)	,176	,225
MitralValve	Z	-1,992[b]	-1,461[b]
	Asymp. Sig. (2-tailed)	,046	,144
NodeAV	Z	-1,604[b]	,000[d]
	Asymp. Sig. (2-tailed)	,109	1,000
NodeSinus	Z	-,845[b]	-,943[b]
	Asymp. Sig. (2-tailed)	,398	,345
Pericard	Z	-1,193[b]	-1,538[b]
	Asymp. Sig. (2-tailed)	,233	,124
PulmonaryArtery	Z	-,804[b]	-1,136[b]
	Asymp. Sig. (2-tailed)	,422	,256
PulmonicValve	Z	-1,682[b]	,000[d]
	Asymp. Sig. (2-tailed)	,093	1,000
RightAtrium	Z	-2,223[b]	-1,820[b]
	Asymp. Sig. (2-tailed)	,026	,069
RightCoronarArte	Z	-1,826[b]	-1,000[b]
	Asymp. Sig. (2-tailed)	,068	,317
RightVentricle	Z	-1,362[b]	-,447[b]
	Asymp. Sig. (2-tailed)	,173	,655
SuperiorVenaCava	Z	-1,120[c]	-,549[c]
	Asymp. Sig. (2-tailed)	,263	,583
TricuspidalValve	Z	-1,000[b]	,000[d]
	Asymp. Sig. (2-tailed)	,317	1,000

a. Wilcoxon Signed Ranks Test

b. Based on negative ranks.

c. Based on positive ranks.

d. The sum of negative ranks equals the sum of positive ranks.

C.5 Descriptive Statistics, Wilcoxon Signed Rank Test, Proton Robustness: Dmean, D0, D45, V15, V30

Descriptive Statistics

Structure		N	Percentiles 25th	50th (Median)	75th
Aorta	D45FB	15	1,75200000000	5,95700000000	26,14700000000
	V15GyFB	15	24,39037363000	38,64011321000	54,59402740000
	V30GyFB	15	11,97108621000	30,66710224000	41,94333962000
	AplanDmean	14	11,6975	20,0800	26,8800
	D45FB_w1	15	1,608000E+000	1,189400E+001	2,645000E+001
	V15GyFB_w1	15	23,67515753000	40,94881919000	53,01201466000
	V30GyFB_w1	15	12,86767241000	26,60417363000	40,78671704000
	Aw1Dmean	14	11,1400	20,6450	26,2800
AorticValve	D45FB	15	,01300000000	,09100000000	,60700000000
	V15GyFB	15	,00000000000	,00000000000	,00000000000
	V30GyFB	15	,00000000000	,00000000000	,00000000000
	AplanDmean	14	,0350	,1400	,7500
	D45FB_w1	15	1,800000E-002	1,080000E-001	4,620000E-001
	V15GyFB_w1	15	,00000000000	,00000000000	,00000000000
	V30GyFB_w1	15	,00000000000	,00000000000	,00000000000
	Aw1Dmean	14	,0350	,1300	,5550
Heart	D45FB	15	,00850000000	,02700000000	,17700000000
	V15GyFB	15	2,23438484000	3,91865306100	8,56224749200
	V30GyFB	15	1,26055685100	2,04535568500	5,04914985600
	AplanDmean	14	1,0450	1,8200	4,3725
	D45FB_w1	15	1,700000E-002	2,800000E-002	1,200000E-001
	V15GyFB_w1	15	2,62662500000	4,81091318300	8,99866336600
	V30GyFB_w1	15	1,56250000000	2,58625401900	6,15018950400
	Aw1Dmean	14	1,0975	2,1500	4,1950
InferiorVenaCava	D45FB	15	,00295652200	,03333333300	,14000000000
	V15GyFB	15	,00000000000	,00000000000	,00000000000
	V30GyFB	15	,00000000000	,00000000000	,00000000000
	AplanDmean	14	,0000	,0350	,1275
	D45FB_w1	15	3,000000E-003	2,109100E-002	2,030000E-001
	V15GyFB_w1	15	,00000000000	,00000000000	,00000000000
	V30GyFB_w1	15	,00000000000	,00000000000	,00000000000
	Aw1Dmean	14	,0000	,0150	,1825
LeftAntDescArter	D45FB	15	,00000000000	,06700000000	,15695950600
	V15GyFB	15	,00000000000	,00000000000	,02700000000
	V30GyFB	15	,00000000000	,00000000000	,00000000000
	AplanDmean	14	,0450	,3600	1,2375
	D45FB_w1	15	1,000000E-002	5,900000E-002	2,620000E-001
	V15GyFB_w1	15	,00000000000	,00000000000	,65900000000
	V30GyFB_w1	15	,00000000000	,00000000000	,00000000000
	Aw1Dmean	14	,0550	,3700	2,0675
LeftAtrium	D45FB	15	,32300000000	1,06700000000	3,59300000000
	V15GyFB	15	8,85243055600	13,51636808000	29,48110390000

Descriptive Statistics

Structure		N	Percentiles 25th	50th (Median)	75th
	V30GyFB	15	4,34622916700	8,04958187100	20,45704762000
	AplanDmean	14	4,0125	6,0800	15,1250
	D45FB_w1	15	5,670000E-001	1,287000E+000	1,086100E+001
	V15GyFB_w1	15	10,10963514000	19,09281766000	40,52199361000
	V30GyFB_w1	15	4,54470945900	12,71705476000	28,14707006000
	Aw1Dmean	14	4,2300	8,5950	17,4625
LeftCircumflex	D45FB	15	,05000892000	,19900000000	,76337655900
	V15GyFB	15	,00000000000	,00000000000	6,87200000000
	V30GyFB	15	,00000000000	,00000000000	,25200000000
	AplanDmean	14	,0800	,9300	5,6875
	D45FB_w1	15	5,200000E-002	1,780000E-001	1,232000E+000
	V15GyFB_w1	15	,00000000000	,00000000000	23,25700000000
	V30GyFB_w1	15	,00000000000	,00000000000	17,67200000000
	Aw1Dmean	14	,0700	,5400	12,8050
LeftMainCoArtery	D45FB	15	,13872358900	1,07737748300	2,09953495400
	V15GyFB	15	,00000000000	,00000000000	,00000000000
	V30GyFB	15	,00000000000	,00000000000	,00000000000
	AplanDmean	14	,2125	1,4400	2,5575
	D45FB_w1	15	1,406350E-001	7,190000E-001	3,723188E+000
	V15GyFB_w1	15	,00000000000	,00000000000	,77800000000
	V30GyFB_w1	15	,00000000000	,00000000000	,00000000000
	Aw1Dmean	14	,3350	1,2950	5,4275
LeftVentricle	D45FB	15	,00350000000	,01854379600	,08600000000
	V15GyFB	15	,00000000000	,00000000000	,00000000000
	V30GyFB	15	,00000000000	,00000000000	,00000000000
	AplanDmean	14	,0100	,0500	,3850
	D45FB_w1	15	5,636000E-003	1,166700E-002	8,900000E-002
	V15GyFB_w1	15	,00000000000	,00000000000	,00000000000
	V30GyFB_w1	15	,00000000000	,00000000000	,00000000000
	Aw1Dmean	14	,0100	,0450	,6900
MitralValve	D45FB	15	,02720000000	,12000000000	,39500000000
	V15GyFB	15	,00000000000	,00000000000	,00000000000
	V30GyFB	15	,00000000000	,00000000000	,00000000000
	AplanDmean	14	,0375	,2050	1,0275
	D45FB_w1	15	3,600000E-002	1,250000E-001	4,700000E-001
	V15GyFB_w1	15	,00000000000	,00000000000	,00000000000
	V30GyFB_w1	15	,00000000000	,00000000000	,00000000000
	Aw1Dmean	14	,0425	,2450	1,3275
NodeAV	D45FB	15	,00653214100	,04800000000	,18600000000
	V15GyFB	15	,00000000000	,00000000000	,00000000000
	V30GyFB	15	,00000000000	,00000000000	,00000000000
	AplanDmean	14	,0100	,0650	,2050
	D45FB_w1	15	1,018200E-002	4,500000E-002	1,590000E-001
	V15GyFB_w1	15	,00000000000	,00000000000	,00000000000
	V30GyFB_w1	15	,00000000000	,00000000000	,00000000000
	Aw1Dmean	14	,0100	,0500	,1875

Descriptive Statistics

Structure		N	Percentiles 25th	50th (Median)	75th
NodeSinus	D45FB	15	,01236927600	,26800000000	5,05582802500
	V15GyFB	15	,00000000000	,00000000000	10,35912500000
	V30GyFB	15	,00000000000	,00000000000	,00000000000
	AplanDmean	14	,0100	,4000	6,6825
	D45FB_w1	15	5,295000E-003	1,950000E-001	2,781000E+000
	V15GyFB_w1	15	,00000000000	,00000000000	,37000000000
	V30GyFB_w1	15	,00000000000	,00000000000	,00000000000
	Aw1Dmean	14	,0075	,2200	4,1850
Pericard	D45FB	15	,01400000000	,03000000000	,16100000000
	V15GyFB	15	5,11076132900	8,72624260400	14,58830159000
	V30GyFB	15	3,19354078500	5,45616568000	9,87286455300
	AplanDmean	14	2,3725	3,8950	7,4350
	D45FB_w1	15	2,300000E-002	3,200000E-002	1,010000E-001
	V15GyFB_w1	15	6,08372934500	10,85610611000	13,11601453000
	V30GyFB_w1	15	3,96072857100	7,22569774900	9,05800000000
	Aw1Dmean	14	2,7825	4,6150	6,7950
PulmonaryArtery	D45FB	15	3,72500000000	22,49100000000	40,02500000000
	V15GyFB	15	28,51594444000	49,93572174000	66,87879397000
	V30GyFB	15	18,20100000000	36,98121633000	52,29266912000
	AplanDmean	14	12,3325	26,9900	34,6400
	D45FB_w1	15	9,674000E+000	1,848500E+001	4,193200E+001
	V15GyFB_w1	15	36,20249345000	49,58525373000	64,40832584000
	V30GyFB_w1	15	22,53955102000	33,29550442000	54,45007256000
	Aw1Dmean	14	17,0050	22,0450	35,9250
PulmonicValve	D45FB	15	,00569078500	,19200000000	,56900000000
	V15GyFB	15	,00000000000	,00000000000	,00000000000
	V30GyFB	15	,00000000000	,00000000000	,00000000000
	AplanDmean	14	,0800	,4550	1,0450
	D45FB_w1	15	2,233300E-002	1,660000E-001	4,590000E-001
	V15GyFB_w1	15	,00000000000	,00000000000	,00000000000
	V30GyFB_w1	15	,00000000000	,00000000000	,00000000000
	Aw1Dmean	14	,1350	,3950	,9650
RightAtrium	D45FB	15	,00614277600	,07331412900	,27600000000
	V15GyFB	15	,00000000000	,00000000000	,86968382400
	V30GyFB	15	,00000000000	,00000000000	,00000000000
	AplanDmean	14	,0075	,1250	1,3550
	D45FB_w1	15	3,200000E-003	8,000000E-002	2,960000E-001
	V15GyFB_w1	15	,00000000000	,00000000000	,97348292700
	V30GyFB_w1	15	,00000000000	,00000000000	,06200000000
	Aw1Dmean	14	,0075	,0800	1,1150
RightCoronarArte	D45FB	14	,00000000000	,02188092100	,12609985575
	V15GyFB	14	,00000000000	,00000000000	,00000000000

Descriptive Statistics

Structure		N	Percentiles 25th	50th (Median)	75th
	V30GyFB	14	,00000000000	,00000000000	,00000000000
	AplanDmean	14	,0000	,0250	,1475
	D45FB_w1	15	0,000000E+000	1,000000E-003	9,254100E-002
	V15GyFB_w1	15	,00000000000	,00000000000	,00000000000
	V30GyFB_w1	15	,00000000000	,00000000000	,00000000000
	Aw1Dmean	14	,0000	,0200	,1150
RightVentricle	D45FB	14	,00000000000	,00640000000	,05800000000
	V15GyFB	14	,00000000000	,00000000000	,00000000000
	V30GyFB	14	,00000000000	,00000000000	,00000000000
	AplanDmean	14	,0000	,0200	,0925
	D45FB_w1	15	0,000000E+000	0,000000E+000	4,500000E-002
	V15GyFB_w1	15	,00000000000	,00000000000	,00000000000
	V30GyFB_w1	15	,00000000000	,00000000000	,00000000000
	Aw1Dmean	14	,0000	,0150	,0650
SuperiorVenaCava	D45FB	15	,36900000000	46,89900000000	56,19100000000
	V15GyFB	15	2,86600000000	67,70215873000	91,12135678000
	V30GyFB	15	,03800000000	56,65668471000	75,74073469000
	AplanDmean	14	1,6350	27,8050	50,5475
	D45FB_w1	15	3,076150E-001	2,858600E+001	5,346100E+001
	V15GyFB_w1	15	,00000000000	62,29670968000	88,09782822000
	V30GyFB_w1	15	,00000000000	42,90775000000	73,00260465000
	Aw1Dmean	14	,4425	19,4400	41,6425
TricuspidalValve	D45FB	15	,00000000000	,01401574800	,07763898900
	V15GyFB	15	,00000000000	,00000000000	,00000000000
	V30GyFB	15	,00000000000	,00000000000	,00000000000
	AplanDmean	14	,0000	,0200	,0850
	D45FB_w1	15	0,000000E+000	8,227000E-003	6,721900E-002
	V15GyFB_w1	15	,00000000000	,00000000000	,00000000000
	V30GyFB_w1	15	,00000000000	,00000000000	,00000000000
	Aw1Dmean	14	,0000	,0100	,0775

Wilcoxon Signed Ranks Test

Test Statistics[a]

Structure		D45FB_w1 - D45FB	V15GyFB_w1 - V15GyFB	V30GyFB_w1 - V30GyFB
Aorta	Z	-,738[b]	-,625[b]	-1,022[b]
	Asymp. Sig. (2-tailed)	,460	,532	,307
AorticValve	Z	-1,022[b]	,000[c]	,000[c]
	Asymp. Sig. (2-tailed)	,307	1,000	1,000
Heart	Z	-,313[b]	-,682[d]	-,785[d]
	Asymp. Sig. (2-tailed)	,755	,496	,433
InferiorVenaCava	Z	-,175[d]	-1,000[d]	,000[c]
	Asymp. Sig. (2-tailed)	,861	,317	1,000
LeftAntDescArter	Z	-1,503[d]	-,943[d]	-,535[d]
	Asymp. Sig. (2-tailed)	,133	,345	,593
LeftAtrium	Z	-,057[d]	-1,099[d]	-1,161[d]
	Asymp. Sig. (2-tailed)	,955	,272	,245
LeftCircumflex	Z	-,852[d]	-,169[d]	-,405[d]
	Asymp. Sig. (2-tailed)	,394	,866	,686
LeftMainCoArtery	Z	-,398[b]	,000[c]	-,535[b]
	Asymp. Sig. (2-tailed)	,691	1,000	,593
LeftVentricle	Z	-1,083[d]	-1,604[d]	-1,069[d]
	Asymp. Sig. (2-tailed)	,279	,109	,285
MitralValve	Z	-1,590[d]	-1,069[d]	-,447[d]
	Asymp. Sig. (2-tailed)	,112	,285	,655
NodeAV	Z	-1,036[d]	,000[c]	,000[c]
	Asymp. Sig. (2-tailed)	,300	1,000	1,000
NodeSinus	Z	-1,477[b]	-1,483[b]	,000[c]
	Asymp. Sig. (2-tailed)	,140	,138	1,000
Pericard	Z	-,534[b]	-1,079[d]	-1,161[d]
	Asymp. Sig. (2-tailed)	,593	,281	,245
PulmonaryArtery	Z	-,625[d]	-,852[d]	-,284[d]
	Asymp. Sig. (2-tailed)	,532	,394	,776
PulmonicValve	Z	-,628[b]	-,730[b]	-1,000[b]
	Asymp. Sig. (2-tailed)	,530	,465	,317
RightAtrium	Z	-,350[b]	-1,183[d]	-1,214[d]
	Asymp. Sig. (2-tailed)	,727	,237	,225
RightCoronarArte	Z	-1,481[b]	,000[c]	,000[c]
	Asymp. Sig. (2-tailed)	,139	1,000	1,000
RightVentricle	Z	-,681[b]	-1,000[b]	-1,000[b]
	Asymp. Sig. (2-tailed)	,496	,317	,317
SuperiorVenaCava	Z	-2,726[b]	-2,432[b]	-2,589[b]
	Asymp. Sig. (2-tailed)	,006	,015	,010
TricuspidalValve	Z	-1,778[b]	,000[c]	,000[c]
	Asymp. Sig. (2-tailed)	,075	1,000	1,000

Test Statistics[a]

Structure		Aw1Dmean - AplanDmean
Aorta	Z	-1,412[b]
	Asymp. Sig. (2-tailed)	,158
AorticValve	Z	-1,851[b]
	Asymp. Sig. (2-tailed)	,064
Heart	Z	-,282[d]
	Asymp. Sig. (2-tailed)	,778
InferiorVenaCava	Z	-1,123[d]
	Asymp. Sig. (2-tailed)	,261
LeftAntDescArter	Z	-,471[d]
	Asymp. Sig. (2-tailed)	,638
LeftAtrium	Z	-,524[d]
	Asymp. Sig. (2-tailed)	,600
LeftCircumflex	Z	-1,015[b]
	Asymp. Sig. (2-tailed)	,310
LeftMainCoArtery	Z	-,597[b]
	Asymp. Sig. (2-tailed)	,551
LeftVentricle	Z	-1,489[d]
	Asymp. Sig. (2-tailed)	,137
MitralValve	Z	-,420[d]
	Asymp. Sig. (2-tailed)	,675
NodeAV	Z	-,254[d]
	Asymp. Sig. (2-tailed)	,799
NodeSinus	Z	-1,784[b]
	Asymp. Sig. (2-tailed)	,074
Pericard	Z	-,804[d]
	Asymp. Sig. (2-tailed)	,422
PulmonaryArtery	Z	-,094[d]
	Asymp. Sig. (2-tailed)	,925
PulmonicValve	Z	-,524[b]
	Asymp. Sig. (2-tailed)	,600
RightAtrium	Z	-,059[d]
	Asymp. Sig. (2-tailed)	,953
RightCoronarArte	Z	-1,367[b]
	Asymp. Sig. (2-tailed)	,172
RightVentricle	Z	-1,338[b]
	Asymp. Sig. (2-tailed)	,181
SuperiorVenaCava	Z	-3,180[b]
	Asymp. Sig. (2-tailed)	,001
TricuspidalValve	Z	-1,403[b]
	Asymp. Sig. (2-tailed)	,161

a. Wilcoxon Signed Ranks Test

b. Based on positive ranks.

c. The sum of negative ranks equals the sum of positive ranks.

d. Based on negative ranks.

C.6 Wilcoxon Signed Rank Test, Proton-Photon: Dmean, D45, V15, V30

Test Statistics[a]

Structure		D45FB_proton - D45FB_photon	V15GyFB_proton - V15GyFB_photon	V30GyFB_proton - V30GyFB_photon
Aorta	Z	-3,408[b]	-3,351[b]	-3,408[b]
	Asymp. Sig. (2-tailed)	<,001	<,001	<,001
AorticValve	Z	-3,408[b]	-2,366[b]	-1,000[b]
	Asymp. Sig. (2-tailed)	<,001	,018	,317
Heart	Z	-3,408[b]	-3,294[b]	-3,296[b]
	Asymp. Sig. (2-tailed)	<,001	<,001	<,001
InferiorVenaCava	Z	-3,408[b]	-1,342[b]	-1,000[b]
	Asymp. Sig. (2-tailed)	<,001	,180	,317
LeftAntDescArter	Z	-3,408[b]	-2,803[b]	-1,826[b]
	Asymp. Sig. (2-tailed)	<,001	,005	,068
LeftAtrium	Z	-3,408[b]	-3,045[b]	-2,354[b]
	Asymp. Sig. (2-tailed)	<,001	,002	,019
LeftCircumflex	Z	-3,351[b]	-2,240[b]	-1,782[b]
	Asymp. Sig. (2-tailed)	<,001	,025	,075
LeftMainCoArtery	Z	-3,294[b]	-2,533[b]	-1,483[b]
	Asymp. Sig. (2-tailed)	<,001	,011	,138
LeftVentricle	Z	-3,408[b]	-2,201[b]	-2,023[b]
	Asymp. Sig. (2-tailed)	<,001	,028	,043
MitralValve	Z	-3,408[b]	-2,201[b]	-1,826[b]
	Asymp. Sig. (2-tailed)	<,001	,028	,068
NodeAV	Z	-3,408[b]	-1,000[b]	,000[c]
	Asymp. Sig. (2-tailed)	<,001	,317	1,000
NodeSinus	Z	-3,010[b]	-1,836[b]	-2,023[b]
	Asymp. Sig. (2-tailed)	,003	,066	,043
Pericard	Z	-3,408[b]	-3,294[b]	-3,296[b]
	Asymp. Sig. (2-tailed)	<,001	<,001	<,001
PulmonaryArtery	Z	-3,351[b]	-3,408[b]	-3,067[b]
	Asymp. Sig. (2-tailed)	<,001	<,001	,002
PulmonicValve	Z	-3,408[b]	-3,059[b]	-2,023[b]
	Asymp. Sig. (2-tailed)	<,001	,002	,043
RightAtrium	Z	-3,408[b]	-2,293[b]	-1,992[b]
	Asymp. Sig. (2-tailed)	<,001	,022	,046
RightCoronarArte	Z	-3,296[b]	-1,604[b]	-1,000[b]
	Asymp. Sig. (2-tailed)	<,001	,109	,317
RightVentricle	Z	-3,296[b]	-2,201[b]	-1,000[b]
	Asymp. Sig. (2-tailed)	<,001	,028	,317
SuperiorVenaCava	Z	-2,442[b]	-2,824[b]	-2,275[b]
	Asymp. Sig. (2-tailed)	,015	,005	,023

Test Statistics[a]

Structure		D45FB_proton - D45FB_photon	V15GyFB_proton - V15GyFB_photon	V30GyFB_proton - V30GyFB_photon
TricuspidalValve	Z	-3,408[b]	-1,000[b]	,000[c]
	Asymp. Sig. (2-tailed)	<,001	,317	1,000

a. Wilcoxon Signed Ranks Test

b. Based on positive ranks.

c. The sum of negative ranks equals the sum of positive ranks.

Test Statistics[a]

Structure		ECLIPSEMeanDoseGyFB - AplanDmean
Aorta	Z	-3,296[b]
	Asymp. Sig. (2-tailed)	<,001
AorticValve	Z	-3,296[b]
	Asymp. Sig. (2-tailed)	<,001
Heart	Z	-3,296[b]
	Asymp. Sig. (2-tailed)	<,001
InferiorVenaCava	Z	-3,297[b]
	Asymp. Sig. (2-tailed)	<,001
LeftAntDescArter	Z	-3,296[b]
	Asymp. Sig. (2-tailed)	<,001
LeftAtrium	Z	-3,296[b]
	Asymp. Sig. (2-tailed)	<,001
LeftCircumflex	Z	-3,296[b]
	Asymp. Sig. (2-tailed)	<,001
LeftMainCoArtery	Z	-3,296[b]
	Asymp. Sig. (2-tailed)	<,001
LeftVentricle	Z	-3,296[b]
	Asymp. Sig. (2-tailed)	<,001
MitralValve	Z	-3,296[b]
	Asymp. Sig. (2-tailed)	<,001
NodeAV	Z	-3,296[b]
	Asymp. Sig. (2-tailed)	<,001
NodeSinus	Z	-3,296[b]
	Asymp. Sig. (2-tailed)	<,001
Pericard	Z	-3,296[b]
	Asymp. Sig. (2-tailed)	<,001
PulmonaryArtery	Z	-3,296[b]
	Asymp. Sig. (2-tailed)	<,001

Test Statistics[a]

Structure		ECLIPSEMeanDoseGyFB - AplanDmean
PulmonicValve	Z	-3,297[b]
	Asymp. Sig. (2-tailed)	<,001
RightAtrium	Z	-3,296[b]
	Asymp. Sig. (2-tailed)	<,001
RightCoronarArte	Z	-3,296[b]
	Asymp. Sig. (2-tailed)	<,001
RightVentricle	Z	-3,297[b]
	Asymp. Sig. (2-tailed)	<,001
SuperiorVenaCava	Z	-3,296[b]
	Asymp. Sig. (2-tailed)	<,001
TricuspidalValve	Z	-3,297[b]
	Asymp. Sig. (2-tailed)	<,001

a. Wilcoxon Signed Ranks Test

b. Based on negative ranks.

C.7 Descriptive Statistics, Proton-Photon: D45, V15, V30

Descriptive Statistics

Structure		N	Percentiles 25th	50th (Median)	75th
Aorta	D45FB_photon	15	15,928279660	24,681855400	38,503575000
	V15GyFB_photon	15	47,225000000	63,149909090	75,632281820
	V30GyFB_photon	15	31,085500000	38,676772730	57,944654550
	D45FB_proton	15	1,7520000000	5,9570000000	26,147000000
	V15GyFB_proton	15	24,390373630	38,640113210	54,594027400
	V30GyFB_proton	15	11,971086210	30,667102240	41,943339620
AorticValve	D45FB_photon	15	2,3990575680	5,3193671910	10,668837070
	V15GyFB_photon	15	,00000000000	,00000000000	16,449454550
	V30GyFB_photon	15	,00000000000	,00000000000	,00000000000
	D45FB_proton	15	,01300000000	,09100000000	,60700000000
	V15GyFB_proton	15	,00000000000	,00000000000	,00000000000
	V30GyFB_proton	15	,00000000000	,00000000000	,00000000000
Heart	D45FB_photon	15	1,3387576170	1,9718225390	7,8787788330
	V15GyFB_photon	15	8,8339536360	14,684500000	21,551945450
	V30GyFB_photon	15	3,3487009090	4,9472500000	9,4273700000
	D45FB_proton	15	,00850000000	,02700000000	,17700000000
	V15GyFB_proton	15	2,2343848400	3,9186530610	8,5622474920
	V30GyFB_proton	15	1,2605568510	2,0453556850	5,0491498560
InferiorVenaCava	D45FB_photon	15	,67078512300	1,1395894400	3,9866021130
	V15GyFB_photon	15	,00000000000	,00000000000	,00000000000
	V30GyFB_photon	15	,00000000000	,00000000000	,00000000000
	D45FB_proton	15	,00295652200	,03333333300	,14000000000
	V15GyFB_proton	15	,00000000000	,00000000000	,00000000000
	V30GyFB_proton	15	,00000000000	,00000000000	,00000000000
LeftAntDescArter	D45FB_photon	15	1,6606620480	2,8188635550	9,4520217390
	V15GyFB_photon	15	,00000000000	4,7424345450	34,636272730
	V30GyFB_photon	15	,00000000000	,00000000000	5,4046445450
	D45FB_proton	15	,00000000000	,06700000000	,15695950600
	V15GyFB_proton	15	,00000000000	,00000000000	,02700000000
	V30GyFB_proton	15	,00000000000	,00000000000	,00000000000
LeftAtrium	D45FB_photon	15	2,9766850740	11,792082570	17,416512100
	V15GyFB_photon	15	20,503245450	32,737600000	48,642300000
	V30GyFB_photon	15	7,4344790910	13,329409090	31,535500000
	D45FB_proton	15	,32300000000	1,0670000000	3,5930000000
	V15GyFB_proton	15	8,8524305560	13,516368080	29,481103900
	V30GyFB_proton	15	4,3462291670	8,0495818710	20,457047620
LeftCircumflex	D45FB_photon	15	2,1471163200	3,0615850590	8,3484406780
	V15GyFB_photon	15	,00000000000	6,5919354550	21,321827270
	V30GyFB_photon	15	,00000000000	,00000000000	13,210172730
	D45FB_proton	15	,05000892000	,19900000000	,76337655900
	V15GyFB_proton	15	,00000000000	,00000000000	6,8720000000
	V30GyFB_proton	15	,00000000000	,00000000000	,25200000000

Descriptive Statistics

Structure		N	Percentiles 25th	50th (Median)	75th
LeftMainCoArtery	D45FB_photon	15	8,1691740390	12,822619750	25,432895760
	V15GyFB_photon	15	,00000000000	22,650081820	100,00000000
	V30GyFB_photon	15	,00000000000	,00000000000	12,278818180
	D45FB_proton	15	,13872358900	1,0773774830	2,0995349540
	V15GyFB_proton	15	,00000000000	,00000000000	,00000000000
	V30GyFB_proton	15	,00000000000	,00000000000	,00000000000
LeftVentricle	D45FB_photon	15	,86911745200	1,1930642540	4,9878120810
	V15GyFB_photon	15	,00000000000	,00000000000	2,8234218180
	V30GyFB_photon	15	,00000000000	,00000000000	,31507536400
	D45FB_proton	15	,00350000000	,01854379600	,08600000000
	V15GyFB_proton	15	,00000000000	,00000000000	,00000000000
	V30GyFB_proton	15	,00000000000	,00000000000	,00000000000
MitralValve	D45FB_photon	15	1,7269132450	2,7351717010	11,081554170
	V15GyFB_photon	15	,00000000000	,00000000000	22,273918180
	V30GyFB_photon	15	,00000000000	,00000000000	,40161181800
	D45FB_proton	15	,02720000000	,12000000000	,39500000000
	V15GyFB_proton	15	,00000000000	,00000000000	,00000000000
	V30GyFB_proton	15	,00000000000	,00000000000	,00000000000
NodeAV	D45FB_photon	15	1,2151129830	2,2181208230	5,0275884280
	V15GyFB_photon	15	,00000000000	,00000000000	,00000000000
	V30GyFB_photon	15	,00000000000	,00000000000	,00000000000
	D45FB_proton	15	,00653214100	,04800000000	,18600000000
	V15GyFB_proton	15	,00000000000	,00000000000	,00000000000
	V30GyFB_proton	15	,00000000000	,00000000000	,00000000000
NodeSinus	D45FB_photon	15	2,8706859080	5,3022289510	14,520781330
	V15GyFB_photon	15	,00000000000	2,5084645450	43,560200000
	V30GyFB_photon	15	,00000000000	,00000000000	4,0780300000
	D45FB_proton	15	,01236927600	,26800000000	5,0558280250
	V15GyFB_proton	15	,00000000000	,00000000000	10,359125000
	V30GyFB_proton	15	,00000000000	,00000000000	,00000000000
Pericard	D45FB_photon	15	1,2756871430	2,0060800450	6,6493202660
	V15GyFB_photon	15	13,570472730	19,692927270	25,390636360
	V30GyFB_photon	15	6,5289918180	10,860527270	14,199836360
	D45FB_proton	15	,01400000000	,03000000000	,16100000000
	V15GyFB_proton	15	5,1107613290	8,7262426040	14,588301590
	V30GyFB_proton	15	3,1935407850	5,4561656800	9,8728645530
PulmonaryArtery	D45FB_photon	15	22,137774030	42,731617310	52,352308800
	V15GyFB_photon	15	72,081372730	93,119018180	99,757818180
	V30GyFB_photon	15	31,625200000	64,064500000	83,285900000
	D45FB_proton	15	3,7250000000	22,491000000	40,025000000
	V15GyFB_proton	15	28,515944440	49,935721740	66,878793970
	V30GyFB_proton	15	18,201000000	36,981216330	52,292669120

Descriptive Statistics

Structure		N	Percentiles 25th	50th (Median)	75th
PulmonicValve	D45FB_photon	15	9,2034860600	11,670923530	21,988942920
	V15GyFB_photon	15	,10129971800	17,804600000	75,360281820
	V30GyFB_photon	15	,00000000000	,00000000000	10,183100000
	D45FB_proton	15	,00569078500	,19200000000	,56900000000
	V15GyFB_proton	15	,00000000000	,00000000000	,00000000000
	V30GyFB_proton	15	,00000000000	,00000000000	,00000000000
RightAtrium	D45FB_photon	15	1,1838328790	1,8719069180	4,5105579910
	V15GyFB_photon	15	,00000000000	,77810354500	12,504500000
	V30GyFB_photon	15	,00000000000	,00000000000	1,1010809090
	D45FB_proton	15	,00614277600	,07331412900	,27600000000
	V15GyFB_proton	15	,00000000000	,00000000000	,86968382400
	V30GyFB_proton	15	,00000000000	,00000000000	,00000000000
RightCoronarArte	D45FB_photon	15	1,0934635370	1,5630977010	3,9934044000
	V15GyFB_photon	15	,00000000000	,00000000000	,00000000000
	V30GyFB_photon	15	,00000000000	,00000000000	,00000000000
	D45FB_proton	14	,00000000000	,02188092100	,12609985575
	V15GyFB_proton	14	,00000000000	,00000000000	,00000000000
	V30GyFB_proton	14	,00000000000	,00000000000	,00000000000
RightVentricle	D45FB_photon	15	,88598837100	1,1595496220	3,8115769550
	V15GyFB_photon	15	,00000000000	,00000000000	6,5171418180
	V30GyFB_photon	15	,00000000000	,00000000000	,00000000000
	D45FB_proton	14	,00000000000	,00640000000	,05800000000
	V15GyFB_proton	14	,00000000000	,00000000000	,00000000000
	V30GyFB_proton	14	,00000000000	,00000000000	,00000000000
SuperiorVenaCava	D45FB_photon	15	15,490325000	52,636651910	54,430008140
	V15GyFB_photon	15	48,915609090	99,057618180	100,00000000
	V30GyFB_photon	15	,00000000000	60,592100000	98,105572730
	D45FB_proton	15	,36900000000	46,899000000	56,191000000
	V15GyFB_proton	15	2,8660000000	67,702158730	91,121356780
	V30GyFB_proton	15	,03800000000	56,656684710	75,740734690
TricuspidalValve	D45FB_photon	15	,95902151600	1,2859530890	4,9209377220
	V15GyFB_photon	15	,00000000000	,00000000000	,00000000000
	V30GyFB_photon	15	,00000000000	,00000000000	,00000000000
	D45FB_proton	15	,00000000000	,01401574800	,07763898900
	V15GyFB_proton	15	,00000000000	,00000000000	,00000000000
	V30GyFB_proton	15	,00000000000	,00000000000	,00000000000

C.8 Wilcoxon Signed Rank Test, Photon: Dmean Heart and Dmean substructures

Test Statistics[a]

	ECLIPSEMeanDoseGyAorta - ECLIPSEMeanDoseGyHeart	ECLIPSEMeanDoseGyAorticValve - ECLIPSEMeanDoseGyHeart	ECLIPSEMeanDoseGyInferiorVenaCava - ECLIPSEMeanDoseGyHeart	ECLIPSEMeanDoseGyLeftAntDescArter - ECLIPSEMeanDoseGyHeart
Z	-4,782[b]	-,782[c]	-3,620[c]	-,339[c]
Asymp. Sig. (2-tailed)	<,001	,434	<,001	,734

Test Statistics[a]

	ECLIPSEMeanDoseGyLeftAtrium - ECLIPSEMeanDoseGyHeart	ECLIPSEMeanDoseGyLeftCircumflex - ECLIPSEMeanDoseGyHeart	ECLIPSEMeanDoseGyLeftMainCoArtery - ECLIPSEMeanDoseGyHeart	ECLIPSEMeanDoseGyLeftVentricle - ECLIPSEMeanDoseGyHeart
Z	-4,782[b]	-,278[c]	-4,278[b]	-3,877[c]
Asymp. Sig. (2-tailed)	<,001	,781	<,001	<,001

Test Statistics[a]

	ECLIPSEMeanDoseGyMitralValve - ECLIPSEMeanDoseGyHeart	ECLIPSEMeanDoseGyNodeAV - ECLIPSEMeanDoseGyHeart	ECLIPSEMeanDoseGyNodeSinus - ECLIPSEMeanDoseGyHeart	ECLIPSEMeanDoseGyPericard - ECLIPSEMeanDoseGyHeart
Z	-2,000[c]	-4,703[c]	-1,059[b]	-4,588[b]
Asymp. Sig. (2-tailed)	,045	<,001	,289	<,001

Test Statistics[a]

	ECLIPSEMeanDoseGyPulmonaryArtery - ECLIPSEMeanDoseGyHeart	ECLIPSEMeanDoseGyPulmonicValve - ECLIPSEMeanDoseGyHeart	ECLIPSEMeanDoseGyRightAtrium - ECLIPSEMeanDoseGyHeart	ECLIPSEMeanDoseGyRightCoronarArte - ECLIPSEMeanDoseGyHeart
Z	-4,782[b]	-4,402[b]	-2,808[c]	-3,970[c]
Asymp. Sig. (2-tailed)	<,001	<,001	,005	<,001

Test Statistics[a]

	ECLIPSEMeanDoseGyRightVentricle - ECLIPSEMeanDoseGyHeart	ECLIPSEMeanDoseGySuperiorVenaCava - ECLIPSEMeanDoseGyHeart	ECLIPSEMeanDoseGyTricuspidalValve - ECLIPSEMeanDoseGyHeart
Z	-4,783[c]	-4,566[b]	-4,782[c]
Asymp. Sig. (2-tailed)	<,001	<,001	<,001

a. Wilcoxon Signed Ranks Test

b. Based on negative ranks.

c. Based on positive ranks.

C.9 Wilcoxon Signed Rank Test, Proton: Dmean Heart and Dmean substructures

Test Statistics[a]

	Aorta - Heart	AorticValve - Heart	InferiorVenaCava - Heart	LeftAntDescArter - Heart	LeftAtrium - Heart
Z	-3,296[b]	-3,296[c]	-3,296[c]	-2,417[c]	-3,233[b]
Asymp. Sig. (2-tailed)	<,001	<,001	<,001	,016	,001

Test Statistics[a]

	LeftCircumflex - Heart	LeftMainCoArtery - Heart	LeftVentricle - Heart	MitralValve - Heart
Z	-,282[c]	-,910[c]	-3,296[c]	-1,789[c]
Asymp. Sig. (2-tailed)	,778	,363	<,001	,074

Test Statistics[a]

	NodeAV - Heart	NodeSinus - Heart	Pericard - Heart	PulmonaryArtery - Heart	PulmonicValve - Heart
Z	-3,296[c]	-,031[b]	-3,297[b]	-3,296[b]	-2,417[c]
Asymp. Sig. (2-tailed)	<,001	,975	<,001	<,001	,016

Test Statistics[a]

	RightAtrium - Heart	RightCoronarArte - Heart	RightVentricle - Heart	SuperiorVenaCava - Heart
Z	-3,296[c]	-3,296[c]	-3,296[c]	-2,668[b]
Asymp. Sig. (2-tailed)	<,001	<,001	<,001	,008

Test Statistics[a]

	TricuspidalValve - Heart
Z	-3,296[c]
Asymp. Sig. (2-tailed)	<,001

a. Wilcoxon Signed Ranks Test

b. Based on negative ranks.

c. Based on positive ranks.

Bibliography

[1] J. D. Bradley, R. Paulus, R. Komaki, G. Masters, G. Blumenschein, S. Schild, J. Bogart, C. Hu, K. Forster, A. Magliocco, V. Kavadi, Y. I. Garces, S. Narayan, P. Iyengar, C. Robinson, R. B. Wynn, C. Koprowski, J. Meng, J. Beitler, R. Gaur, W. Curran, and H. Choy, "Standard-dose versus high-dose conformal radiotherapy with concurrent and consolidation carboplatin plus paclitaxel with or without cetuximab for patients with stage iiia or iiib non-small-cell lung cancer (rtog 0617): a randomised, two-by-two factorial phase 3 study," *The Lancet Oncology*, vol. 16, pp. 187–199, 2 2015. 1.1, 2.5.6, 2.6.1, 5.2.3

[2] O. Gjyshi, T. Xu, A. Elhammali, D. Boyce-Fappiano, S. G. Chun, S. Gandhi, P. Lee, A. B. Chen, S. H. Lin, J. Y. Chang, A. Tsao, C. M. Gay, X. R. Zhu, X. Zhang, J. V. Heymach, F. V. Fossella, C. Lu, Q.-N. Nguyen, and Z. Liao, "Toxicity and survival after intensity-modulated proton therapy versus passive scattering proton therapy for nsclc," *Journal of Thoracic Oncology*, vol. 16, pp. 269–277, 2 2021. 1.1

[3] C. G. Boer, K. Fjellanger, I. M. Sandvik, M. Ugland, G. M. Engeseth, and L. B. Hysing, "Substantial sparing of organs at risk with modern proton therapy in lung cancer, but altered breathing patterns can jeopardize target coverage," *Cancers*, vol. 14, no. 6, 2022. 1.1, 1.2, 5.2.2

[4] H. Arnesen, P. Holck, and J. Hisdal. (2022, Nov.) Hjertet. (Accessed: Jan. 3. 2023). [Online]. Available: https://sml.snl.no/hjertet 2.1, 2.1, 5.2.1, 5.2.3

[5] P. Kumar and M. Xlark, *Clinical Medicine*, 5th ed. Saunders, 2004. 2.1, 2.2, 2.6.2, 2.6.2, 2.6.2

[6] D. J. Bell. (2019, Dec.) Great vessels. (Accessed: 2023-1-18). [Online]. Available: https://doi.org/10.53347/rID-73033// 2.1

[7] World Cancer Research Fund International. (2022, Mar.) Lung cancer statistics. (Accessed: Feb. 09. 2023). [Online]. Available: https://www.wcrf.org/cancer-trends/lung-cancer-statistics/ 2.2

[8] Kreftregisteret . (2022, Jun.) Kreft i norge. (Accessed: Feb. 09. 2023). [Online]. Available: https://www.kreftregisteret.no/Temasider/om-kreft/ 2.2

[9] Kreftregisteret. (2022, Nov.) Lungekreft. (Accessed: Jan. 31. 2023). [Online]. Available: https://www.kreftregisteret.no/Temasider/kreftformer/Lungekreft/ 2.2

[10] Kreftforeningen. (2023, Feb.) Lungekreft. (Accessed: Feb. 09. 2023). [Online]. Available: https://kreftforeningen.no/om-kreft/kreftformer/lungekreft/ 2.2, 2.5.1

[11] Helsedirektoratet, "Nasjonalt handlingsprogram med retningslinjer for diagnostikk, behandling og oppfølging av lungekreft, mesoteliom og thymom," Oslo, Jan. 2023. [Online]. Available: https://www.helsedirektoratet.no/retningslinjer/lungekreft-mesoteliom-og-thymom-handlingsprogram 2.2, 2.1, 2.2, 2.5.1, 2.5.6, 2.6, 2.6.2, A.1

[12] J. P. Gibbons, *Khans's The Physics of Radiation Therapy*, 6th ed. Wolters Kluwer Health, 2020. 2.3.1, 2.3.2, 2.3.3, 2.3.4, 2.5.3

[13] T. E. Johnson, *Health Physics*, 5th ed. McGraw-Hill Education, 2017. 2.3.2, 2.5.1

[14] K. Hoftsad. (2022, May) gray. (Accessed: Feb. 15. 2023). [Online]. Available: https://snl.no/gray 2.3.3

[15] E. J. Hall and A. J. Giaccia, *Radiobiology for the radiologist*, 8th ed. Wolters Kluwer, 2019. 2.3.3, 2.3.3, 2.3.4, 2.3.4, 2.3.4, 2.3.4, 2.3.4, 2.4.1, 2.4.1, 2.4.1, 2.4.1, 2.4.1, 2.4.1

[16] A. T. Berman, S. S. James, and R. Rengan, "Proton beam therapy for non-small cell lung cancer: Current clinical evidence and future directions," *Cancers*, vol. 7, no. 3, pp. 1178–1190, 2015. 5

[17] D. S. Chang, F. D. Lasley, I. J. Das, M. S. Mendonca, and J. R. Dynlacht, *Basic Radiotherapy Physics and Biology*, 2nd ed. Springer, 2021. 2.4.1, 2.4.2, 2.5.2

[18] G. G. Steel, T. McMillan, and J. Peacock, "The 5rs of radiobiology," *International Journal of Radiation Biology*, vol. 56, no. 6, pp. 1045–1048, 1989, pMID: 2574214. 2.4.1

[19] M. Reda, A. F. Bagley, H. Y. Zaidan, and W. Yantasee, "Augmenting the therapeutic window of radiotherapy: A perspective on molecularly targeted therapies and nanomaterials," *Radiotherapy and Oncology*, vol. 150, pp. 225–235, 2020. 7

[20] W. A. Kalender, *Computed Tomography*, 2nd ed. Erlangen: Publicis Corporate Publishing, 2005. 2.5.1

[21] D. Bell, J. Jones, and A. Murphy. (2019, Jun.) Ct intravenous contrast media. (Accessed: Feb. 23. 2023). [Online]. Available: https://doi.org/10.53347/rID-47275 2.5.1

[22] D. L. Bailey, D. W. Townsenda, P. E. Valk, and M. N. Maisey, *Positron Emission Tomography : Basic Sciences*, 3rd ed. Springer, 2003. 2.5.1

[23] F. Sciacca. (2020, Aug.) Organs at risk. Accessed: Jan. 3. 2023. [Online]. Available: https://radiopaedia.org/articles/organs-at-risk 2.5.2

[24] E. J. Hall and A. J. Giaccia, *Radiobiology for the radiologist*, 8th ed. Philadelphia, PA, USA: Wolters Kluwer, 2019. 2.5.5

[25] Norsk Lunge Cancer Gruppe, KVIST group, "Professional guidelines for curative radiotherapy of non-small cell lung cancer. revised version 2016." Norwegian Radiation Protection Authority, Tech. Rep., 2017. [Online]. Available: https://dsa.no/sok?searchquery=Faglige+anbefalinger+for+strålebehandling+ved+ikke-småcellet+lungekreft 2.5.6

[26] C. A. Perez, K. Stanley, P. Rubin, S. Kramer, L. Brady, R. PerezTamayo, G. S. Brown, J. Concannon, M. Rotman, and H. G. Seydel, "A prospective randomized study of various irradiation doses and fractionation schedules in the treatment of inoperable nonoatcell carcinoma of the lung. preliminary report by the radiation therapy oncology group," *Cancer*, vol. 45, pp. 2744–2753, 1980. 2.5.6

[27] A. McWilliam, A. Abravan, K. Banfill, C. Faivre-Finn, and M. van Herk, "Demystifying the results of rtog 0617: Identification of dose sensitive cardiac subregions associated with overall survival," *Journal of Thoracic Oncology*, vol. 18, no. 5, pp. 599–607, 2023. 2.5.6, 4.1, 5.2.3

[28] R. O. Dillman, S. L. Seagren, K. J. Propert, J. Guerra, W. L. Eaton, M. C. Perry, R. W. Carey, E. F. Frei, and M. R. Green, "A randomized trial of induction chemotherapy plus high-dose radiation versus radiation alone in stage iii non-small-cell lung cancer," *New England Journal of Medicine*, vol. 323, no. 14, pp. 940–945, 1990, pMID: 2169587. 2.5.6

[29] W. J. Curran, R. Paulus, C. J. Langer, R. Komaki, J. S. Lee, S. Hauser, B. Movsas, T. Wasserman, S. A. Rosenthal, E. Gore, M. MacHtay, W. Sause, and J. D. Cox, "Sequential vs concurrent chemoradiation for stage iii non-small cell lung cancer:

Randomized phase iii trial rtog 9410," *Journal of the National Cancer Institute*, vol. 103, pp. 1452–1460, 10 2011. 2.5.6

[30] A. Elhammali, P. Blanchard, A. Yoder, Z. Liao, X. Zhang, X. Ronald Zhu, P. K. Allen, M. Jeter, J. Welsh, and Q.-N. Nguyen, "Clinical outcomes after intensity-modulated proton therapy with concurrent chemotherapy for inoperable non-small cell lung cancer," *Radiotherapy and Oncology*, vol. 136, pp. 136–142, 2019. 2.5.6

[31] X. Zhang, Y. Li, X. Pan, L. Xiaoqiang, R. Mohan, R. Komaki, J. D. Cox, and J. Y. Chang, "Intensity-modulated proton therapy reduces the dose to normal tissue compared with intensity-modulated radiation therapy or passive scattering proton therapy and enables individualized radical radiotherapy for extensive stage iiib non-small-cell lung cancer: A virtual clinical study," *International Journal of Radiation Oncology, Biology, Physics*, vol. 77, no. 2, pp. 357–366, 2010. 2.5.6

[32] M. Thor, J. O. Deasy, C. Hu, E. Gore, V. Bar-Ad, C. Robinson, M. Wheatley, J. H. Oh, J. Bogart, Y. I. Garces, V. S. Kavadi, S. Narayan, P. Iyengar, J. S. Witt, J. W. Welsh, C. D. Koprowski, J. M. Larner, Y. Xiao, and J. Bradley, "Modeling the impact of cardiopulmonary irradiation on overall survival in nrg oncology trial rtog 0617," *Clinical Cancer Research*, vol. 26, pp. 4643–4650, 9 2020. 2.6.1, 4.1, 4.5, 5.2.3

[33] S. Vivekanandan, D. B. Landau, N. Counsell, D. R. Warren, A. Khwanda, S. D. Rosen, E. Parsons, Y. Ngai, L. Farrelly, L. Hughes, M. A. Hawkins, and J. D. Fenwick, "The impact of cardiac radiation dosimetry on survival after radiation therapy for non-small cell lung cancer," *International Journal of Radiation Oncology, Biology, Physics*, vol. 99, pp. 51–60, 9 2017. 2.6.1, 2.6.2, 4.1

[34] US Department of Health and Human Services. (2017, Nov.) Common terminology criteria for adverse events. (Accessed: Feb. 15. 2023). [Online]. Available: https://ctep.cancer.gov/protocoldevelopment/electronic_applications/docs/ctcae_v5_quick_reference_5x7.pdf 2.6.1

[35] J. S. Niedzielski, X. Wei, T. Xu, D. R. Gomez, Z. Liao, J. A. Bankson, S. Y. Lai, L. E. Court, and J. Yang, "Development and application of an elastic net logistic regression model to investigate the impact of cardiac substructure dose on radiation-induced pericardial effusion in patients with nsclc," *Acta Oncologica*, vol. 59, no. 10, pp. 1193–1200, 2020, pMID: 32678696. 2.6.1, 2.6.2, 4.1, 4.5, 5.2.2, 5.2.3

[36] F. A. van Nimwegen, G. Ntentas, S. C. Darby, M. Schaapveld, M. Hauptmann, P. J. Lugtenburg, C. P. M. Janus, L. Daniels, F. E. van Leeuwen, D. J. Cutter, and B. M. P. Aleman, "Risk of heart failure in survivors of hodgkin lymphoma: effects of cardiac exposure to radiation and anthracyclines," *Blood*, vol. 129, pp. 2257–2265, 4 2017. 2.6.1, 2.6.2, 4.1

[37] D. J. Cutter, M. Schaapveld, S. C. Darby, M. Hauptmann, F. A. V. Nimwegen, A. D. Krol, C. P. Janus, F. E. V. Leeuwen, and B. M. Aleman, "Risk for valvular heart disease after treatment for hodgkin lymphoma," *Journal of the National Cancer Institute*, vol. 107, 4 2015. 2.6.1, 2.6.2

[38] M. C. Tjong, D. S. Bitterman, K. Brantley, A. Nohria, U. Hoffmann, K. M. Atkins, and R. H. Mak, "Major adverse cardiac event risk prediction model incorporating baseline cardiac disease, hypertension, and logarithmic left anterior descending coronary artery radiation dose in lung cancer (chyll)," *Radiotherapy and Oncology*, vol. 169, pp. 105–113, 2022. 2.6.1, 2.6.2, 4.1, 4.5, 4

[39] X. Wang, N. L. Palaskas, B. P. Hobbs, J. I. Abe, K. T. Nead, S. W. Yusuf, J. Hermann, A. Deswal, and S. H. Lin, "The impact of radiation dose to heart substructures on major coronary events and patient survival after chemoradiation therapy for esophageal cancer," *Cancers*, vol. 14, 3 2022. 2.6.1, 2.6.2, 2.6.2, 4.5, 5, 5.2.2

[40] P. Lancellotti, V. T. Nkomo, L. P. Badano, J. Bergler-Klein, J. Bogaert, L. Davin, B. Cosyns, P. Coucke, R. Dulgheru, T. Edvardsen, O. Gaemperli, M. Galderisi, B. Griffin, P. A. Heidenreich, K. Nieman, J. C. Plana, S. C. Port, M. Scherrer-Crosbie, R. G. Schwartz, I. A. Sebag, J.-U. Voigt, S. Wann, and P. C. Yang, "Expert consensus for multi-modality imaging evaluation of cardiovascular complications of radiotherapy in adults: a report from the European Association of Cardiovascular Imaging and the American Society of Echocardiography," *European Heart Journal - Cardiovascular Imaging*, vol. 14, no. 8, pp. 721–740, 08 2013. 2.6.2

[41] L. Pan, D. Lei, W. Wang, Y. Luo, and D. Wang, "Heart dose linked with cardiac events and overall survival in lung cancer radiotherapy: A meta-analysis," *Medicine*, vol. 99, p. e21964, 9 2020. 2.6.2

[42] P. A. Heidenreich, S. L. Hancock, B. K. Lee, C. S. Mariscal, and I. Schnittger, "Asymptomatic cardiac disease following mediastinal irradiation," *Journal of the American College of Cardiology*, vol. 42, no. 4, pp. 743–749, 2003. 2.6.2

[43] X. Wei, H. H. Liu, S. L. Tucker, S. Wang, R. Mohan, J. D. Cox, R. Komaki, and Z. Liao, "Risk factors for pericardial effusion in inoperable esophageal cancer patients treated with definitive chemoradiation therapy," *International Journal of Radiation Oncology, Biology, Physics*, vol. 70, no. 3, pp. 707–714, 2008. 2.6.2, 4.5

[44] D. M. Gujral, G. Lloyd, and S. Bhattacharyya, "Radiation-induced valvular heart disease," *Heart*, vol. 102, no. 4, pp. 269–276, 2016. 2.6.2

[45] P. McGale, S. C. Darby, P. Hall, J. Adolfsson, N.-O. Bengtsson, A. M. Bennet, T. Fornander, B. Gigante, M.-B. Jensen, R. Peto, K. Rahimi, C. W. Taylor, and M. Ewertz, "Incidence of heart disease in 35,000 women treated with radiotherapy for breast cancer in denmark and sweden," *Radiotherapy and Oncology*, vol. 100, no. 2, pp. 167–175, 2011. 2.6.2

[46] L. Cella, R. Liuzzi, M. Conson, G. Torre, M. Caterino, N. De Rosa, M. Picardi, L. Camera, R. Solla, A. Farella, M. Salvatore, and R. Pacelli, "Dosimetric predictors of asymptomatic heart valvular dysfunction following mediastinal irradiation for hodgkins lymphoma," *Radiotherapy and Oncology*, vol. 101, no. 2, pp. 316–321, 2011. 2.6.2, 4.1

[47] H.-M. Chang, T. M. Okwuosa, T. Scarabelli, R. Moudgil, and E. T. Yeh, "Cardiovascular complications of cancer therapy: Best practices in diagnosis, prevention, and management: Part 2," *Journal of the American College of Cardiology*, vol. 70, no. 20, pp. 2552–2565, 2017. 2.2, 2.6.2, 2.6.2

[48] R. L. Larsen, R. I. Jakacki, V. L. Vetter, A. T. Meadows, J. H. Silber, and G. Barber, "Electrocardiographic changes and arrhythmias after cancer therapy in children and young adults," *The American Journal of Cardiology*, vol. 70, no. 1, pp. 73–77, 1992. 2.6.2

[49] M. J. Adams, S. R. Lipsitz, S. D. Colan, N. J. Tarbell, S. T. Treves, L. Diller, N. Greenbaum, P. Mauch, and S. E. Lipshultz, "Cardiovascular status in long-term survivors of hodgkin's disease treated with chest radiotherapy," *Journal of Clinical Oncology*, vol. 22, no. 15, pp. 3139–3148, 2004, pMID: 15284266. 2.6.2

[50] Y. Qian, H. Zhu, E. L. Pollom, B. Y. Durkee, A. A. Chaudhuri, M. F. Gensheimer, M. Diehn, D. B. Shultz, and B. W. Loo Jr, "Sinoatrial node toxicity after stereotactic ablative radiation therapy to lung tumors," *Practical Radiation Oncology*, vol. 7, no. 6, pp. e525–e529, 2017. 2.6.2, 4.1

[51] K. M. Nielsen, B. V. Offersen, H. M. Nielsen, M. Vaage-Nilsen, and S. W. Yusuf, "Short and long term radiation induced cardiovascular disease in patients with cancer," *Clinical Cardiology*, vol. 40, no. 4, pp. 255–261, 2017. 2.6.2

[52] S. C. Darby, M. Ewertz, P. McGale, A. M. Bennet, U. Blom-Goldman, D. Brønnum, C. Correa, D. Cutter, G. Gagliardi, B. Gigante, M.-B. Jensen, A. Nisbet, R. Peto, K. Rahimi, C. Taylor, and P. Hall, "Risk of ischemic heart disease in women after radiotherapy for breast cancer," *New England Journal of Medicine*, vol. 368, no. 11, pp. 987–998, 2013, pMID: 23484825. 2.6.2

[53] T. Tagami, M. F. Almahariq, D. V. Balanescu, T. J. Quinn, J. T. Dilworth, B. A. Franklin, and A. Bilolikar, "Usefulness of coronary computed tomographic angiography to evaluate coronary artery disease in radiotherapy-treated breast cancer survivors," *The American Journal of Cardiology*, vol. 143, pp. 14–20, 2021. 2.6.2

[54] F. K. Duane, N. B. Boekel, J. N. Jacobse, Z. Wang, B. M. Aleman, S. C. Darby, M. Schaapveld, F. E. van Leeuwen, M. H. Baaijens, S. Warren, and C. W. Taylor, "Exposure of the heart and cardiac valves in women irradiated for breast cancer 19702009," *Clinical and Translational Radiation Oncology*, vol. 36, pp. 132–139, 2022. 2.6.2, 4.1

[55] M. Martinou and A. Gaya, "Cardiac complications after radical radiotherapy," *Seminars in Oncology*, vol. 40, no. 2, pp. 178–185, 2013, cardio-oncology: The Relationships Between the Heart and Cancer. 2.6.2

[56] M. Adams, P. H. Hardenbergh, L. S. Constine, and S. E. Lipshultz, "Radiation-associated cardiovascular disease," *Critical Reviews in Oncology/Hematology*, vol. 45, no. 1, pp. 55–75, 2003. 2.6.2

[57] G. Gagliardi, L. S. Constine, V. Moiseenko, C. Correa, L. J. Pierce, A. M. Allen, and L. B. Marks, "Radiation dose-volume effects in the heart," *International Journal of Radiation Oncology, Biology, Physics*, vol. 76, 3 2010. 2.6.2

[58] K. Fjellanger, L. Rossi, B. J. Heijmen, H. E. S. Pettersen, I. M. Sandvik, S. Breedveld, T. H. Sulen, and L. B. Hysing, "Patient selection, inter-fraction plan robustness and reduction of toxicity risk with deep inspiration breath hold in intensity-modulated radiotherapy of locally advanced non-small cell lung cancer," *Frontiers in Oncology*, vol. 12, 8 2022. 3.2

[59] F. Duane, M. C. Aznar, F. Bartlett, D. J. Cutter, S. C. Darby, R. Jagsi, E. L. Lorenzen, O. McArdle, P. McGale, S. Myerson, K. Rahimi, S. Vivekanandan, S. Warren, and C. W. Taylor, "A cardiac contouring atlas for radiotherapy," *Radiotherapy and Oncology*, vol. 122, pp. 416–422, 3 2017. 3.3.2, 3.3.3, 1, 3.3.4, 5.1, 5.3

[60] J. Socha, A. Rygielska, B. Uzibo-yczkowska, J. Chaubiska-Fendler, A. Jurek, M. Maciorowska, M. Mielniczuk, P. Pawowski, D. Tyc-Szczepaniak, P. Krzesiski, and L. Kepka, "Contouring cardiac substructures on average intensity projection 4d-ct for lung cancer radiotherapy: A proposal of a heart valve contouring atlas," *Radiotherapy and Oncology*, vol. 167, pp. 261–268, 2022. 3.3.2, 3.3.4, 5.1, 5.1

[61] P. Loap, V. Servois, G. Dhonneur, K. Kirov, A. Fourquet, and Y. Kirova, "A radiation therapy contouring atlas for cardiac conduction node delineation," *Practical Radiation Oncology*, vol. 11, no. 4, pp. e434–e437, 2021. 3.3.2, 3.3.4

[62] J. P. Delille, A. Hernigou, V. Sene, G. Chatellier, J. C. Boudeville, P. Challande, and M. C. Plainfosse, "Maximal thickness of the normal human pericardium assessed by electron-beam computed tomography," *European Radiology*, vol. 9, pp. 1183–1189, 1999. 3.3.4

[63] H. E. S. Pettersen, "Dvhtoolkit," https://github.com/BergenParticleTherapy/DVHToolkit, 2019. 3.4.1, 3.5.3

[64] Microsoft Corporation, "Microsoft excel." [Online]. Available: https://office.microsoft.com/excel 3.4.1

[65] D. J. Bell. (2021, Aug.) Dice similarity coefficient. Accessed: Jan. 24. 2023. [Online]. Available: https://doi.org/10.53347/rID-75056 3.4.1

[66] S. Jacob, J. Camilleri, S. Derreumaux, V. Walker, O. Lairez, M. Lapeyre, E. Bruguière, A. Pathak, M.-O. Bernier, D. Laurier, J. Ferrieres, O. Gallocher, I. Latorzeff, B. Pinel, D. Franck, C. Chevelle, G. Jimenez, and D. Broggio, "Is mean heart dose a relevant surrogate parameter of left ventricle and coronary arteries exposure during breast cancer radiotherapy: a dosimetric evaluation based on individually-determined radiation dose (baccarat study)," *Radiation Oncology*, vol. 14, p. 29, 2019. 4.1, 4.5

[67] S. Momin, J. Wolf, J. Roper, Y. Lei, T. Liu, J. D. Bradley, K. Higgins, X. Yang, and J. Zhang, "Enhanced cardiac substructure sparing through knowledge-based treatment planning for non-small cell lung cancer radiotherapy," *Frontiers in Oncology*, vol. 12, 2022. 4.1, 5.2.3

[68] S. Ellahham, A. Khalouf, M. Elkhazendar, N. Dababo, and Y. Manla, "An overview of radiation-induced heart disease," *Radiation Oncology Journal*, vol. 40, no. 2, pp. 89–102, 2022. 4.1

[69] A. McWilliam, J. Kennedy, C. Hodgson, E. Vasquez Osorio, C. Faivre-Finn, and M. van Herk, "Radiation dose to heart base linked with poorer survival in lung cancer patients," *European Journal of Cancer*, vol. 85, pp. 106–113, 2017. 4.1, 5.2.3

[70] K. Wang, K. A. Pearlstein, N. D. Patchett, A. M. Deal, P. Mavroidis, B. C. Jensen, M. B. Lipner, T. M. Zagar, Y. Wang, C. B. Lee, M. J. Eblan, J. G. Rosenman, M. A. Socinski, T. E. Stinchcombe, and L. B. Marks, "Heart dosimetric analysis of three types of cardiac toxicity in patients treated on dose-escalation trials for stage iii non-small-cell lung cancer," *Radiotherapy and Oncology*, vol. 125, pp. 293–300, 11 2017. 4.5, 5.2.3

[71] A. McWilliam, J. Khalifa, E. Vasquez Osorio, K. Banfill, A. Abravan, C. Faivre-Finn, and M. van Herk, "Novel methodology to investigate the effect of radiation dose to heart substructures on overall survival," *International Journal of Radiation Oncology, Biology, Physics*, vol. 108, no. 4, pp. 1073–1081, 2020. 4.5

[72] M. J. Ferris, K. S. Martin, J. M. Switchenko, O. A. Kayode, J. Wolf, Q. Dang, R. H. Press, W. J. Curran, and K. A. Higgins, "Sparing cardiac substructures with optimized volumetric modulated arc therapy and intensity modulated proton therapy in thoracic radiation for locally advanced non-small cell lung cancer," *Practical Radiation Oncology*, vol. 9, pp. e473–e481, 9 2019. 5.2.2, 5.2.3

[73] Kreftregisteret. (2022) Årsrapport 2021 med resultater og forbedringstiltak fra nasjonalt kvalitetsregister for lungekreft. Oslo, Norway. (Accessed: May. 27. 2023). [Online]. Available: https://www.kreftregisteret.no/globalassets/publikasjoner-og-rapporter/arsrapporter/publisert-2022/arsrapport-2021-nasjonalt-kvalitetsregister-for-lungekreft.pdf 5.2.3